N° d'ordre NNT: 2022LYSEC0013

THÈSE de DOCTORAT DE L'UNIVERSITÉ DE LYON
opérée au sein de l'École Centrale de Lyon

École Doctorale N° 162
Mécanique Énergétique Génie Civil Acoustique

Spécialité de doctorat : Acoustique

Soutenue publiquement le 01/04/2022, par
David Lamidel

Aerodynamic noise sources due to the tip flow in the fan stage of turbofan engines

---

Devant le jury composé de:

Carolus, Thomas	Professeur	Université de Siegen	Rapporteur
Sanjosé, Marlène	Professeure	ÉTS, Université du Québec	Rapporteure
Boudet, Jérôme	Maître de conférence	LMFA	Examinateur
Carbonneau, Xavier	Professeur	ISAE-Supaéro	Président du jury
Roger, Michel	Professeur	LMFA	Directeur de thèse
Daviller, Guillaume	Docteur	CERFACS	Encadrant de thèse
De Laborderie, Hélène	Docteur	Safran Aircraft Engines	Invitée

Remerciements

Cette thèse est le fruit d'une collaboration entre Safran Aircraft Engines, le Laboratoire de Mécanique des Fluides et d'Acoustique (LMFA) de l'École Centrale de Lyon et le CERFACS. Elle est co-financée par Safran Aircraft Engines et la DGA/DGAC dans le cadre du projet AITEC 2 et par l'ANRT via une thèse CIFRE (2018/1057). Ces travaux ont également été réalisés dans le cadre du LABEX CeLyA (ANR-10-LABX-0060) de l'Université de Lyon, dans le programme "Investissements d'Avenir" (ANR-16-IDEX-0005) opéré par l'ANR. L'ensemble des simulations numériques a été réalisé grâce aux ressources de calcul fournies par le réseau GENCI sous le numéro d'allocation A0082A06074 et le CERFACS.

En premier lieu, je remercie les membres du jury d'avoir accepté d'évaluer mes travaux de thèse. Un grand merci aux deux rapporteurs Professeure Marlène Sanjosé et Professeur Thomas Carolus pour avoir évalué mon travail en détails. Je tiens également à remercier Jérôme Boudet et Professeur Xavier Carbonneau d'avoir examiné mes travaux avec leur expertise en turbomachines.

Je souhaite remercier mes encadrants de thèse: Michel Roger, Guillaume Daviller et Hélène De Laborderie. Chacun a su apporter sa contribution aux différents sujets de recherche abordés durant la thèse. Malgré la distance, un lien a été maintenu tout au long de la thèse. Je voudrais aussi remercier Fernando Gea Aguilera qui a pris le relais d'Hélène pendant son absence.

Mes remerciements vont naturellement à toute l'équipe acoustique du LMFA notamment à Emmanuel Jondeau qui m'a fourni toutes les données expérimentales du cas profil isolé fixe. J'ai pu également faire la rencontre de nombreuses personnes autour d'un baby-foot ou sur une péniche: Pierre, Etienne, Simon, Mathieu l'admirateur de panthère, Yann l'auteur d'EPP, Helmut le cascadeur nocturne, Danny lou proufechounel des pots de thèse et Miguel le flambeur du Bec de jazz.

Après 6 mois au LMFA à Lyon, j'ai poursuivi ma thèse au CERFACS à Toulouse. J'exprime toute ma gratitude à l'équipe turbomachines qui m'a conseillé plusieurs fois sur l'aspect numérique: Florent Duchaine, Nicolas Odier, Jérôme Dombard et Laurent Gicquel. Je tiens également à remercier l'équipe CSG pour leur support indéfectible: Fred, Patrick, Gérard, Fabrice et Isa. De plus, l'équipe Admin formée notamment de Chantal, Michèle, Marie

et Jade, a su apporter une bonne humeur et un cadre de travail agréable. Je pense aussi aux moments passés avec la grande équipe de foot de l'EAC qui terrasse toute la métropole toulousaine: Val, Jarjar, Lulu, Yann, Louis, Maxou le Cap, Kam l'aficionados d'Aulas, Cazard le briseur de glaçons et concombres, Polo l'influenceur de Strava, Chrichri le plus reggaeton des gardiens havrais et Marchal le frrrr. Je tiens à remercier la team Kitesurf pour m'avoir permis d'arriver des lundis matins avec le visage rouge du coup de soleil de la veille: Bastien, Laroche, Romain la plagiste qui vend du matos, Kelu le breton volant de Colombie, Toutoul le destructeur de canapé[1], Flo le marseillais qui transpire beaucoup trop et Adelita la meilleure compagne de Chpritz. Grâce à eux, j'ai pu découvrir ce sport et faire de beaux voyages. Merci aussi à Juanito pour ses conseils à la petanque, Gauthier pour son talent de photographe et Thibault pour les moments passés autour des platines.

Je tiens à remercier ma mère qui a toujours été là pour moi y compris pour la thèse. Et j'ai une pensée pour mon père qui m'a vu commencé la thèse et qui aurait été fier de me voir l'achever.

[1] Ne pas l'inviter à sa crémaillière.

Résumé

Au regard de l'augmentation du trafic aérien soutenue par les pays émergents ainsi que des certifications acoustiques de plus en plus strictes, les motoristes portent une attention particulière à la compréhension, la prédiction et le contrôle du bruit de soufflante. L'étage de soufflante des futurs turbofans à très haut taux de dilution devrait être responsable d'une partie non-négligeable du bruit rayonné par un avion. De plus, la contribution du bruit de soufflante, aussi bien tonal que large bande, sur les architectures actuelles est importante pour des régimes d'approche et au décollage. Parmi les mécanismes physiques générant le bruit de soufflante, le bruit de jeu en tête de pale est actuellement considéré de second ordre et n'est pas pris en compte dans l'évaluation du bruit de soufflante. L'évolution vers des architectures à très haut taux de dilution peut faire évoluer l'importance du bruit de jeu du second au premier ordre. Dans ce contexte, des simulations aux grandes échelles résolvant les grandes structures tourbillonnaires et modélisant les petites, sont réalisées sur un profil isolé fixe et une soufflante à échelle réduite représentative d'un turbofan à très haut taux de dilution. Basée sur une comparaison avec des mesures, cette méthode numérique montre une capacité prédictive de l'aérodynamique instationnaire de l'écoulement de jeu. Une approche avec une loi de paroi permet la simulation d'applications turbomachines telles que la soufflante à échelle réduite. De plus, l'adaptation de maillage basée sur des quantités physiques se présente comme une méthodologie appropriée à la résolution des structures tourbillonnaires complexes tridimensionnelles des écoulements secondaires d'une turbomachine comme l'écoulement de jeu. Des fonctions d'identification sont également appliquées afin de caractériser le tourbillon de jeu en tête de pales. Afin d'augmenter la connaissance pour la définition de nouveaux modèles du bruit de jeu, une analyse des écoulements de jeu des deux configurations est réalisée. Parmi les mécanismes aérodynamiques sources du bruit de jeu, la diffraction des structures tourbillonnaires dans le jeu par les arêtes de l'extrémité de pale apparaît comme le mécanisme dominant sur les architectures à très haut taux de dilution.

Mots-clés: Écoulement de jeu, Bruit de jeu, Profil isolé, Soufflante à échelle réduite, Simulation aux grandes échelles, Adaptation de maillage, Identification de tourbillon.

Abstract

Regarding the growth of global air transport sustained by the emerging countries and the more and more stringent noise certification, engine manufacturers pay particular attention on the understanding, prediction and control of fan noise. The fan stage of future ultra-high by-pass ratio turbofans may be responsible for a significant part of the noise radiated by an aircraft. Moreover, the fan noise contribution on the current turbofans, whether tonal or broadband, is large at both approach and take-off operating points. Among several physical mechanisms generating the fan noise, the tip clearance noise at the tip of fan blades is considered as a secondary source of noise on the current turbofan architectures and is not accounted for the evaluation of fan noise. The evolution towards ultra-high by-pass ratio architectures may bring the tip clearance noise from a secondary source to a primary one. In this context, large-eddy simulations resolving the large eddies and modelling the small ones, are performed on an isolated airfoil and a rig-scaled fan representative of future ultra-high by-pass ratio turbofan engine. Based on a comparison with measurements, the numerical method shows its capacity to recover the unsteady aerodynamics of the tip flow. A wall-modelled approach allows for the computation of turbomachinery applications such as the rig-scaled fan. Moreover, mesh adaptation based on flow quantities appears to be an appropriate methodology to resolve the complex three-dimensional vortical structure of turbomachinery secondary flows such as the tip flow. Identification functions are also applied to characterise the tip leakage vortex at the tip of fan blades. To bring knowledge for the definition of new models of tip clearance noise, an analysis of tip flows on the two configurations is carried out. Among several aerodynamic source mechanisms of tip clearance noise, the scattering of vortical structures in the gap by the tip edges appears to be the dominant mechanism on ultra-high by-pass ratio turbofan engine.

Keywords: Tip leakage flow, Tip clearance noise, Isolated airfoil, Rig-scaled fan, Large-eddy simulation, Mesh adaptation, Vortex identification.

Contents

Nomenclature

Symbols

β	Angle of attack (°)
$\boldsymbol{\Omega} = (\Omega_1, \Omega_2, \Omega_3)$	Vorticity vector $\left(\mathrm{s}^{-1}\right)$
$\boldsymbol{v} = (v_1, v_2, v_3)$	Absolute instantaneous velocity vector $\left(\mathrm{m.s}^{-1}\right)$
$\boldsymbol{V} = (V_1, V_2, V_3)$	Absolute mean velocity vector $\left(\mathrm{m.s}^{-1}\right)$
$\boldsymbol{v} = (v_x, v_r, v_t)$	Velocity vector in the cylindrical system of coordinates $\left(\mathrm{m.s}^{-1}\right)$
$\boldsymbol{v} = \left(v_x, v_y, v_z\right)$	Velocity vector in the Cartesian system of coordinates $\left(\mathrm{m.s}^{-1}\right)$
$\boldsymbol{W} = (W_1, W_2, W_3)$	Relative mean velocity vector $\left(\mathrm{m.s}^{-1}\right)$
$\boldsymbol{w} = (w_1, w_2, w_3)$	Relative instantaneous velocity vector $\left(\mathrm{m.s}^{-1}\right)$
δ	Boundary layer thickness (m)
$\dot{m}$	Massflow rate $\left(\mathrm{kg.s}^{-1}\right)$
ϵ	Turbulent dissipation rate $\left(\mathrm{m}^3\mathrm{.s}^{-2}\right)$
γ	Specific heat capacity ratio (-)
κ	Wavenumber $\left(\mathrm{m}^{-1}\right)$
$\mathscr{Q}$	Heat transfer per mass unit $\left(\mathrm{m}^2\mathrm{.s}^{-2}\right)$
$\mathscr{W}$	Work transfer per mass unit $\left(\mathrm{m}^2\mathrm{.s}^{-2}\right)$

μ	Dynamic viscosity $\left(\text{kg.m}^{-1}.\text{s}^{-1}\right)$
ν	Kinematic viscosity $\left(\text{m}^2.\text{s}^{-1}\right)$
ω	Angular frequency $\left(\text{rad.s}^{-1}\right)$
Π	Total pressure ratio (-)
ρ	Density $\left(\text{kg.m}^{-3}\right)$
σ	Shear-stress tensor $\left(\text{kg.m}^{-1}.\text{s}^{-2}\right)$
τ	Time (s)
a	Sound velocity $\left(\text{m.s}^{-1}\right)$
c	Blade chord (m)
c_p	Specific heat capacity at constant pressure $\left(\text{m}^2.\text{s}^{-2}.\text{K}^{-1}\right)$
c_v	Specific heat capacity at constant volume $\left(\text{m}^2.\text{s}^{-2}.\text{K}^{-1}\right)$
c_x	Blade axial chord (m)
e	Blade thickness (m)
E_{tot}	Total energy per mass unit $\left(\text{m}^2.\text{s}^{-2}\right)$
f	Frequency $\left(\text{s}^{-1}\right)$
h	Enthalpy per mass unit $\left(\text{m}^2.\text{s}^{-2}\right)$
k	Turbulent kinetic energy $\left(\text{m}^2.\text{s}^{-2}\right)$
l	Blade span (m)
N	Rotation speed $\left(\text{tr.mn}^{-1}\right)$
P	Mean pressure $\left(\text{kg.m}^{-1}.\text{s}^{-2}\right)$
p	Instantaneous pressure $\left(\text{kg.m}^{-1}.\text{s}^{-2}\right)$
r	Specific gas constant $\left(\text{m}^2.\text{s}^{-2}.\text{K}^{-1}\right)$
s	Gap height (m)
T	Temperature (K)
t	Pitch (m)

U	Blade speed $\left(\mathrm{m.s}^{-1}\right)$

Dimensionless numbers

Ma = V/a	Mach number (-)
Re = Vc/ν	Reynolds number (-)
St = fc/V	Strouhal number (-)
C_p	Pressure coefficient (-)

Subscripts

0	Relative to the reference state
tip	Relative to the blade tip
sta	Relative to the static quantity
tot	Relative to the total quantity
LE	Relative to the blade leading edge
TE	Relative to the blade trailing edge

Superscripts

$.''$	Fluctuating quantity from Favre time average
$.'$	Fluctuating quantity from Reynolds time average
$.^{**}$	Fluctuating quantity from Favre spatial filter
$.^{*}$	Fluctuating quantity from Reynolds spatial filter
rms	root-mean-squared
sgs	subgrid-scale

Operators

$\langle\, . \,\rangle$	Reynolds time average
$\|\| \, . \, \|\|$	Vector magnitude
$\overline{.}$	Reynolds spatial filter
$\widehat{.}$	Favre time average

$\widetilde{.}$	Favre spatial filter

Acronyms

ALE	Arbitrary Lagrangian–Eulerian
BPF	Blade Passage Frequency
CFL	Courant–Friedrichs–Lewy condition
CPU	Central Processing Unit
FWH	Ffowcs-Williams and Hawkings
IATA	International Air Transport Association
ICAO	International Civil Aviation Organisation
IGV	Inlet Guide Vanes
LBM	Lattice Boltzmann Method
LDV	Laser Doppler Velocimetry
LES	Large Eddy Simulation
Nn	Nominal rotation speed
OGV	Outlet Guide Vanes
PIV	Particle Image Velocimetry
PSD	Power Spectral Density
RANS	Reynolds-Averaged Navier-Stokes
RI	Rotating Instability
TBLE	Thin Boundary Layer Equations
TCN	Tip Clearance Noise
TCS	Turbulence Control Screen
TLF	Tip Leakage Flow
TLV	Tip Leakage Vortex
TSV	Tip Separation Vortex

TTGC	Two-Step Taylor Galerkin C
UHBR	Ultra-High By-pass Ratio
URANS	Unsteady Reynolds-Averaged Navier-Stokes
WMLES	Wall-Modeled Large-Eddy Simulation
WRLES	Wall-Resolved Large-Eddy Simulation
ZLES	Zonal Large-Eddy Simulation

List of Figures

List of Tables

Introduction

Aeronautics context

In 2018, the International Air Transport Association (IATA)[2] released its air transportation forecast [40]. Figure 1 presents the global air transport passenger numbers over time under three scenarios. With a constant policies scenario in magenta, the passenger numbers could double to 7 billion in 2037. In a reverse scenario in which protectionism develops (blue), aviation would continue to grow, but at a slower pace. On the contrary, the global passenger numbers should increase faster under a liberalized environment (green).

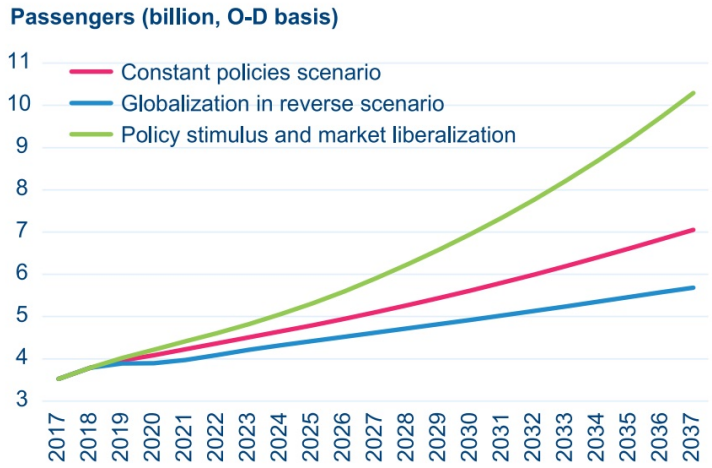

Figure 1: Global air transport passenger numbers over time from IATA [40].

The global market growth will be sustained by a strong air transportation development in emerging countries. Figure 2 shows the ten largest passenger markets over time. China will displace the United States (US) as the world's largest aviation market in 2025. Moreover, India may become the 3rd air passenger market, surpassing the United Kingdom (UK) around 2024. Finally, Indonesia will climb from the world's 10th largest aviation market in 2017 to

[2]IATA represents some 290 airlines comprising 82% of global air traffic.

the 4th largest by 2030.

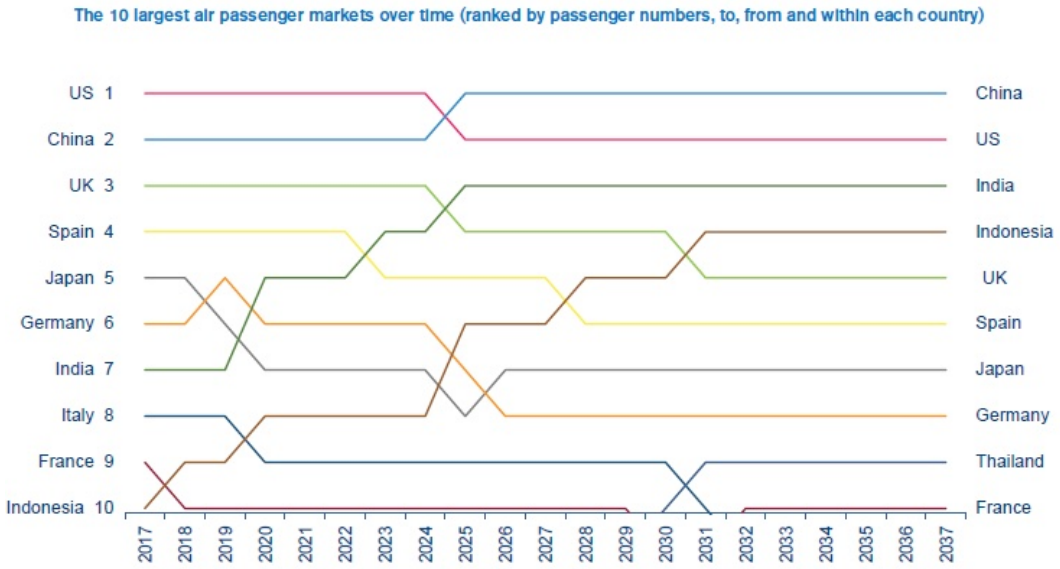

Figure 2: Ten largest passenger markets over time from IATA [40].

The global pandemic in 2020 had a profound impact on the forecast profile. The IATA revised 2020 passenger traffic forecast down for Middle East [42] and Africa [41]. In both regions, the full-year 2020 passenger numbers reached only 30% of 2019 levels. A full return to 2019 levels is not expected until late 2023 for Africa and 2024 for Middle East. Nevertheless, a strong and gradually recovery is expected in the long term.

The civil aviation stakeholders will then face both economical and environmental challenges to sustain a high global air market growth. The decrease of the averaged ticket price draws airline companies to reduce operation cost to maintain profitability. Meanwhile, aircraft and engine manufacturers must strongly reduce greenhouse gases and noise emissions. Indeed, noise emission affects people living in the vicinity of airports during take-offs and landings (community noise) and ramp agents during ground operations (ramp noise). Noise generated by civil aviation are framed by the International Civil Aviation Organisation (ICAO) at global scale and by the airport at local scale.

The ICAO defines standards on community noise through the Annex 16 to the Convention on International Civil Aviation [44]. Threshold noise level are defined on three trajectory points as shown in Figure 3a: approach, lateral/sideline, flyover/cutback. A cumulative threshold value on the three points is also defined. Figure 3b shows the progression of the ICAO noise standards defined in Effective Perceived Noise Level (EPNL). This metric takes into account the specificity of the human ear response, the annoyance perceived due to the emergence of tones in the acoustic spectrum and the time of exposure to the annoyance. Threshold noise levels depend on the weight of the aircraft expressed in Maximum Take-off

Weight (MTOW). Standards on the community noise become more and more stringent as the air traffic market expands. Aircraft must comply with the ICAO standards to get a flight authorisation. Besides, the ICAO also makes recommendations for the ramp noise.

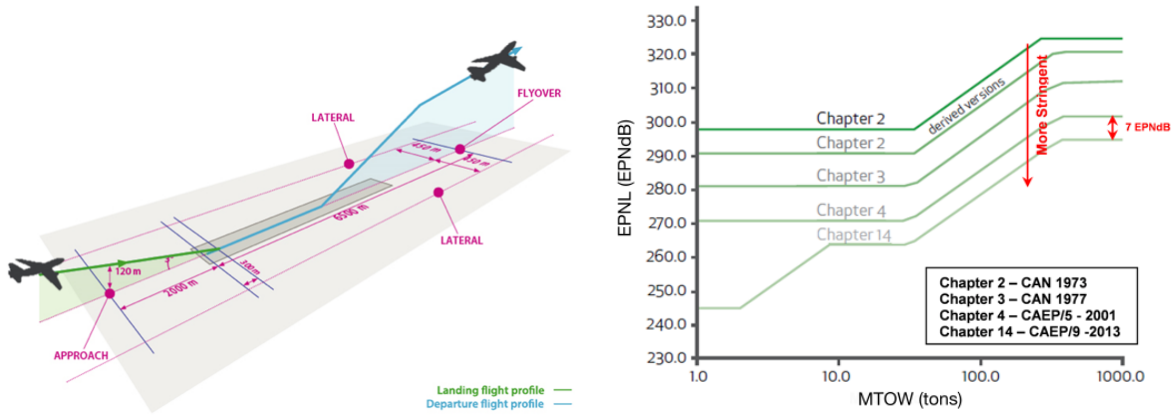

(a) (b)

Figure 3: (a) Aircraft noise certification reference measurement points. (b) Progression of the ICAO noise standards. Both extracted from course "Bruit des transports aériens et terrestres" of *École Centrale de Lyon* [99].

In addition to the international standards, local noise fees and flight restriction policies are set up by some airports because of residents' complaints. The policies have a non-negligible economic impact for airline companies. Regarding this economic stake and ICAO certification, the understanding, prediction and control of aircraft noise sources are major challenges for aircraft manufacturers.

Turbofan noise

Aircraft noise is mainly generated by the airframe (fuselage, landing gears, high lift devices) and the engines. The noise breakdown is strongly dependent on the aircraft type and engine architecture. The CFM LEAP that powers the Airbus A320neo, Boeing 737 MAX and COMAC C919 [3] is a dual spool direct drive engine architecture. The latter sketched in Figure 4 is composed of two shafts. The work produced by the high pressure turbine is directly transmitted by the high pressure shaft in orange to the high pressure compressor. Similarly, the work produced by the low pressure turbine is directly transmitted by the low pressure shaft in blue to the low pressure compressor and fan. Downstream of the fan, Outlet Guide Vanes (OGV) and Inlet Guide Vanes (IGV) are found in the by-pass and primary ducts, respectively. Combustion occurs in the combustor in red to power the turbine.

A schematic noise breakdown for dual spool direct drive engines is presented in Figure 5. The contribution of each component differs according to the ICAO certification point. Approach, sideline and cutback points are, respectively, in blue, orange and green. Airframe noise and fan noise are dominant at approach whereas it is jet noise and fan noise at take-off.

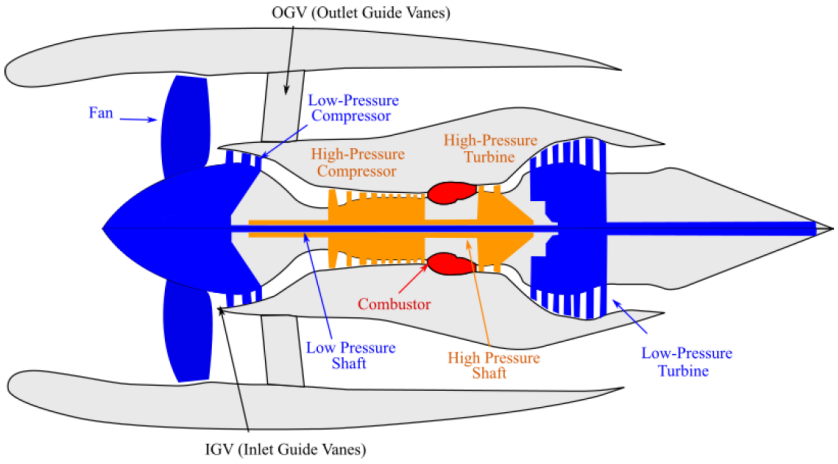

Figure 4: Dual spool direct drive engine architecture extracted from course "Bruit des transports aériens et terrestres" of *École Centrale de Lyon* [99].

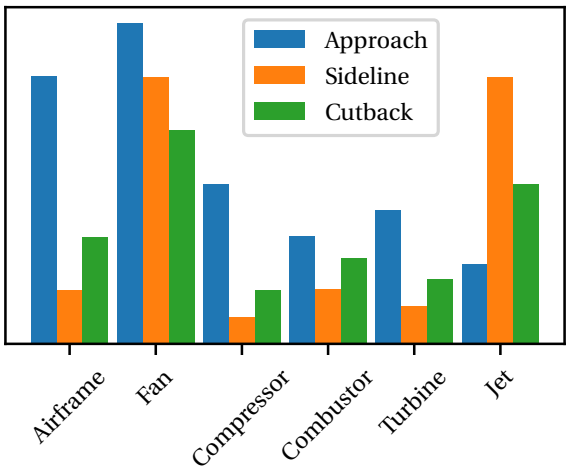

Figure 5: Schematic noise breakdown for dual spool direct drive engines adapted from course "Bruit des transports aériens et terrestres" of *École Centrale de Lyon* [99].

Several physical mechanisms generating the fan noise are sketched in Figure 6. Noise sources are divided into tonal and broadband components. Tonal noise is produced by a periodic phenomena in time and characterised by a peak at discrete frequencies in the acoustic spectrum. Broadband noise is generated by a random and non-periodic phenomena and spreads over a large range of frequencies in the acoustic spectrum. Broadband mechanisms are highlighted in blue whereas tonal mechanisms are in green. The following broadband mechanisms generating fan noise on modern fans are identified:

- The interaction between fan blade turbulent wakes and OGV/IGV leading edges (primary source).
- The fan self-noise, which is the interaction between turbulent structures in boundary layers developing on fan blades and their trailing edge (primary source).

- The interaction between the atmospheric upstream turbulence and fan blades (secondary source).
- The interaction of inlet boundary layers on casing (nacelle) and hub with fan blades and OGV, which also includes tip gap vortices contribution (secondary source).

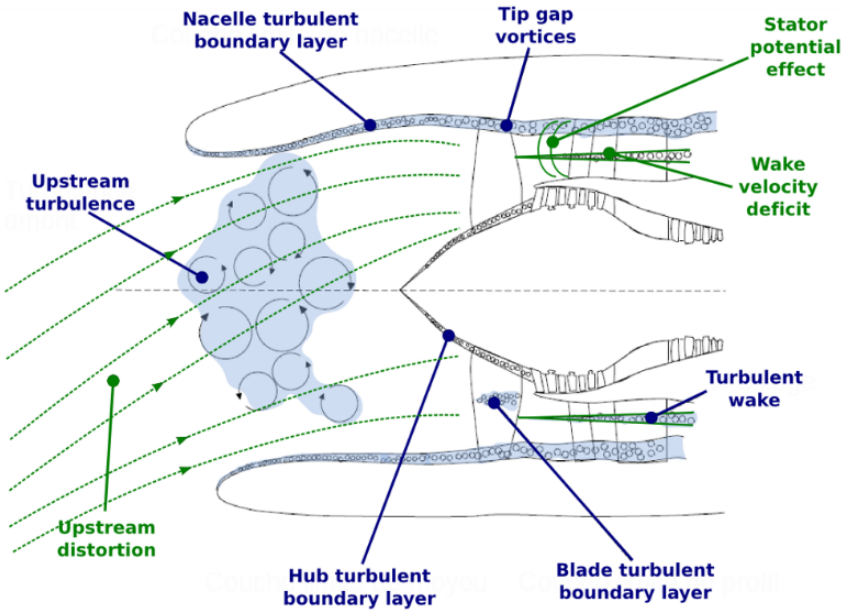

Figure 6: Sketch of the generation mechanismns of fan noise on turbofan engine from Moreau [63].

Together with broadband mechanisms, the following tonal mechanisms are also found:

- The interaction of wake velocity deficits of fan blades with OGV/IGV leading edges (primary source).
- The fan self-noise which is due to fan rotation and decomposed into loading noise and thickness noise (primary source for transonic/supersonic ratings).
- The interaction between upstream distortion and fan blades (primary source),
- The interaction between downstream distortion that can be generated by the presence of OGV heterogeneities, and fan blades (primary source).
- The interaction of inlet boundary layers on casing (nacelle) and hub with fan blades and OGV, which also includes tip gap vortices contribution (secondary source).

The relative importance of broadband and tonal mechanisms generating fan noise depends on the fan geometry. Therefore, engine manufacturers have to account for the evolution of turbofan engine architectures to evaluate turbofan noise. One candidate of near-term architectures is the Ultra-High By-pass-Ratio (UHBR) turbofan engine.

Ultra-High By-pass-Ratio turbofan architecture

Driven by the reduction of fuel consumption, the By-Pass Ratio[3] (BPR) of turbofan engine has continuously increased through decades. Figure 7 presents three generations of turbofan engines. In 1990's, turbofan engines having BPR from 5 to 7 were used such as CFM56 [1] with a BPR of 6 (Figure 7a). Then, in 2010's, a new generation with higher BPR around 10 emerged such as CFM LEAP [3] with a BPR of 11 (Figure 7b). For the next generation of turbofan engines, BPR more than 15 are considered. This next generation of propulsion systems called UHBR turbofan was studied in the EU project ENOVAL [2] (Figure 7c).

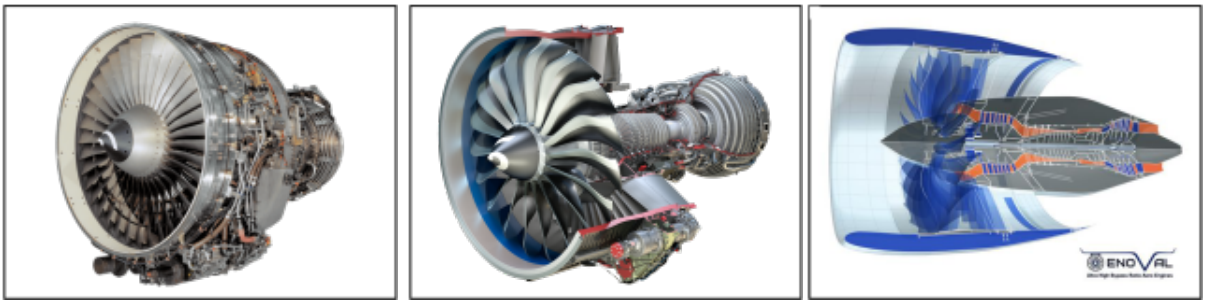

(a) CFM56 [1]. (b) CFM LEAP [3]. (c) ENOVAL [2].

Figure 7: Three generations of turbofan engines.

For UHBR turbofan architectures, the fan diameter is further increased at the price of a relatively shorter nacelle to reduce both weight and drag. Consequently, the balance of noise sources is modified. Figure 8 presents a typical turbofan engine spectrum and future trends for UHBR architectures from Moreau [63]. The reduction of turbine masking caused by the reduction of the number of stages combined with a more unstable lean combustion leads to an increase of combustion noise that is expected to compete even more with jet noise at low frequencies. Having more loaded turbine rows yields also to more intense tonal and broadband turbine noise, often shifted to more annoying frequency bands.

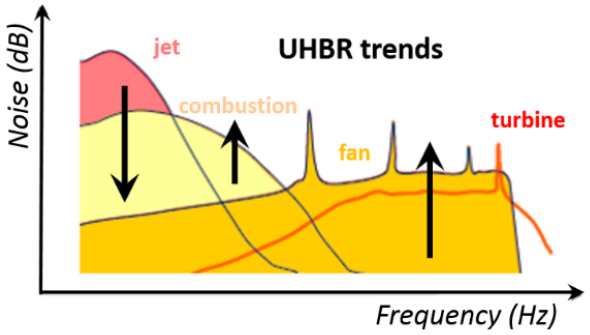

Figure 8: Typical turbofan engine spectrum and future trends for UHBR architectures from Moreau [63].

[3] Ratio between the massflow rates of the by-pass flow and core flow

The fan noise is expected to become the main noise source at almost all flight conditions [39]. Indeed, the shorter intake for UHBR turbofans implies an important upstream distortion. Moreover, the reduction of the distance between fan blades and stator vanes amplifies the interaction of fan blade wakes with the OGV/IGV leading edges. Liners integration for the reduction of noise frequencies is also more constrained. Finally, the modification of secondary flows could produce additional noise sources that are currently considered of secondary importance.

To summarise, the fan stage of turbofan engines is actually responsible for a large part of the noise radiated by an aircraft, whether tonal or broadband, at both approach and take-off operating points. Moreover, the fan noise contribution on future UHBR turbofan engines is expected to be amplified with respect to the other noise sources. Regarding the growth of global air transport sustained by the emerging countries and the more and more stringent ICAO standards, engine manufacturers pay particular attention on the understanding, prediction and control of fan noise. Among the several physical mechanisms generating the fan noise, the tip clearance noise at the tip of fan blades is considered as a secondary source of noise on the current turbofan architectures and not accounted in the fan noise prediction. The evolution towards UHBR architectures may bring the tip clearance noise from a secondary source to a primary one. Regarding this context, the following objectives of the thesis are set:

- Understand the aerodynamic mechanisms generating tip clearance noise in fan stage at approach regimes.
- Evaluate the capacities of numerical methods to predict turbomachinery secondary flows.
- Gather knowledge for the definition of new improved models of tip clearance noise. It is worth mentioning that analytical modelling is beyond the scope of the thesis.

Outline of the manuscript

To address the objectives of the thesis, the outline of the manuscript is presented in Figure 9. Chapter 1 presents a review of the current knowledge on the tip flow phenomenology and tip clearance noise. In addition, a classification of the aerodynamic noise mechanisms and analytical models of the tip clearance noise are provided. The cases of study of Chapters 3 and 4 are also compared to the literature. In Chapter 2, the fundamental and theoretical background of the numerical methods used to compute the tip flow in Chapters 3 and 4 are introduced. The numerical simulations of the tip flows of a single fixed airfoil and a rig-scaled fan representative of an UHBR turbofan are presented in Chapters 3 and 4, respectively. Based on a comparison with experiments, the ability of numerical approaches to recover the aerodynamics and acoustics of the tip flow is evaluated. Finally, in Chapter 5, the tip flows of the isolated airfoil and fan are compared. A dimensional analysis is set up to formulate dimensionless variables characterising the flow physics.

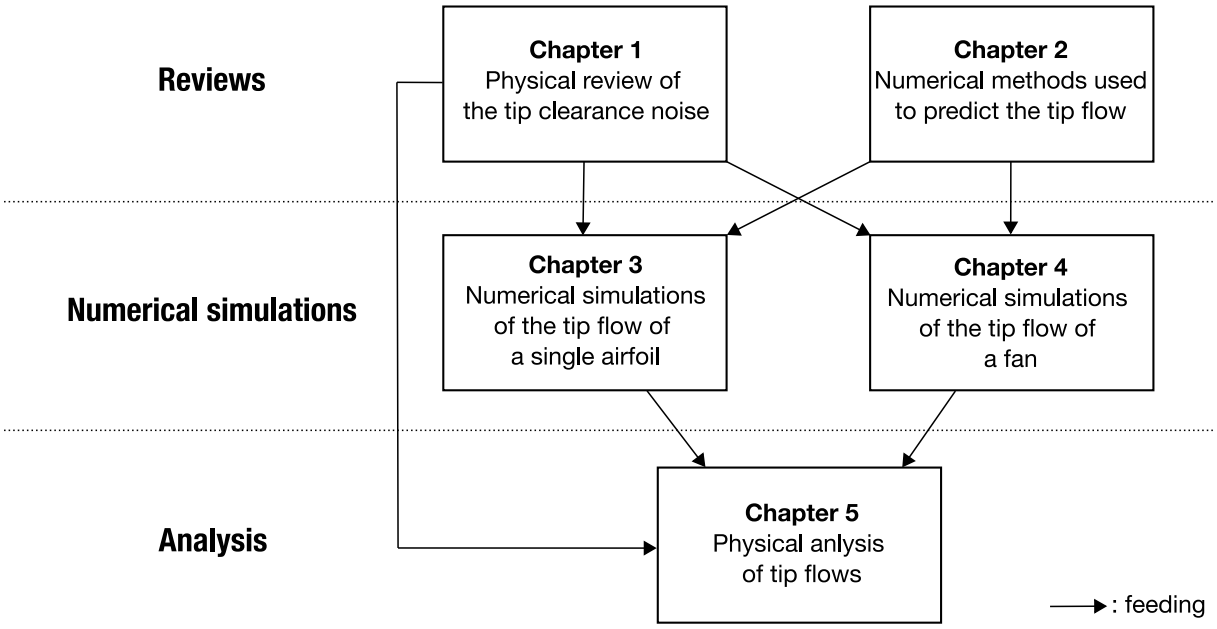

Figure 9: Outline of the manuscript.

1 State of the art of the tip clearance noise

A review of the current knowledge on the tip flow phenomenology and the tip clearance noise is described in this chapter. In addition, a classification of the noise source mechanisms is provided. Then, analytical models of the tip clearance noise are presented. The hypotheses and limitations of the models are described. Since the flow phenomenology differs between configurations, dimensionless parameters of the cases considered in the thesis are compared to the literature. The aim is to assess the representativity of the configuration studied and detailed in this thesis and get hints on the potential source mechanisms.

Contents

1.1 Tip flow phenomenology

In turbomachinery, the rotor tip clearance between the blade and the casing wall induces a Tip Leakage Flow (TLF) across the gap. As illustrated in Figure 1.1, the TLF goes from pressure side (PS) to suction side (SS) due to a pressure difference at the blade tip. At the gap exit, the TLF interacts with the main flow and rolls up to form the Tip Leakage Vortex (TLV). The circulation and size of the TLV increase as it is convected downstream along the suction side edge, until the vortex detaches from the edge and starts moving away from the suction side towards the pressure side of the next blade. After the vortex detaches, its circulation decays since it is no longer fed by the TLF. Finally, the TLV diffuses and can eventually merge with the blade wakes [54]. In the manuscript, it is worth noting that "tip flow" refers to the secondary flow at the blade tip whereas "tip leakage flow" refers to the flow in the gap, almost perpendicular to the chord.

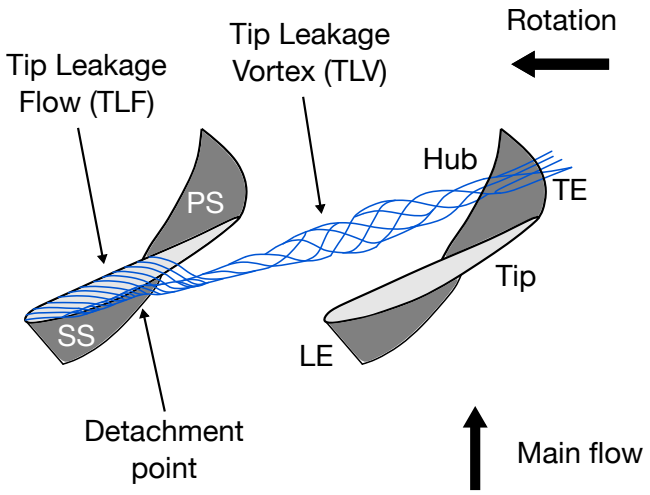

Figure 1.1: Sketch of the Tip Leakage Flow (TLF) and the Tip Leakage Vortex (TLV) at the tip of fan blade viewed from the casing wall. LE: Leading Edge, TE: Trailing Edge, PS: Pressure Side, SS: Suction Side.

With the aim of improving the aerodynamic performance of the axial compressors and turbines, a large amount of studies on the tip flow topology and the associated losses were achieved in the 1990s [62, 8, 89, 43, 50, 49, 83, 55]. Experimental and numerical investigations were conducted on linear cascades and rotors. The description of the flow phenomenology resulting from these studies is first detailed starting by the TLF in the gap. Then, the TLV which is the main phenomenon is presented. Finally, other vortices observed at the blade tip and peculiar flow topologies are described.

1.1.1 Tip leakage flow

At least three types of TLF topologies have been highlighted in the literature and sketched in Figure 1.2. The parameters having an influence on the topology and the range of values on which the phenomena occur are not clear at the present state of knowledge. Nevertheless, the TLF topologies presented in this section are representative of the literature.

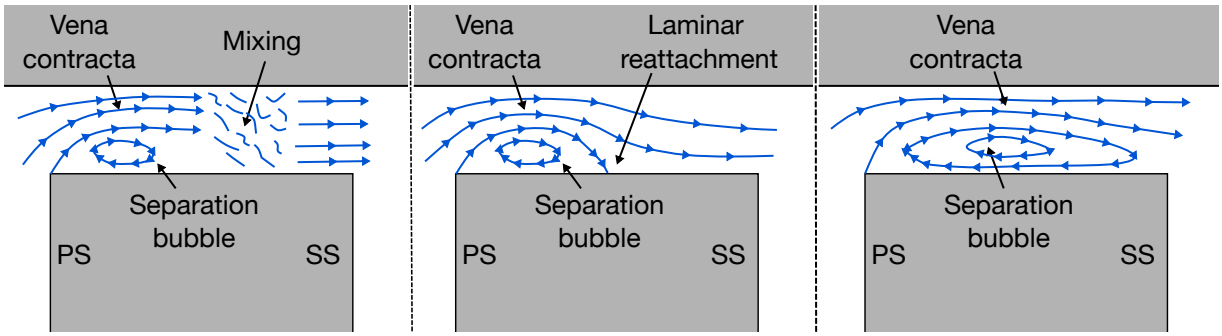

(a) Moore and Tilton [62]. (b) Bindon [8]. (c) Storer and Cumpsty [89].

Figure 1.2: Sketches of the TLF on a plane perpendicular to the camber line for different experiments.

Moore and Tilton [62] studied the flow in the tip gap of a five-blade linear turbine cascade. Measurements of static pressure on the airfoil and the end-wall surfaces and velocity profile at the gap exit were performed. The exit Reynolds number based on axial chord was 4.5×10^5 and the gap height was 2.1 percent of axial chord. Figure 1.2a shows the TLF in the gap described by the authors, the plane of observation being perpendicular to the chord. A vena contracta is observed near the gap entrance. At this point, the flow is at its maximum velocity and the wall static pressure at its minimum. A laminar flow separation occurs at the gap entrance because of the sharp edge. The authors measured a contraction ratio (ratio of the jet width to the gap height) of 0.61 validating the potential flow theory developed by Rains in 1954 [75]. Downstream of the vena contracta, a mixing process occurs with measured static pressure across the gap exit being fairly uniform.

Bindon [8] made a review of the TLF topology from previous measurements on a seven-blade linear cascade to identify and quantify the loss mechanisms. The exit Reynolds number ranged from 2.0 to 3.0×10^5. Wall static pressure and velocity deduced from total pressure were measured. The author summarised that a narrow separation bubble sketched in Figure 1.2b is formed on the pressure side of the flat clearance gap surface. The TLF, almost orthogonal to the chord, travels above the bubble and reattaches behind it to exit the gap.

Alternatively, the TLF could also remain separated from the blade tip as described by Storer and Cumpsty [89]. The authors investigated the TLF in a linear cascade representative of an axial compressors using a combination of experiments and Reynolds-Averaged Navier-Stokes (RANS) computations. The computations were used to explore aspects of the TLF not accessible by the experiments alone. Three different configurations were studied: a first one

with no gap and two others with different gap heights (2% and 4% of chord). The authors observed that the TLF does not reattach along the majority of the chord as illustrated in Figure 1.2c. Also, the authors showed that the magnitude and chordwise distribution of the TLF depend on the static pressure field near the end of the blade.

1.1.2 Tip leakage vortex

At the tip gap exit, the TLF interacts with the main flow and rolls up to form the TLV which is the main phenomenon at the blade tip region. Inoue and Kuroumaru [43] performed detailed measurements of the TLV in two axial compressor rotors of different solidity (1.25 and 1.67 at midspan) and stagger angles (47.2° and 45.5° at midspan). The solidity is defined as the ratio between the chord c and pitch t. The pitch is the distance between two blades in the azimuthal direction. The stagger angle is the angle formed by the blade chord with the axial direction. For each rotor, the gap height was varied from 0.43 to 4.3 percent of chord by changing the diameter of the casing wall to keep the blade geometry constant. The flow structure was characterised by a phase-locked multi-sampling technique with a slanted hot wire in the clearance and a high-response pressure sensor on the casing wall. It was shown that the trajectory and detachment point of the TLV could be recovered from the wall static pressure distribution.

Figure 1.3 presents the ensemble-averaged static pressure on the casing wall for gap heights of 0.42% and 2.55% of chord. The main flow is going from top to bottom and the blades from right to left. The detachment of the TLV is located near the minimum of pressure (isoline -0.6 in Figure 1.3a and isoline -0.5 in Figure 1.3b) and the TLV axis is aligned with the trough of low pressure. With the increase of the tip clearance, the detachment of the TLV moves downstream and the trajectory of the vortex is more inclined toward the azimuthal direction. The authors also concluded that the solidity does not affect the flow pattern substantially except for the interaction of the TLV with the adjacent blade and wake. Storer and Cumpsty [89] gave additional information on the influence of the gap height: the TLV increases in size and strength as the clearance is increased. Besides, the position of the vortex relative to the suction surface is a key factor driving the pressure distribution near the blade tip.

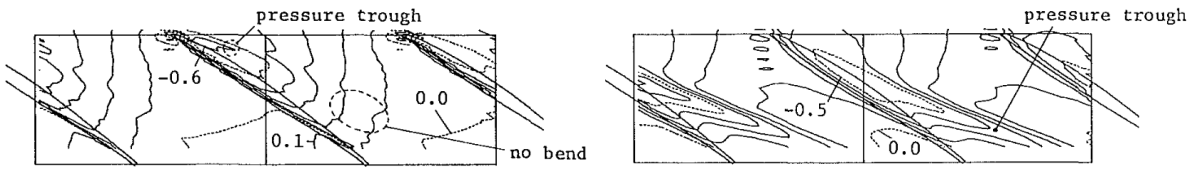

(a) (b)

Figure 1.3: Ensemble-averaged static pressure on the casing wall for gap heights of 0.42% (a) and 2.55% (b) of chord from Inoue and Kuroumaru [43]. The main flow is going from top to bottom and the blades from right to left.

Kang and Hirsch [50, 49] performed measurements on a linear compressor cascade with stationary endwall at design conditions. Tip gap heights of 1.0, 2.0 and 3.3 percent of chord were compared with the no-clearance case. In the second part of the study [49], five-hole probe measurements were used to investigate the TLV process. In their configuration, the TLV has a quasi-circular cross-section with high total pressure and low static pressure. Moreover, the axial velocity profile passing through the TLV center shows a wakelike shape, which is diffusing while moving downstream. The diffusion rate is affected by the wall boundary layer, especially when the vortex center is close to the wall at small clearance. During the TLV evolution, its center is moving away from both the blade suction surface and the endwall approximately linearly with the distance travelled by the TLV.

1.1.3 Other vortices

Nearby the intense TLV, other smaller vortices are observed at the blade tip. Together with the five hole probe measurements, Kang and Hirsch [50] conducted extensive surface flow visualisations. Figure 1.4 presents a multiple vortices structure based on the ink-trace visualisation on the blade tip. In addition to the known TLV, two other small vortices were observed in the tip region: the Tip Separation Vortex (TSV) rolling up because of the separation of the TLF from the pressure side edge and a secondary vortex along the suction side edge having an opposite rotation sense to the TLV. The TSV is consistent with the separation bubble and vena contracta described in Section 1.1.1. Induced vortices located close to the casing wall could also be formed by the important circulation of the TLV.

A horseshoe vortex has also been described upstream the blade leading edge in several studies [83, 43, 50]. This vortex sketched in Figure 1.4 is characteristic of the junction between the blade and the casing wall for a no-gap case and is the result of the scrapping of the casing boundary layer. It is found at small clearances such as 0.43% of chord for Inoue and Kuroumaru [43] and 1% of chord for Kang and Hirsch [50]. Moreover, Sjolander and Amrud [83] observed in their case (0.96% of chord) that the pressure-side leg of the horseshoe vortex is swept over the blade tip within the first 10 percent of the chord length to become part of the TLV. The horseshoe vortex is expected for thick-enough boundary layers compared to the gap height.

1.1.4 Peculiar flow topologies

In some specific configurations, the flow topology at the blade tip does not correspond to the documented literature. For instance, instead of the well-known unique TLV, multiple vortices were observed in the planar cascade of turbine blades of Sjolander and Amrud [83]. In this study, the structure of the tip flow and its effect on the blade loading has been examined for tip clearances ranging from 0.0 to 2.86 percent of chord. A blade was instrumented with 14 rows of 73 static taps and an extensive flow visualisation was conducted using both smoke

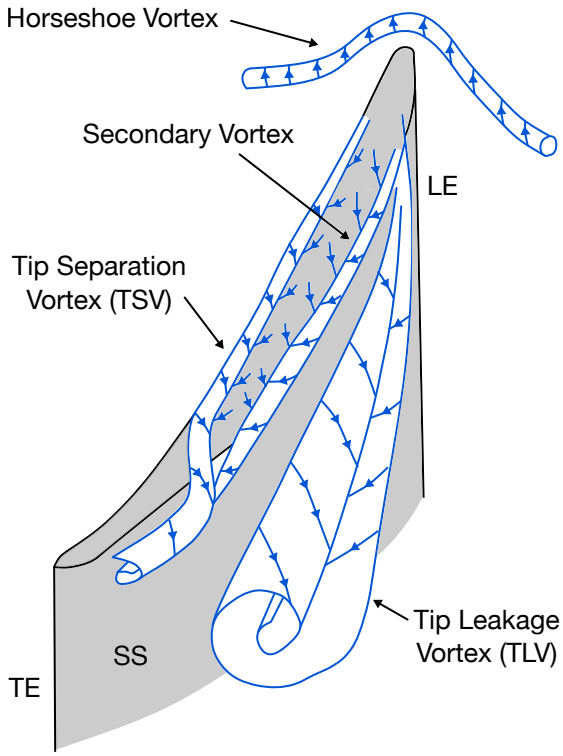

Figure 1.4: Sketch of the vortex structure around the tip adapted from Kang and Hirsch [48].

and surface oil visualisation. Multiple pressure peaks on the suction side close to the tip were measured as the gap height was increased. Three discrete TLVs with their onset located at 20, 60 and 75 percent of chord were identified. Indeed, the second and third vortices did not wrapped around the first one. No singularity of the configuration or the flow regime compared to the other studies are given by the authors.

On the contrary, in the study of Lakshminarayana *et al.* [55], the TLV does not exist. The authors performed rotating five-hole probe measurements in a single-stage axial flow compressor facility. Two-dimensional fields of relative velocity as well as static and total pressures were recorded downstream of the trailing edge along a length of about 20-26 percent of span in the tip region. Instead of rolling up to form the TLV, the TLF of high velocity mixes quickly with the mainstream, producing intense shearing and flow separation. The authors explained that the inlet swirl, high turbulence and high blade loading of this configuration could cause intense mixing of the leakage jet before it could roll up into a discrete vortex.

1.2 Tip clearance noise

The Tip Clearance Noise (TCN) is defined as the noise generated by the blade tip flow. Longhouse [60] conducted in 1978 the first major study of the TCN on an axial ring fan for automotive applications. The fan diameter was 356 mm and was composed of eight equally spaced blades. The noise measurements were made in both free field and reverberant field

environments and the fan backpressure and speed were varied during the tests. Figure 1.5 presents the effect of tip clearance on the overall noise level. The TCN was shown to increase when the tip gap was increased for most of the fan operating points and over the full frequency range.

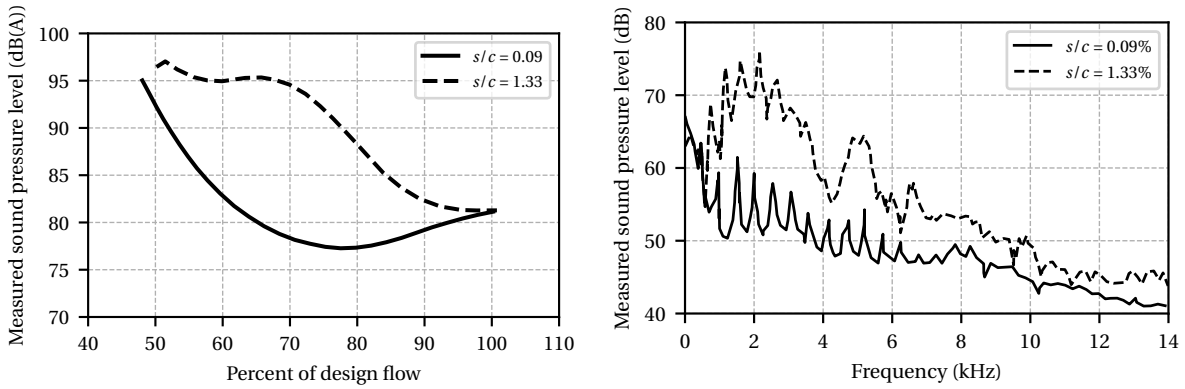

(a) (b) 78% of design flow.

Figure 1.5: Effect of tip clearance on the overall noise level from Longhouse [60].

Then, Fukano *et al.* [28] achieved a systematic experimental investigation of the effects of tip clearance on both noise and performance of four commercially representative low speed fans (three axial and one mixed (axial/radial)). The authors showed that reducing tip clearance both improved performance and reduced noise, not only at the maximum efficiency operating point but also in a low flow rate operating region. Even if the two previous studies gave first information on the TCN, it can be noted that they are not representative of turbofan engines, these studies being mainly focus on automotive applications that are quite far from gas turbine designs.

A study on a Boeing 18-inch fan rig was conducted in 1998 by Ganz *et al.* [29]. The purposes of the test were to identify and quantify the mechanisms including fan broadband noise generation, and to assess the validity of theoretical models on those noise mechanisms. The analysis showed that the TCN is not the major source of noise. However, the gap height could strongly affect the main noise sources such as the rotor self noise [1] and the interaction noise between the casing boundary layer and the rotor tip.

1.2.1 Jet-like tip leakage flow and edges scattering

Jacob *et al.* [45] identified major features of the flow that are candidate source mechanisms. The analysis was based on an experimental study of the TLF of a non-rotating, low Mach number single airfoil configuration. An important gap of 5% of the airfoil chord together with a high angle of attack (15°) to an already cambered airfoil are set. It allows to highlight

[1] The noise measured in the rotor-alone configuration with no boundary layer.

the TCN regarding the other airfoil noise sources while keeping the same generation mechanisms as for smaller gap heights. Particule Image Velocimetry (PIV) in the gap, pressure probes on the wall and microphones in the far-field were used to characterise the aerodynamics and acoustics of the configuration.

Figure 1.6 shows the TCN contribution to the far field noise as a function of the observation angle (directivity) and frequency. The contribution is computed as the difference between the sound measured with and without a gap. Two different frequency domains are highlighted. A medium frequency domain from 0.7 - 3 kHz (St_0 = 2 to 8.6) is underlined with pink ellipses. The Strouhal number St_0 is defined as the dimensionless frequency, based on the chord length c and the inflow velocity V_0. The PSD level varies according to the fifth power of the inflow velocity. Besides, a higher frequency domain (black ellipse) from 3 - 7 kHz (St_0 = 8.6 to 20) is found to vary according to a power of the inflow velocity comprised between 7 and 8. Dimensional analysis in aeroacoustics states that dipoles and quadrupoles have characteristic exponents of 6 and 8, respectively [32]. Both sources are of the same order of magnitude.

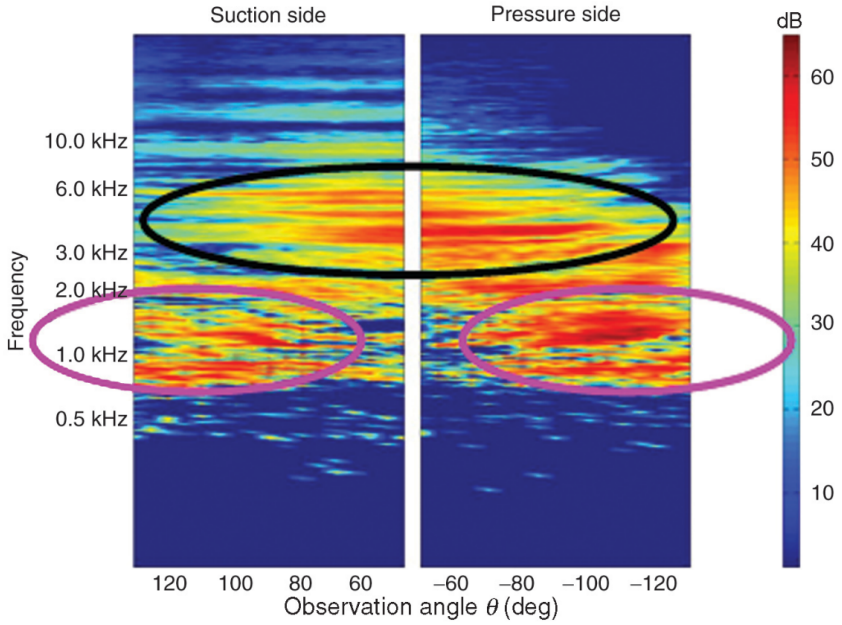

Figure 1.6: Tip clearance contribution to the far field against the observation angle and frequency. The color scale indicates the PSD level in dB-ref 4.10^{-10} Pa^2/Hz from Jacob *et al.* [45].

A sketch of the associated aerodynamic source mechanisms is proposed in Figure 1.7. The medium frequency domain (pink) is related to vortical structures generated by the TLF and then scattered as sound by the tip edge (Figure 1.7a) or the airfoil trailing edge-tip corner (Figure 1.7b). The vicinity of the TLV and the blade trailing edge plays an important role for the existence of this mechanism. Moreover, on a linear cascade or rotor configurations, the TLV could also interact with the trailing edge of the adjacent rotor blade. On the other hand, the high frequency component (black) is emitted by the unsteady motion of small eddies in the jet-like flow. The latter is believed to generate sound when escaping from the gap into

the free flow (Figure 1.7a).

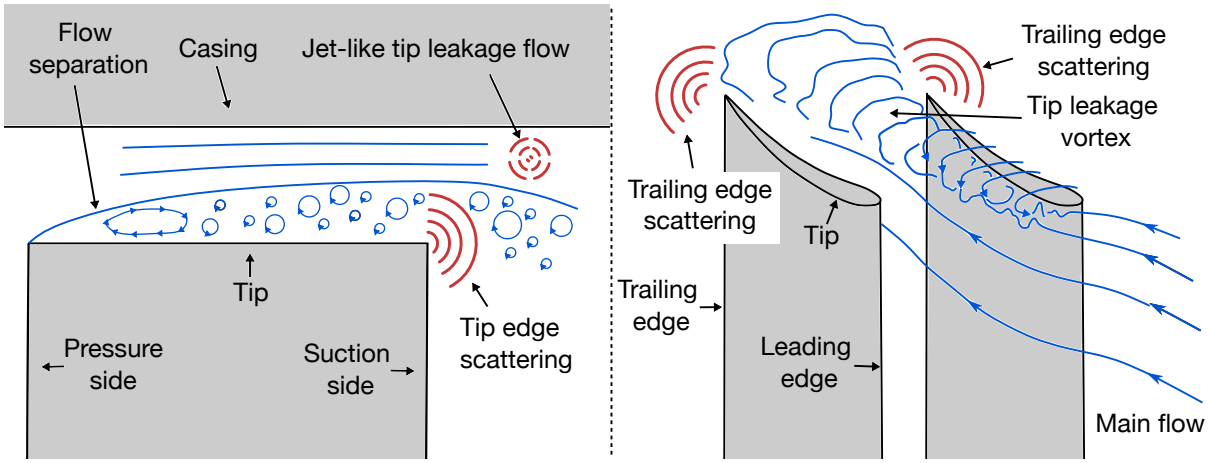

(a) (b)

Figure 1.7: Sketches of the aerodynamic source mechanisms of the TCN in the gap (a) and in the blade passage (b).

Moreover, the production location of the medium-frequency component has been detailed by Boudet *et al.* [12]. Figure 1.8 presents pressure spectra at the airfoil tip in both the experiment and the simulation. A broad hump centred around $St_0 = 3.7$ (1 300 Hz) is observed. The authors proposed a methodology including a wavelet analysis to identify the unsteady phenomenon related to this hump. Using the database from a Zonal Large Eddy Simulation (ZLES) of the isolated fixed airfoil [10], the analysis allowed discerning the blade tip flow separation as the origin of the vortical structures. Previously, Camussi *et al.* [15] also achieved a wavelet analysis on the experimental results of the first campaign and draw the same conclusion.

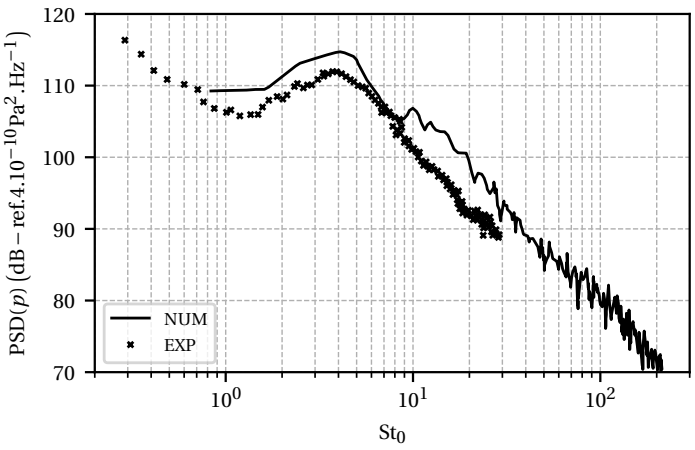

Figure 1.8: Experimental and numerical pressure spectra at the blade tip of an isolated airfoil adapted from Boudet *et al.* [10].

1.2.2 Rotating instability

In addition to broadband noise sources, Kameier and Neise [47] observed significant sound pressure level within limited, almost narrow frequency bands. This component of the TCN is called the Rotating Instability (RI). The experiment was conducted with a low-speed axial compressor with a diameter of 452 mm. The impeller diameter was kept constant throughout the tests, and the tip clearance was varied from 0.7 to 5.6% of blade chord by using casing segments of different sizes. Figure 1.9 shows a sound pressure spectrum in the rotor near field. The RI arises at Strouhal numbers around 1.4 which is below the Blade Passing Frequency (BPF) component (St_0 = 3.3). An interaction mechanism between the RI and the rotor noted as "BPF-RI" in Figure 1.9, is visible around St_0 = 1.9. The RI is observed for tip clearances larger than or equal to 2.8 % of blade chord and at flow rates equal to or smaller than the design flow rate.

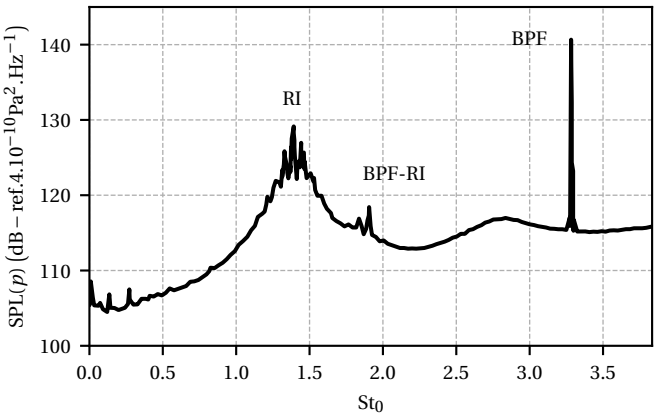

Figure 1.9: Sound pressure level in the rotor near-field at 3000 rpm adapted from Pardowitz *et al.* [69]. RI: Rotating Instability, BPF: Blade Passage Frequency, BPF-RI: Interaction between the RI and the rotor.

Several studies were achieved to confirm the experimentally-observed phenomenon of the RI and have a better understanding of the underlying physical mechanism. März *et al.* [61] performed an Unsteady Reynolds-Averaged Navier-Stokes (URANS) simulation of the same compressor and conducted measurement with high-resolution pressure probes. Then, unsteady flow field was measured by a high-speed PIV system in a single blade passage at several radial positions by Pardowitz *et al.* [69]. Finally, Zhu *et al.* [97] used unsteady aeroacoustic predictions with the Lattice Boltzmann Method (LBM) and conducted a modal analysis of the pressure field to detect rotating coherent flow structures.

To summarise the results obtained in these previous studies, the RI consists of coherent vortical structures coming from the tip clearance and moving in the tangential direction. Figure 1.10 presents the tip vortices filtered in the frequency range of the RI and coloured by pressure fluctuations. The interaction of the structures with the fan blades causes periodic fluctuations of the blade loading, and thus induces tonal noise in the far field. Yet, as

these vortices have a range of tangential velocities, broadband humps are observed instead of sharp tonal peaks. For even lower massflow rate, the instability at the tip spreads over the whole blade resulting into rotating stall[2]. The RI mechanism appearing at off design conditions for large gap heights (> 2-3% of chord) is not expected in the configurations considered in this thesis because the gap height to chord ratio in turbofans are generally lower. The tip flow phenomenology described in Sections 1.1.1 and 1.1.2 is completely changed when the RI occurs.

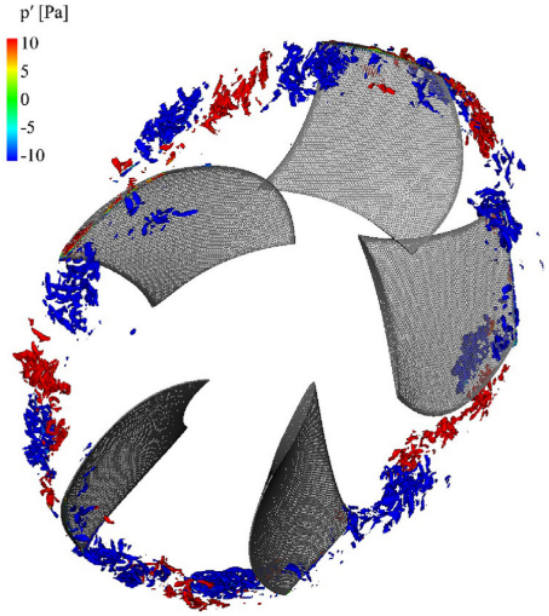

Figure 1.10: Tip vortices visualised with iso-surfaces of λ_2 criterion with a value of -200 s^{-2}, filtered in the frequency range of the RI (340-360 Hz) and coloured by pressure fluctuations from Zhu *et al.* [97].

1.2.3 Tip leakage vortex wandering

Depending on the flow regime, the wandering of the TLV could also be a major contribution of the TCN. Indeed, the periodic oscillation of the vortex may produce tonal noise. Fukano and Jang [27] were the first to describe this noise generation mechanism using two rotating hot-wire sensors on axial flow fans with two different gap heights. In addition to broadband noise due to random velocity fluctuations in the blade passage, a discrete frequency noise due to periodic velocity fluctuations was observed. The peak frequency in the velocity spectrum was proportionally shifted by the increase of the fan rotational speed. The flow rate at constant rotational speed was also shown to have an influence on the characteristic frequencies of the phenomenon.

[2]The rotating stall is a phenomenon of axial compressor flow when a blade row stall in separate patches travels around the compressor annulus.

Moreover, Boudet *et al.* [9] carried out an analysis of the flow in a fan test rig. Figure 1.11a shows a power spectral density spectrum of the axial velocity downstream of the blade tip. The peak observed at $St_0 = 1.0$ is caused by a natural unsteadiness of the TLV as shown in Figure 1.11b. The alignment of the positive and negative isosurfaces along the vortex axis, alternating laterally at nearly constant radius, indicates a lateral oscillation of the TLV. This tonal component dominates the outlet duct acoustic spectrum in this configuration. Such a phenomenon has been visualized by Zierke *et al.* [98], in a high-Reynolds number pump facility. More recently, You *et al.* [95] detected a wandering of the tip leakage vortex in a cascade configuration. The Strouhal number of the peak based on the chord length and the upstream velocity is about unity.

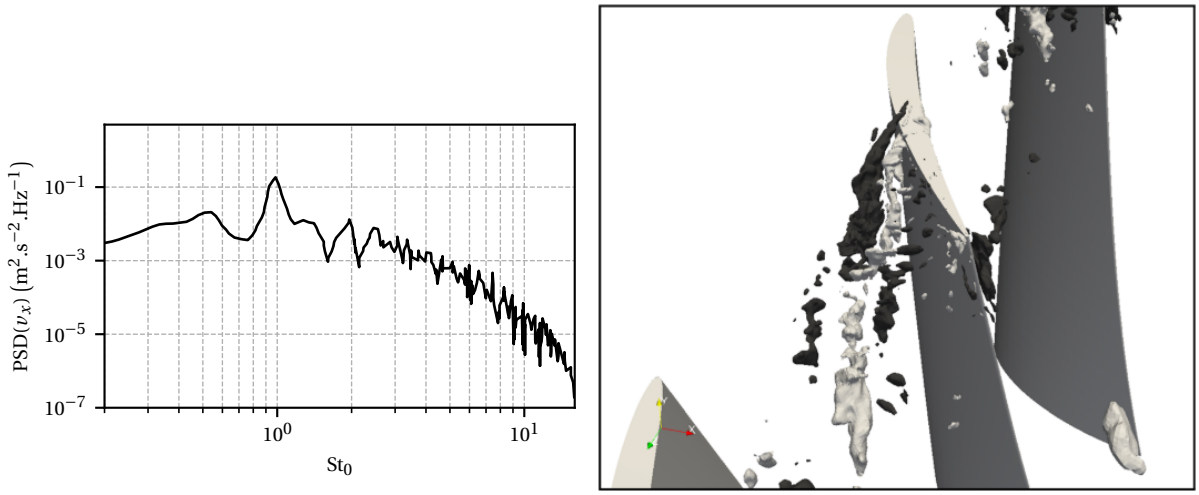

(a) (b)

Figure 1.11: (a) Power spectral density of the axial velocity, in the rotor frame, downstream of the blade tip. (b) Real part of the radial velocity Fourier transform ($St_0 = 1.0$): isosurfaces at -4×10^{-6} m/s (dark gray) and 4×10^{-6} m/s (light gray) from Boudet *et al.* [9].

Boudet *et al.* [9] suggest that the wandering could be a response of the TLV to upstream turbulence from the casing boundary layer and/or the adjacent TLV. However, You *et al.* [95] considered shear-layer instability in the clearance jet flow as the most probable origin of the natural unsteadiness in the cascade configuration. The wandering motion is expected to generate a significant amount of noise when hitting the tip of the adjacent blade. The wandering of the TLV could be a precursor of the RI described in Section 1.2.2.

1.2.4 Rotor tip flow-stator vanes interaction

In 1977, Dittmar *et al.* [24] performed one of the only study on the rotor tip flow-stator vanes interaction noise available in the open literature. A sketch of the corresponding mechanism is presented in Figure 1.12. The rotor tip flow irregularities include both the vortices and the velocity deficits produced by the gap. The mechanism by which rotor tip flow irregularities can generate noise is the same as for the rotor wake mechanism. Namely, the interaction of

the wake with the downstream stator blades induces fluctuating velocities and flow angles on the stator vanes. These, in turn, produce stator lift fluctuations which generate noise. The blade to blade repeatability of this region induces tonal noise and its harmonics while the purely random parts became broadband noise generators. From velocity profiles, the authors concluded the probable significance of the rotor tip flow-stator vanes interaction as a noise source. Later, Dittmar *et al.* [25] installed an outer wall slot between the rotor and the stator to remove the fan tip flow of a 20" diameter model turbofan. A reduction between 2 to 4 dB of the noise radiated has been measured behind the stator.

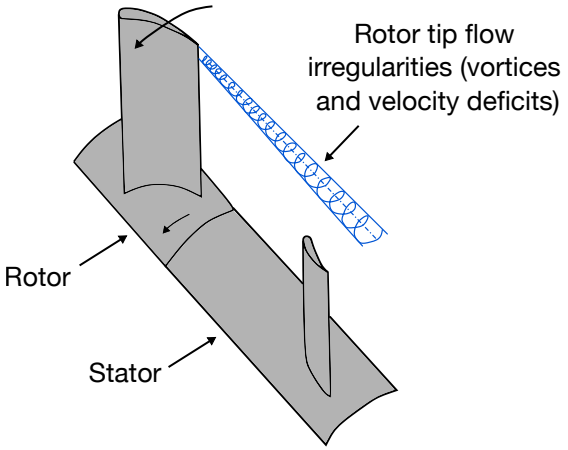

Figure 1.12: Sketch of the interaction noise of the rotor tip flow irregularities with downstream stator vanes from Dittmar *et al.* [24].

1.2.5 Classification of source mechanisms

All the source mechanisms described in this section are summarised in Figure 1.13. They are classified in three categories. Blade self noise sources are due to flow perturbations generated by a blade that are converted into sound by the same blade. When it applies to all the rotor blades instead of one single blade, it is defined as rotor self noise. Lastly, interaction noise sources are due to perturbations convected by the flow and converted into sound when hitting stator vanes. Each mechanism is labelled by a letter. For instance, the jet-like tip leakage flow mechanism is mechanism A. This classification is an overview of the current knowledge on the aerodynamic noise sources of the TCN.

Noise generation by the tip edge and trailing edge are separated into two distinct mechanisms. Even if the aerodynamic mechanism is the same (scattering by a corner), flow turbulences convected on the blade tip and suction side surfaces interacting with edges are disparate. Another possible noise source located at the rotor tip is the interaction of the casing boundary layer with the blade tip. Indeed, the impingement of the turbulent structures in the casing boundary layer on the blade leading edge could produce noise. Even if the gap height has an influence on this interaction mechanism, the turbulent structures responsible

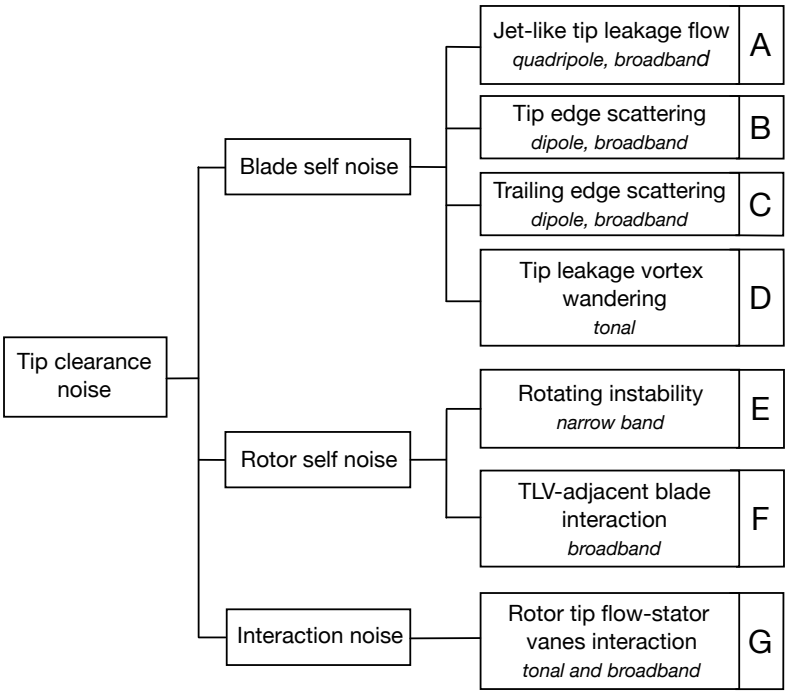

Figure 1.13: Classification of the aerodynamic mechanisms responsible for the generation of the TCN.

for the noise generation are not coming from the TLF itself. For this reason, this source of noise is not considered as part of the TCN in the manuscript.

1.3 Tip clearance noise modelling

The mechanisms of noise production by the tip flow were detailed in Section 1.2. The analytical models to predict the TCN are now presented. A low number of studies in this area of research are available in the open literature, and no analytical model is currently valid for different parameters to the author knowledge. First attempts to model the TCN were proposed by Grilliat in 2008 [35, 34]. The author proposed two models corresponding to different noise generation mechanisms.

1.3.1 Amiet's approach

The first model aims at computing the noise generated by turbulent structures at the airfoil trailing edge (mechanism C in Figure 1.13). Besides the turbulent structures in the airfoil boundary layers, additional structures are generated at the airfoil tip by the tip leakage flow and vortex. The model is based on an extension of Amiet's theory [5, 77, 78] which relies on linearised unsteady aerodynamics theory around an airfoil to predict the far-field noise due to a turbulent pressure gust convected past the trailing edge. The idea is to introduce spanwise attenuated hydrodynamic wavenumbers in order to account for the concentration

of the perturbations in the tip region. Indeed, the assumption of homogeneity in spanwise direction does not hold in this region.

Since the acoustic wavelength stays very large with respect to the airfoil thickness, the blade is assimilated to a zero-thickness, rigid, flat plate. The wavelength is also large compared to the gap height, therefore the gap can be ignored when calculating the far-field sound radiation and the casing wall is considered as a perfect reflector.

The set of coordinates used for the model is depicted in Figure 1.14. The reflecting wall is in the plane (x_1,x_3) and the airfoil is in the plane (x_1,x_2) with a spanwise extent $L/2$ $(x_2 < 0)$ and a chord length c. The mean flow velocity V_0 is assumed parallel to the chord line. The observer is placed at $\boldsymbol{x} = (x_1, x_2, x_3)$ and the sources are located on the airfoil at $\boldsymbol{y} = (x, y)$. Non-dimensional quantities are introduced $X = x/b$ and $Y = y/b$ with $b = c/2$. The incident pressure gust reads $P_0 e^{-iK_1 X} e^{(\alpha - iK_2)Y}$ with $K_1 = \omega b/V_c$ the streamwise non-dimensional wavenumber, V_c the convection velocity of the disturbances and ω the angular frequency. α is the damping factor and K_2 the usual spanwise non-dimensional wavenumber with zero damping.

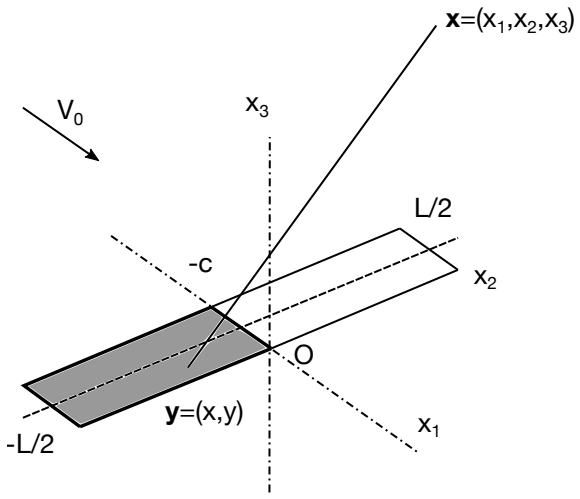

Figure 1.14: Sketch of the set of coordinates used for the adapted Amiet's model adapted from Grilliat's thesis [34].

For the model, the power spectral density of the radiated acoustic pressure in the far-field for the trailing edge noise including the tip flow contribution is defined as

$$S_{pp}(\boldsymbol{x},\omega) = \left(\frac{K x_3 L}{2\pi S_0^2}\right)^2 \frac{1}{b} \int_{-\infty}^{+\infty} \Pi_0\left(\frac{\omega}{V_c}, K_2\right) |I_1(K_2)|^2 \times \left| e^{i\zeta L/(4b)} \operatorname{sinc}\left(\zeta \frac{L}{4b}\right) + e^{i\xi L/(4b)} \operatorname{sinc}\left(\xi \frac{L}{4b}\right) \right|^2 dK_2 \quad (1.1)$$

where sinc is the cardinal sine, $K = \kappa b$, $\zeta = K_2 + i\alpha - K x_2/S_0$, $\xi = K_2 + i\alpha + K x_2/S_0$, κ the

wavenumber and $S_0 = cL/2$. For the expression of I_1, please refer to Grilliat's thesis *et al.* [34]. The function Π_0 is defined as follows

$$\Pi_0\left(\frac{\omega}{V_c}, K_2\right) = \frac{V_c}{\pi}\phi_{pp}(\omega)\, l_y(\omega, K_2) \tag{1.2}$$

where ϕ_{pp} is the hydrodynamic wall-pressure spectra closely upstream of the trailing edge. The coherence length l_y is defined as

$$l_y(K_2, \alpha, \omega) = \int_{-\infty}^{+\infty} \gamma\left(\omega, \eta_2\right) \cos\left(K_2\eta_2/b\right) e^{-\alpha\eta_2/b} d\eta_2 \tag{1.3}$$

where γ is the magnitude squared coherence between two pressure signals closely upstream of the trailing edge and η_2 the spanwise distance between the two. Finally, the wall pressure fluctuations ϕ_{pp}, the coherence length in the spanwise direction l_y, the convection velocity in the streamwise direction V_c and a damping factor α have to be provided to compute the noise radiation.

1.3.2 Howe's approach

The second model aims at computing the noise generated by the TLF when leaving the gap. It corresponds to mechanisms A and B in Figure 1.13. The model has been developped by Dunne and Howe [26] based on Howe's acoustic analogy [37] and the theory of potential flows. The approach of Dunne and Howe [26] models the sound radiated as an upstream vortex ingested by the TLF is expelled from the gap. Additional vorticity is shed into the TLF from the airfoil tip. The noise is then generated both by the ingested and shed vortices passing nearby the airfoil tip suction side as illustrated in Figure 1.15.

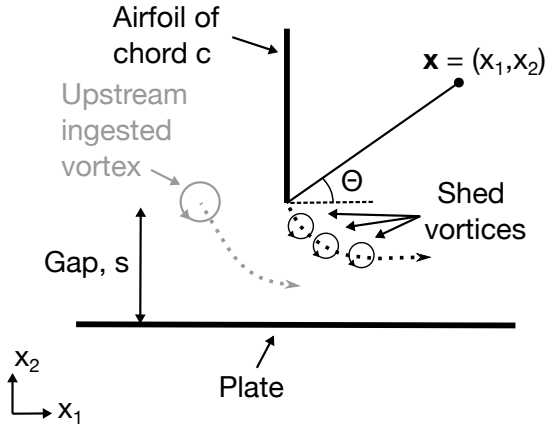

Figure 1.15: Sketch of the interaction noise model of Dunne and Howe [26].

In the case of the TCN of a fan, the sound generated by an upstream ingested vortex is not expected. Therefore, Grilliat [35, 34] proposed that the interaction noise model could be transformed into a self noise model by only taking into account the shed vortices from the

airfoil tip pressure side.

The Howe's analogy for low Mach number flow is formulated as

$$\frac{1}{a_0^2}\frac{\partial^2 h_{tot}}{\partial t^2} - \nabla^2 h_{tot} = \nabla \cdot (\boldsymbol{\Omega} \wedge \boldsymbol{v}) \tag{1.4}$$

with $h_{tot} = h + 0.5 v_i v_i$ the total enthalpy, h the enthalpy and a_0 the speed of sound. Flow velocity $\boldsymbol{v}$ and vorticity $\boldsymbol{\Omega}$ modelled with a distribution of potential vortices have to be provided to compute the source terms of the analogy. Then, the sound radiation is computed using a compact Green function. Finally, the time evolution of the acoustic pressure of an observer located at $\boldsymbol{x}$ is

$$\frac{p(\boldsymbol{x},t)}{\rho_0} \approx \frac{V_c (c/2)^2 \beta \cos\Theta}{2\pi a_0 |\mathbf{x}|} \int_{-\infty}^{+\infty} \mathrm{i}\omega \gamma_0(\omega) F(\omega) \mathrm{e}^{\mathrm{i}\omega[t]} \mathrm{d}\omega \tag{1.5}$$

where β is a constant depending on c and s, $[t] = t - ||\boldsymbol{x}|| / a_0$ the retarded time and V_c the translation velocity of the shed vorticity. $\gamma_0(\omega)$ and $F(\omega)$ are defined in Dunne and Howe [26].

Some limitations are identified. Since a 2D plane perpendicular to the chord is considered in the model, a full prediction of this source of noise is not possible. An extension to 3D could be a piecewise 2D approach, as done by Chen *et al.* [17] for another model, taking into account the chordwise evolution of the velocity and vorticity in the gap. Moreover, the airfoil is considered as a flat plate. Therefore, the effect of airfoil thickness and gap Reynolds number are not considered. The latter could have a strong impact on the flow conditions at the gap exit.

Besides, Howe [38] derived an expression for the acoustic power $\mathscr{P}$ generated by a flow for a low Mach number compact vorticity distribution $\boldsymbol{\Omega}$ in free space in the presence of compact solid surfaces

$$\mathscr{P} = -\iiint_V \rho_0 \left((\boldsymbol{\Omega} \times \boldsymbol{v}) \cdot \boldsymbol{u_a} \right) dV, \tag{1.6}$$

where ρ_0 is the mean fluid density (assumed constant), $\boldsymbol{v}$ the velocity, $\boldsymbol{\Omega} = \nabla \times \boldsymbol{v}$ the vorticity and $\boldsymbol{u_a}$ the acoustic particle velocity. This formula states that sound is generated or dissipated when the scalar product of the Lamb vector $\boldsymbol{\Omega} \times \boldsymbol{v}$ with the acoustic velocity field $\boldsymbol{u_a}$ is non-zero.

1.4 Cases of study

Two kind of cases are considered in the thesis: a single fixed airfoil and a rig-scaled shrouded fan. In order to know where these studies are positioned in terms of relevant parameters, a list of the previously detailed researches on the TCN with several dimensionless parameters is presented in Tables 1.1 and 1.2.

The geometric variables used in Table 1.1 are defined in Figure 1.16. c is the chord length

Authors	Year	Config.	s/c (%)	e/c (%)	c/t	β (°)
Kameier and Neise [47]	1997	Rotor	0.70, 1.4, 2.8, 5.6	7.0	0.36	27
Ganz *et al.* [29]	1998	Rotor	0.62, 1.1, 1.6	2.5	1.2	62.7
März *et al.* [61]	2002	Rotor	0.70, 1.4, 2.8, 5.6	7.0	0.36	27
Fukano and Jang [27]	2004	Rotor	1.6, 3.5	-	0.55	64.2
Jacob *et al.* [45]	2010	Airfoil	0 - 7.5	10	-	0 - 18
Boudet *et al.* [9]	2015	Rotor	5.5	-	0.74	-
Pardowitz *et al.* [69]	2015	Rotor	0.70, 2.8, 5.6	7.0	0.36, 0.74	27
Jacob *et al.* [46]	2016	Airfoil	5.0	10	-	16.5
Zhu *et al.* [97]	2018	Rotor	0.44, 4.4	7.0	0.36	-
Single airfoil	-	Airfoil	5.0	10	-	16.5
Rig-scaled fan	-	Rotor	1.5	-	-	-

Table 1.1: Researches on the TCN and associated dimensionless parameters; geometry.

at the tip, s is the gap height, e is the maximum blade tip thickness, t is the pitch at the rotor tip and β is the stagger angle at the tip. Dimensionless parameters characterising the operating point in Table 1.2 are also introduced. The Reynolds number $\mathrm{Re}_0 = V_0 c/\nu$ and Mach number $\mathrm{Ma}_0 = V_0/a_0$ of the incoming flow at velocity V_0 are computed for all studies. To quantify the speed of rotation of a rotor or the linear translation of a cascade, the Reynolds number $\mathrm{Re}_{tip} = U_{tip} c/\nu$ and the Mach number $\mathrm{Ma}_{tip} = U_{tip}/a_0$ of the linear blade speed at the tip U_{tip} are displayed.

Even if the studies from Longhouse [60] in 1978 and Fukano *et al.* [28] in 1986 deal with the TCN, they are not included in Tables 1.1 and 1.2. Indeed, these studies are focus on automotive applications that are quite far from gas turbine designs.

Studies are considered according to the source mechanisms classified in Section 1.2.5. Mechanism E was studied by Kameier and Neise [47], März *et al.* [61], Pardowitz *et al.* [69] and Zhu *et al.* [97]. The latter are characterised by important gap heights (until s/c = 5%) and very low inlet Mach number (Ma_0< 0.05). Besides, Fukano and Jang [27] and Boudet *et al.* [9] performed studies in the same range of Mach number Ma_0 and observed mechanism D. All studies were performed on rotor configurations except for the two studies of Jacob *et al.* [46, 45] in which mechanisms A, B and C were observed. Gap heights were also important (s/c = 5%) but the inlet Mach number indicated in Table 1.2 (Ma_0=0.20) was much higher than the studies on mechanism D and E. The last configuration from Ganz *et al.* [29] is the

Authors	$Re_0 = V_0 c/\nu$	$Ma_0 = V_0/a_0$	$Re_{tip} = U_{tip} c/\nu$	$Ma_{tip} = U_{tip}/a_0$
Kameier and Neise [47]	1.0 - 2.6 × 10^4	0.01 - 0.03	9.5 × 10^4	0.10
Ganz *et al.* [29]	3.2 - 6.7 × 10^5	0.18 - 0.36	1.3 - 2.4 × 10^6	0.70 - 1.28
März *et al.* [61]	3.2 - 4.2 × 10^4	0.03 - 0.04	2.0 × 10^5	0.21
Fukano and Jang [27]	6.4 - 8.6 × 10^4	0.03 - 0.04	2.6 × 10^5	0.09
Jacob *et al.* [45]	0.3 - 1.2 × 10^6	0.06 - 0.26	-	-
Boudet *et al.* [9]	5.3 × 10^4	0.05	2.2 × 10^5	0.22
Pardowitz *et al.* [69]	1.2 - 4.8 × 10^4	0.02 - 0.05	0.7 - 2.0 × 10^5	0.07 - 0.21
Jacob *et al.* [46]	9.3 × 10^5	0.20	-	-
Zhu *et al.* [97]	2.1 - 4.6 × 10^4	0.01 - 0.03	2.1 × 10^5	0.14
Single airfoil	9.3 × 10^5	0.20	-	-
Rig-scaled fan	4.0 × 10^5	0.20	9.2 × 10^5	0.46

Table 1.2: Researches on the TCN and associated dimensionless parameters; operating point.

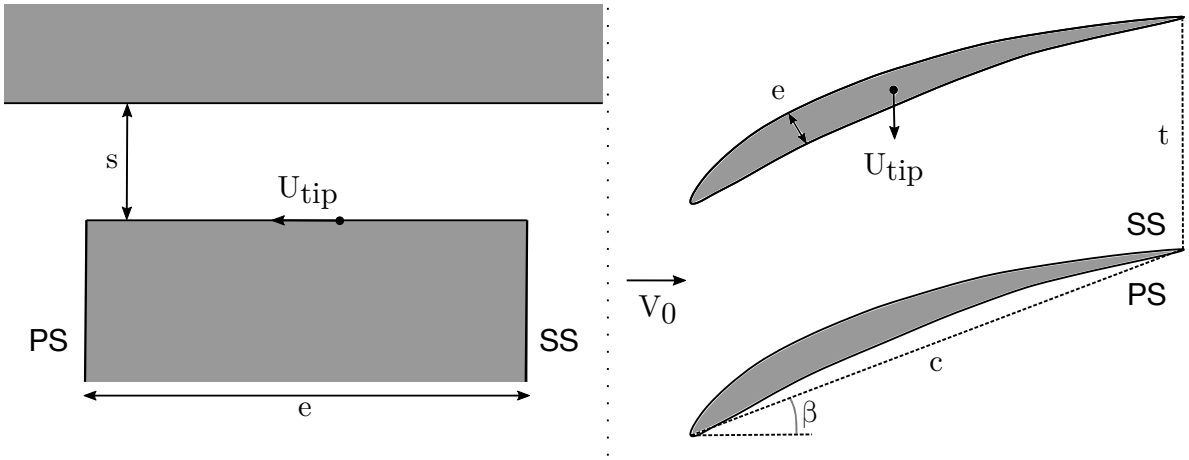

(a) Gap view.

(b) Blade view.

Figure 1.16: Definition of the variables used for the dimensionless parameters in Tables 1.1 and 1.2.

only turbofan case. The authors observed an increase of the noise measured with the gap height but did not detail the source mechanisms.

The single airfoil configuration of the thesis is the same as that of Jacob *et al.* [46, 45]. Therefore, mechanisms A, B and C are expected to occur in the simulations presented in the manuscript. For the fan case, the inlet Mach numbers Ma_0 is much higher than 0.05 and is in

the order of Ganz *et al.* [29]. Therefore, mechanisms D and E are not excepted to occur. Even if the gap height is lower than Jacob *et al.* [46, 45] ($s/c = 1.5 < 5.0$), the inlet Mach numbers are comparable. Therefore, mechanisms A, B and C are expected but less intense. Going from an airfoil to a rotor case could also add mechanism F in the production of TCN.

1.5 Partial conclusions

A review of the current knowledge on the tip flow phenomenology has been achieved in this chapter. The following flow topology is retained: the TLF goes from pressure side to suction side due to a pressure difference at the blade tip. At the gap exit, the TLF interacts with the main flow and rolls up to form the TLV. The circulation and the size of the TLV increase as it is convected downstream along the suction side-tip edge, until the vortex detaches from the edge and starts moving away from the suction side towards the pressure side of the next blade. After the vortex detaches, its circulation decays since it is no more fed by the TLF. Finally, the TLV diffuses and can eventually merge with the blade wakes. The TLV is the main vortex in this region but other vortices may be observed such as the tip separation vortex in the gap and induced vortices.

From this flow topology, noise is produced. Therefore, a review has been made on the mechanisms responsible for this noise production. The following mechanisms were retained:

- jet-like tip leakage flow,
- tip edge scattering,
- trailing edge scattering,
- tip leakage vortex wandering,
- rotating instability,
- tip leakage vortex-adjacent blade interaction,
- rotor tip flow-stator vanes interaction.

A classification of the source mechanisms of the TCN was proposed. The latter were sorted out by blade self noise, rotor self noise and interaction noise. Further studies should be useful to confirm the mechanisms and improve the classification.

Two analytical models of the TCN were presented. The first model aims at computing the noise generated by turbulent structures at the airfoil trailing edge and is based on an extension of Amiet's theory. The second model aims at computing the noise generated by the TLF when leaving the gap. The model is based on Howe's acoustic analogy and the theory

of potential flows. The models are first drafts and a clear lack of knowledge exists in the literature.

The single fixed airfoil and rig-scaled fan cases considered in the thesis were compared to the literature in terms of dimensionless parameters. The aim was to get an idea on the potential source mechanisms found on the configurations. The jet-like tip leakage flow and edge scattering are the most plausible mechanisms for the airfoil and fan. The interaction of the TLV with the adjacent blade may also produce noise in the fan case.

2 Numerical methods

The fundamental and theoretical background of the numerical methods used to compute the tip flow are now presented. The purpose is to provide the knowledge for the analysis of the numerical results when compared to other methods such as experiments.

Contents

2.1 Equations of fluid dynamics

The compressible Navier-Stokes equations for a non-reactive, mono-species gas in conservative form [30] are

$$\frac{\partial \rho}{\partial t} + \frac{\partial \rho v_j}{\partial x_j} = 0, \tag{2.1}$$

$$\frac{\partial \rho v_i}{\partial t} + \frac{\partial \rho v_i v_j}{\partial x_j} = -\frac{\partial p}{\partial x_i} + \frac{\partial \sigma_{ij}}{\partial x_j}, \tag{2.2}$$

$$\frac{\partial \rho E_{tot}}{\partial t} + \frac{\partial \rho E_{tot} v_j}{\partial x_i} = -\frac{\partial p v_j}{\partial x_j} + \frac{\partial \sigma_{ij} v_i}{\partial x_j} - \frac{\partial q_j}{\partial x_j}, \tag{2.3}$$

where t is the time variable, x_i the spatial coordinates, ρ the density, v_i the three components of the velocity vector $\boldsymbol{v}$, p the pressure, $\rho E_{tot} = p/(\gamma-1) + 0.5\rho v_i v_i$ the total energy per unit volume. $\gamma = c_p/c_v$ is the specific heat capacity ratio with c_p and c_v the specific heat capacities at constant pressure and volume, respectively. External forces such as gravity force are not considered. Gravity effects are several order of magnitude lower than pressure and viscous forces effects. As well, source terms in the equations of total energy required for reacting flows are not considered.

The system can be completed by using the perfect gas equation of state $p = \rho r T$ with $r = c_p - c_v$ the specific gas constant. Since the variation of the specific ratios with temperature is weak and that a mono-species and non-reactive gas is considered in the framework of the thesis, r is considered constant and equal to 287 $m^2.s^{-2}.K^{-1}$ for air.

According to the Stokes' hypothesis (bulk viscosity neglected), the shear-stress tensor for a Newtonian fluid is given by

$$\sigma_{ij} = 2\mu(T)\, S_{ij} - \frac{2}{3}\mu(T)\, S_{kk}\delta_{ij}, \tag{2.4}$$

where S_{ij} are the components of the rate-strain tensor written as

$$S_{ij} = \frac{1}{2}\left(\frac{\partial v_i}{\partial x_j} + \frac{\partial v_j}{\partial x_i}\right). \tag{2.5}$$

The variation of the dynamic viscosity μ with temperature can be accounted for by the Sutherland's law

$$\frac{\mu(T)}{\mu(T_0)} = \left(\frac{T}{T_0}\right)^{3/2} \frac{T_0 + S_1}{T + S_1}, \tag{2.6}$$

where S_1 = 110.4 K and T_0 = 273.15 K for air. The law is valid from 100 K to 1900 K [85]. The heat flux q_j is linked to temperature gradient with the Fourier law

$$q_j = -\lambda \frac{\partial T}{\partial x_j}, \tag{2.7}$$

where $\lambda = \mu c_p/\mathrm{Pr}$ is the thermal conductivity. The Prandtl number Pr is the ratio between the kinematic viscosity $\nu = \mu/\rho$ and the thermal diffusivity $\lambda/\left(\rho c_p\right)$. For the air, Pr is considered constant and equal to 0.72.

2.2 Turbulence modelling

The Navier-Stokes equations are non-linear partial differential equations. The exact resolution of these equations is then difficult. The main problem of the fluid dynamics is the turbulence. Turbulence refers to the time-dependent chaotic behaviour of the flow. It is opposed to laminar flows which are characterised by an organised flow structure. The flow

regime (laminar or turbulent) is quantified with the Reynolds number Re. Indeed, for values below a particular value of Re (depending on the type of flow studied), the flow is laminar whereas it is turbulent for values above. Turbomachinery applications are characterised by high Reynolds number. Therefore, flows considered in the scope of the thesis are fully turbulent. Numerical methods were developed to tackle this problem.

The way the turbulence is treated is a key point of the method. To classify the numerical methods, a spectrum of the turbulent energy is introduced in Figure 2.1. In 1922, Richardson introduced the energy cascade with three characteristic length scales [72]:

- the integral length scale l_I with the corresponding wavenumber κ_I is the size of the largest turbulent structures or eddies;
- the Taylor length scale l_T with the corresponding wavenumber κ_T is a characteristic length scale below which the eddies are affected by the fluid viscosity leading to a dissipation of the turbulent kinetic energy into heat;
- the Kolmogorov length scale l_K with the corresponding wavenumber κ_K is the smallest dimension of the eddies.

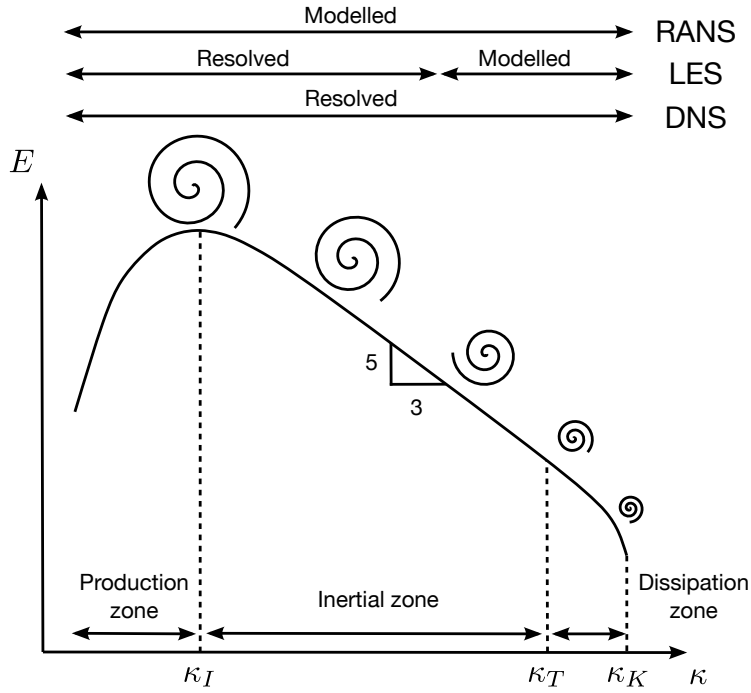

Figure 2.1: Spectrum of turbulent energy of isotropic, homogeneous turbulence with the associated modelling.

From this description of the turbulent length scales, the spectrum can be divided into three regions:

- an energy production zone for wavenumbers below κ_I;

- an inertial zone between κ_I and κ_T. In this region, the energy from large structures is transferred to the smaller structures without dissipation. For large Reynolds number, the production and dissipation process are separated enough and the energy density spectrum evolves as $\kappa^{-5/3}$;

- a dissipation zone between κ_T and κ_K made by small structures under a Joule heating process.

The approach referred as Direct Numerical Simulation (DNS) in Figure 2.1 resolves all the turbulent structures in the flow. On the contrary, the Reynolds-Averaged Navier-Stokes (RANS) formalism models all the structures. Between these two approaches, the Large-Eddy Simulation (LES) method resolves the large eddies and models the small ones. In this thesis, the RANS and LES formalisms were used.

2.2.1 Reynolds-Averaged Navier-Stokes approach

The RANS equations are obtained by time-averaging the Navier-Stokes equations providing a set of transport equations for the averaged momentum. The Reynolds averaging based on a statistical approach consists in decomposing each instantaneous variable X into a mean part $\langle X \rangle$ and a fluctuating part $X^{'}$

$$X = \langle X \rangle + X^{'}. \tag{2.8}$$

$\langle X \rangle$ is the mean quantity using a set average on a large number of realisations. With the property of ergodicity, the set average is equivalent to a temporal average

$$\langle X \rangle = \lim_{T \to \infty} \left(\frac{1}{T} \int_0^T X(t)\, dt \right). \tag{2.9}$$

The time averaging of the fluctuating part $\langle X^{'} \rangle = 0$. When dealing with the compressible Navier-Stokes equations, the Reynolds averaging is much more complex than for the incompressible equations. A Favre averaging (Reynolds averaging weighted according to density) is then introduced to simplify them

$$X = \widehat{X} + X^{''}, \tag{2.10}$$

where

$$\widehat{X} = \frac{\langle \rho X \rangle}{\langle \rho \rangle}. \tag{2.11}$$

Applying the Favre time averaging, the RANS equations are

$$\frac{\partial \langle\rho\rangle\, \widehat{v_j}}{\partial x_j} = 0, \tag{2.12}$$

$$\frac{\partial \langle\rho\rangle\, \widehat{v_i}\, \widehat{v_j}}{\partial x_j} = -\frac{\partial \widehat{p}}{\partial x_i} + \frac{\partial}{\partial x_j}\left(\widehat{\sigma_{ij}} + \sigma_t\right), \tag{2.13}$$

$$\frac{\partial}{\partial x_j}\left(\langle\rho\rangle \widehat{E_{tot}}\widehat{v_j}\right) = -\frac{\partial \widehat{p v_j}}{\partial x_j} + \frac{\partial \widehat{\sigma_{ij} v_i}}{\partial x_j} - \frac{\partial}{\partial x_j}\left(\widehat{q_j} + q_t\right), \tag{2.14}$$

where $\langle\rho\rangle \widehat{E_{tot}} = \widehat{p}/(\gamma-1) + 0.5\langle\rho\rangle \widehat{v_i}\,\widehat{v_i} + \langle\rho\rangle k$ and $\widehat{p} = \langle\rho\rangle r \widehat{T}$. Additional terms of correlations resulting from the averaging appears

- the turbulent kinetic energy, $k = \dfrac{1}{2}\widehat{v_i'' v_i''}$,
- the Reynolds stress tensor, $\sigma_t = -\langle\rho\rangle \widehat{v_i'' v_j''}$,
- the turbulent heat transfer, $q_t = \langle\rho\rangle \widehat{E_{tot}'' v_j''}$.

The three terms account for the effect of turbulence on the mean flow. The number of unknowns is more important than the number of equations. A turbulence model is then provided to close the system of equations. The Boussinesq's hypothesis which is the expression of the Reynolds stress tensor and turbulent heat transfer by gradient laws in the same way to those defined for the mean flow is formulated

$$\sigma_t = 2\mu_t \widehat{S_{ij}} - \frac{2}{3}\left(\langle\rho\rangle k + \mu_t \delta_{ij} \widehat{S_{kk}}\right), \tag{2.15}$$

$$q_t = -\lambda_t \frac{\partial \widehat{T}}{\partial x_j} = -\frac{c_p \mu_t}{\mathrm{Pr}_t}\frac{\partial \widehat{T}}{\partial x_j}. \tag{2.16}$$

Therefore, the modelling of turbulence is reduced to the evaluation of the three following scalar quantities

- the turbulent kinetic energy k,
- the turbulent viscosity coefficient μ_t,
- the turbulent Prandtl number Pr_t.

Generally, the turbulent Prandtl number is considered constant and equal to 0.9 and the turbulent kinetic energy k is computed from the Reynolds stress tensor σ_t. Finally, the modelling is reduced to the computation of the turbulent viscosity μ_t.

Turbulence models

The algebraic models (or zero-equation model) are the first family of turbulence models. The turbulent viscosity is defined according to a mixing length. Even if their predictive value is limited, they have the advantage of a relative robustness and economy. The Baldwin-Lomax model [7] is one of the algebraic models. The second family uses one transport equation of the turbulent viscosity μ_t. The Sparlart-Almaras model [86] is the most famous one. Then, models based on two transport equations are found. In addition to the turbulent kinetic energy k, a second variable such as the turbulent dissipation rate ϵ, the specific turbulent dissipation rate ω or a characteristic mixing length l, is transported in the flow. Then, μ_t is computed from the two transported variables. For instance, in the $k-\omega$ model of Wilcox [93], $\mu_t = \langle\rho\rangle k/\omega$. The transport equations of this model used in Chapter 3 to compute the tip flow of a single airfoil are

$$\frac{\partial\langle\rho\rangle k}{\partial t} + \frac{\partial\langle\rho\rangle k\widehat{v_j}}{\partial x_j} = \sigma_r \frac{\partial\widehat{v_i}}{\partial x_j} - \beta^*\langle\rho\rangle k\omega + \left(\mu + \sigma_k \frac{\langle\rho\rangle k}{\omega}\right)\frac{\partial k}{\partial x_j}, \tag{2.17}$$

$$\frac{\partial\langle\rho\rangle\omega}{\partial t} + \frac{\partial\langle\rho\rangle\omega\widehat{v_j}}{\partial x_j} = \gamma\frac{\omega}{k}\sigma_r \frac{\partial\widehat{v_i}}{\partial x_j} - \beta\langle\rho\rangle\omega^2 + \left(\mu + \sigma_\omega \frac{\langle\rho\rangle k}{\omega}\right)\frac{\partial\omega}{\partial x_j}, \tag{2.18}$$

with $\beta = 0.075$, $\beta^* = 0.09$, $\sigma_k = \sigma_\omega = 0.5$ and $\gamma \approx 0.5532$.

More complex models which are more computational and memory demanding and generally less robust exist. Reynolds Stress Models (RSM) use 7 transport equations and present the most complete classical turbulence models. The first six equations correspond to the Reynolds stress tensor component and the eddy viscosity approach is avoided. The seventh equation corresponds to a turbulent length scale used to compute the dissipation of the turbulence energy.

The RANS approach with the associated turbulence model requires adjustment. Indeed, in each configuration the turbulence intensity and length scales of the structure are different. Then, the appropriate turbulence model has to be chosen and the constants to be tuned. This observation is one of the reason that has pushed the development of other numerical methods such as the Large-Eddy Simulation.

2.2.2 Large-Eddy Simulation approach

Small scale turbulent structures are less affected by the boundary conditions and have more isotropic and homogeneous behaviour than large structures. The LES has been developed on this observation and consists in resolving the large structures and modelling the small ones. In that way, turbulence models are more likely to be more universal. Moreover, small scales carry less energy compared to large scales, thus having less impact on the flow. By modelling a part of the turbulence, the computational cost of the LES is still reduced compared to a

DNS.

Figure 2.2 presents the spatial filtering achieved in the LES approach. The distinction between resolved or modelled turbulent structures is defined by the mesh size. The characteristic length of the mesh is defined as $\Delta = \left(\Delta_i \Delta_j \Delta_k\right)^{1/3}$ with i, j and k the directions. The associated cut-off frequency in the turbulence spectrum is imposed by $\kappa_c = \pi/\Delta$. The mesh acts like a low-pass filter in the wavenumber domain. Spatial scales with a wavenumber lower than κ_c are solved whereas structures with a higher wavenumber are modelled and denoted as subgrid. The cut-off frequency must be ideally set between the integral wavenumber κ_I and the Taylor wavenumber κ_T (defined in Figure 2.1).

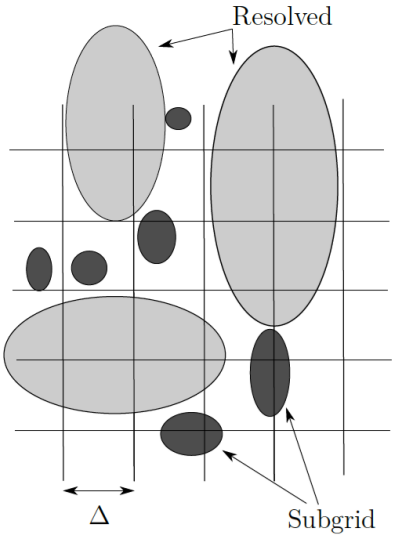

Figure 2.2: Sketch of the spatial filtering achieved in the LES approach due to the mesh from Sagaut *et al.* [79].

Similarly to the RANS formulation, each instantaneous variable is decomposed as

$$X = \overline{X} + X^*, \tag{2.19}$$

but, in the LES formalism, $\overline{X}$ is the resolved part and X^* is the modelled part. It is important to notice that the filtering of the modelled part is not null, $\overline{X^*} \neq 0$. For the compressible equations, a Favre filtering is introduced

$$X = \widetilde{X} + X^{**}, \tag{2.20}$$

where

$$\widetilde{X} = \frac{\overline{\rho X}}{\overline{\rho}}. \tag{2.21}$$

The LES equations based on an eddy viscosity model are

$$\frac{\partial \overline{\rho}}{\partial t} + \frac{\partial \overline{\rho}\ \widetilde{v_j}}{\partial x_j} = 0, \tag{2.22}$$

$$\frac{\partial \overline{\rho}\ \widetilde{v_i}}{\partial t} + \frac{\partial \overline{\rho}\ \widetilde{v_i}\ \widetilde{v_j}}{\partial x_j} = -\frac{\partial \overline{p}}{\partial x_i} + \frac{\partial}{\partial x_j}\left(\overline{\sigma_{ij}} + \sigma_{ij}^{sgs}\right), \tag{2.23}$$

$$\frac{\partial \overline{\rho}\ \widetilde{E_{tot}}}{\partial t} + \frac{\partial \overline{\rho}\ \widetilde{E_{tot}}\ \widetilde{v_j}}{\partial x_j} = -\frac{\partial \overline{p v_j}}{\partial x_j} + \frac{\partial \overline{\sigma_{ij} v_i}}{\partial x_j} + \frac{\partial}{\partial x_j}\left(\overline{q_j} - q_j^{sgs}\right), \tag{2.24}$$

where $\overline{\rho}\widetilde{E_{tot}} = \overline{p}/(\gamma-1) + 0.5\overline{\rho}\widetilde{v_i}\widetilde{v_i} - 0.5\sigma_{ii}^{SGS}$ and $\overline{p} = r\overline{\rho}\widetilde{T}$. $\sigma_{ij}^{SGS} = \overline{\rho}\left(\widetilde{v_i}\ \widetilde{v_j} - \widetilde{v_i v_j}\right)$ is the subgrid scale (SGS) stress tensor and $q_{ij}^{SGS} = \overline{\rho}\left(\widetilde{v_i}\ \widetilde{q_j} - \widetilde{v_i q_j}\right)$ the subgrid scale (SGS) heat flux. The two terms need to be closed. Leonard [56] decomposed the SGS stress tensor into three parts and gave physical interpretation

- $L_{ij} = \overline{\rho}\left(\widetilde{v_i}\widetilde{v_j} - \widetilde{\widetilde{v_i}\widetilde{v_j}}\right)$, the Leonard tensor describing the interactions between the large resolved scales,
- $C_{ij} = \overline{\rho}\left(\widetilde{v_i^{**}\widetilde{v_j}} - \widetilde{\widetilde{v_i}v_j^{**}}\right)$, the cross-stress tensor describing the interactions between resolved and SGS scales,
- $R_{ij} = -\overline{\rho}\widetilde{v_i^{**}v_j^{**}}$, the Reynolds subgrid tensor describing the SGS scales interactions.

Subgrid scale models

The most common models apply the linear Boussinesq approximation for the subgrid scale modelling

$$\sigma_{ij}^{d} = \sigma_{ij}^{sgs} - \frac{1}{3}\delta_{ij}\sigma_{kk}^{sgs} = -2\overline{\rho}\nu_{sgs}\left(\widetilde{S_{ij}} - \frac{1}{3}\delta_{ij}\widetilde{S_{kk}}\right), \tag{2.25}$$

$$q_j^{sgs} = -\frac{C_p\overline{\rho}\nu_{sgs}}{\mathrm{Pr}_{sgs}}\frac{\partial \widetilde{T}}{\partial x_j}. \tag{2.26}$$

The superscript d denotes to the deviatoric part of σ_{ij}^{sgs}. Pr_{sgs} is considered constant and chosen between 0.3 to 0.9. The problem of closure is then reduced to the computation of ν_{sgs} which is local in time and space. A characteristic length l_0 and a characteristic time τ_0 are sufficient to describe the subgrid scales. Indeed, by dimensional analysis: $\nu_{sgs} = l_0^2/\tau_0$. Several models were developed in the past years increasingly incorporating flow effects.

The simplest expression of ν_{sgs} is the Smagorinsky model [84]:

$$\nu_{sgs} = \mathrm{C}_s^2\Delta^2 \mid \widetilde{S} \mid \tag{2.27}$$

where $\mid \widetilde{S} \mid = \left(2\widetilde{S_{ij}}\ \widetilde{S_{ij}}\right)^{0.5}$, $\widetilde{S_{ij}}$ is the resolved strain tensor and C_s is the Smagorinsky constant. Using the local equilibrium hypothesis and assuming a Kolmogorov spectrum, $\mathrm{C}_s \approx$

0.18. The constant is dependent on the flow and ranges from 0.1 to 0.2. The model is overestimating ν_{sgs} in regions with large strain especially in the transition between laminar and turbulent flows. In addition, the Smagorinsky model is not accurate near the wall. Despite the drawbacks, this model is popular due to its simplicity. A damping function to correct the near-wall behaviour is often applied. Some improvements of the Smagorinsky model were made. Lévêque *et al.* [57] enhanced the model by substracting the magnitude of the mean resolved rate of strain to the instantaneous resolved one. The latter is known as the shear-improved Smagorinsky model. Besides, a dynamic procedure can also be set to better model the local structure of the flow. Germano *et al.* [31] designed an algorithm to automatically adjust the constant of the Smagorinsky model at each point in space and each time step. The model is named Dynamic Smagorinsky. Nicoud and Ducros [65] developed a model accounting for the wall named as the Wall-Adapting Local Eddy-Viscosity (WALE) model. The expected asymptotic behaviour $\nu_{sgs} \propto {y^+}^3$, where y^+ is the distance to the wall expressed in wall units, was found combining spatial derivatives of the resolved velocity. An interesting property of the model is that the SGS viscosity vanishes when the flow is two-dimensional as it should.

Nicoud *et al.* [66] noticed that SGS viscosity computed by the WALE model does not vanish for a pure solid rotation. The situation is the opposite for the Smagorinsky model which vanishes for pure rotation but not for pure shear. From the analysis of the singular values of the resolved velocity gradient tensor, the authors derived a SGS model called σ-model. The SGS viscosity for this model is defined as

$$\nu_{sgs} = (\mathrm{C}_\sigma \Delta)^2 \frac{\sigma_3 (\sigma_1 - \sigma_2)(\sigma_2 - \sigma_3)}{\sigma_1^2}, \tag{2.28}$$

where $\sigma_1 \geq \sigma_2 \geq \sigma_3 \geq 0$ are the square roots of the eigenvalues of $g_{ij}g_{ji}$, g_{ij} the velocity gradient tensor and $C_\sigma \approx 1.35$. Finally, the σ-model has the property to automatically vanish in two-dimensional component flow, including the pure shear and solid rotation cases. Moreover, the model shows the appropriate cubic behaviour in the vicinity of solid boundaries. The σ-model is used to compute the tip flows of a single airfoil and a shrouded fan in Chapters 3 and 4, respectively.

2.3 Mesh adaptation

The meshing step of real systems such as turbomachines can be particularly delicate when complex flow physics occurs. Both a significant human time and good experience to refine at first hand interesting regions of such flows are required. Even experienced users are likely to fail especially when dealing with complex and new geometries as usually encountered in a design phase.

To alleviate the inherent difficulties related to this meshing design, a solution-adaptative

procedure to tailor local mesh size and consequently to improve the numerical accuracy of the solution at a given cost is presented in this section. Daviller *et al.* [21] proposed a mesh adaptation based on the averaged kinetic energy dissipation rate to accurately predict pressure losses in complex geometries. Using wall-resolved simulations, the authors showed that two adaptation steps are enough to predict actual pressure losses in a with less than 1% error. Then, Odier *et al.* [68] extended the approach for wall-modelled turbomachinery flows to produce accurate LES predictions. Good turbulence predictions were achieved on a real turbofan stage as soon as a first adaptation was performed, which confirmed the efficiency of the proposed adaptation method.

A metric, *i.e.* ratio between adapted and initial edge sizes, is evaluated from the time-averaged LES prediction. The metric is computed from the normalised wall distance y^+ for cells on the wall and the time-average kinetic energy dissipation rate $\langle\widetilde{\Phi}\rangle$ for the other cells

$$\begin{aligned}
&\text{metric}_{wall} = y^+_{target}/y^+ && \text{for all cells on a wall where } y^+_{target} < y^+,\\
&\text{metric}_{wall} = 1.0 && \text{for all cells on a wall where } y^+_{target} \geq y^+,\\
&\text{metric}_{flow} = \Phi^*(1-\epsilon)+\epsilon && \text{for all other cells,}
\end{aligned}$$

$$\Phi^* = \left[1-\left(\frac{\langle\widetilde{\Phi}\rangle - \langle\widetilde{\Phi}\rangle_{\min}}{\langle\widetilde{\Phi}\rangle_{\max} - \langle\widetilde{\Phi}\rangle_{\min}}\right)\right]^{\alpha}, \qquad \langle\widetilde{\Phi}\rangle = \langle(\mu+\mu_t)\left(\frac{\partial\widetilde{v}_i}{\partial x_j}+\frac{\partial\widetilde{v}_j}{\partial x_i}\right)^2\rangle,$$

where μ is the kinematic viscosity, μ_t the local turbulent viscosity computed by the LES sub-grid scale model, y^+_{target} the target normalised wall distance, α the magnification factor and ϵ the minimum of the metric field in the flow. The magnification factor allows to smooth singularities, to be adapted depending on the configuration under study. Once the metric field obtained, a h-refinement strategy relying on the tetrahedral fully automatic MMG3D library [20] is performed. This procedure is iterative, *i.e.*the simulation has to be stopped and restarted at each adaptation step, and each adaptation step relies on a time-averaged solution,

The mesh adaptation procedure presented in this section is applied to design the mesh for the numerical prediction of the tip flows of an isolated airfoil in Chapter 3 (Section 3.7.2) and a shrouded fan in Chapter 4.

2.4 Wall treatment

Turbomachinery applications are characterised by high Reynolds number. Therefore, the grid requirements especially in the near wall region to perform a simulation could be extreme. For a large industrial compressor, the chord based Reynolds number Re_c is around 2.5×10^6 requiring a heavy cost with a number of boundary layer grid points $N\approx10^9$ [91]. It

is even more important for a fan ($\mathrm{Re}_c \approx 1.0 \times 10^7$, $N \approx 10^{10}$). Only low-pressure turbines are feasible regarding the current computational power with $\mathrm{Re}_c \approx 1.0 \times 10^5$ which requires 10^7 boundary layer grid points. The use of a wall-law to loosen the mesh in the near wall region is a way to alleviate the issue.

Figure 2.3 presents velocity profiles at the wall on fine and coarse meshes. On the fine mesh (Figure 2.3a), the number of points to discretise the velocity profile is sufficient to properly compute the velocity gradient at the wall. Whereas, on the coarse mesh (Figure 2.3b), the velocity gradient at the wall is overestimated. Therefore, the wall shear stress $\tau_w = \mu \partial v / \partial y \,|_{y=0}$ is wrong and a wall treatment is required to impose the correct value.

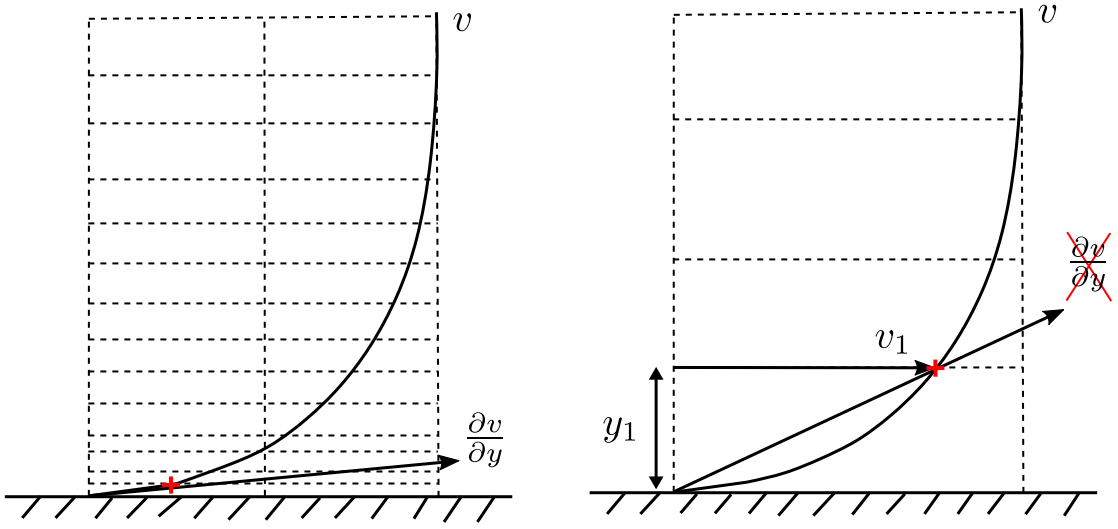

(a) Fine mesh

(b) Coarse mesh

Figure 2.3: Velocity profiles at the wall.

Prandtl [74] and Taylor [90] noticed a similarity region of the velocity profile in the boundary layer and proposed a 2-layer approach to describe this region. Two analytical laws are suggested: a linear layer in the viscous sublayer for $y^+ < 5$ and a logarithmic layer for $30 < y^+$, $y/\delta < 0.3$, with δ the boundary layer thickness [72]. The upper limit of y^+ for the logarithmic layer depends on the Reynolds number. The superscript denotes wall units defined as the non-dimensional wall normal distance $y^+ = y v_\tau / \nu$ and the dimensionless velocity $v^+ = v / v_\tau$ with the friction velocity $v_\tau = \sqrt{\tau_w / \rho}$. From this theory, the first and basic analytical wall-law available in the literature is the log-law

$$v^+ = \frac{1}{\kappa} \ln(y^+) + \mathrm{C}, \tag{2.29}$$

with $\kappa = 0.41$ the von Kàrmàn constant and C another constant. With this relation, the correct shear stress is now computable on the coarse mesh from the mean velocity at the first

grid point. The cost of an analytical law is negligible compared to a numerical iteration. The objective of reducing the computational cost for turbomachinery applications especially in the LES approach, is then achieved. The LES of the tip flows of a single airfoil and a shrouded fan in Chapters 3 and 4, respectively, are performed with a linear law for $y^+ < 11$ and a logarithmic law otherwise. It is worth mentioning that important assumptions on the near wall flow are implied. The theory is valid for stationary 2D flow, attached boundary layer and without pressure gradient [23].

Spalding [88] proposed the following law to only have one single expression for the similarity region:

$$y^+ = v^+ + E\left[e^{\kappa v^+} - 1 - \kappa v^+ - \frac{\left(\kappa v^+\right)^2}{2} - \frac{\left(\kappa v^+\right)^3}{6}\right] \tag{2.30}$$

with $E = 0.1108$. Additional terms can be added to account for pressure gradient, compressible or curvature effects.

Instead of using analytical law, the Thin Boundary Layer Equations (TBLE) can be solved on an embedded grid [13]. The computational cost is 10 to 20% more expensive than an analytical law but remains affordable regarding a LES iteration. The TBLE wall-modelling allows to account for complex effects (pressure gradient, non-equilibrium, convective terms). Finally, a hybrid RANS-LES approach can be used to reduce the computational cost of wall-bounded simulations. For instance, Spalart [87] originally proposed the Detached-Eddy Simulation method. Using the same grid, a RANS turbulence model is used close to the wall and in detached flow region whereas a LES subgrid-scale model is used away from the wall.

2.5 Vortex identification

Flows in turbomachines (fans, compressors, turbines...) are characterized by different vortices developing through the blade and vane passages. These vortices imply aerodynamic losses, stability and noise generation issues. As a consequence, the characterisation of these vortices is major for turbomachine design.

Q, λ_2, Δ criteria [52], commonly used to visualise vortices in numerical simulations, are based on flow velocity gradients. Some other criteria are based on vorticity. These are local quantities including all scales of turbulence. However, major vortices such as the TLV are large scale structures in terms of turbulence. The intermittency induced by the small scales of turbulence makes vortex identification difficult. To overcome the problem, Graftieaux *et al.* [33] proposed the vortex identification functions Γ_1 and Γ_2, derived from velocity fields. These functions are able to characterise large-scale vortex center and boundary, by considering only the topology of the velocity field, not its magnitude.

The first function Γ_1 is defined as

$$\Gamma_1(P) = \frac{1}{S}\int_{M\in S} \frac{(\mathbf{PM} \wedge \mathbf{U_M}) \cdot \mathbf{n}}{\| \mathbf{PM} \| \cdot \| \mathbf{U_M} \|} dS. \tag{2.31}$$

As shown in Figure 2.4, S is a surface surrounding P, M lies in S and $\mathbf{n}$ is the unit vector normal to S. $\mathbf{U_M}$ is the velocity vector at M and $\mathbf{PM}$ is the distance vector between P and M. Γ_1 is dimensionless and $\Gamma_1 \in [-1,1]$. Γ_1 may be interpreted as the normalized angular momentum of the velocity field. The sign of Γ_1 defines the rotation sign of the vortex. $\Gamma_1 > 1$ is for clockwise rotation whereas $\Gamma_1 < 1$ is for anti-clockwise one. The vortex center is defined as the maximum of $|\Gamma_1|$. The integration over surface S acts as a spatial filter.

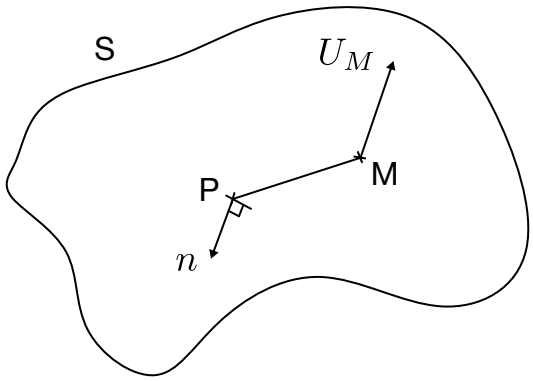

Figure 2.4: Sketch of the set of variables used for the vortex identification functions Γ_1 and Γ_2.

The second function Γ_2 is defined as

$$\Gamma_2(P) = \frac{1}{S}\int_{M\in S} \frac{(\mathbf{PM} \wedge (\mathbf{U_M} - \mathbf{U_P}))\cdot \mathbf{n}}{\| \mathbf{PM} \| \cdot \| \mathbf{U_M} - \mathbf{U_P} \|} dS \tag{2.32}$$

where $\mathbf{U_P} = (1/S)\int_S \mathbf{U} dS$ is the local convection velocity around P. Γ_2 may be interpreted as the relative normalized angular momentum of the velocity field. The vortex core is delimited by the isoline $|\Gamma_2| = 2/\pi$ on S. There are two main advantages of these identification functions: normalisation avoids the question of thresholding and space integration is adapted to the non-local feature of large-scale vortex such as the TLV.

The vortex identification functions Γ_1 and Γ_2 are applied on the TLV of a single airfoil and an UHBR rig-scaled fan in Sections 3.7.1 and **??**.

2.6 Far-field acoustic propagation

Recent advances in computational methods such as LES have enabled the accurate calculation of many time varying flows of practical interest. These methods provide both the unsteady flow and the acoustics inside a computational domain. However, the domain is limited by the computational cost, and usually cannot be extended to the acoustic far field. Furthermore, increasing the size of the computational domain is wasteful because wave propagation outside the flow is well understood and modelled by the linear wave equation. Wave

equations (Lighthill [59], Ffowcs Williams and Hawkings (FWH) [94], Powell [73], etc.) can be used to provide a far field solution given accurate numerical calculations of the source region.

Ffowcs Williams and Hawkings [94] considered a finite volume of space containing a disturbed flow and rigid bodies in arbitrary motion v_s, the surrounding fluid being at rest (Figure 2.5). Bodies and flow generate sound. In that case it is possible, with respect to the sound received at large distances, to replace both the flow and surfaces by equivalent acoustic sources, assuming that the whole medium is perfectly at rest.

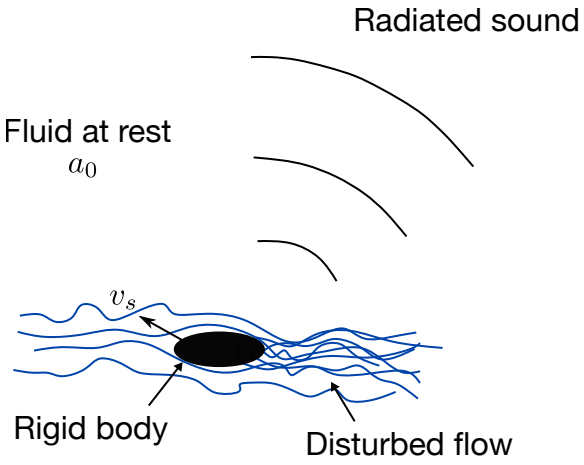

Figure 2.5: Disturbed flow and rigid bodies in arbitrary motion v_s radiating sound in a surrounding medium at rest.

The FWH equation for the fluctuating density $\rho' = \rho - \rho_0$ is

$$\begin{aligned}\frac{\partial^2 \rho'}{\partial t^2} - a_0^2 \frac{\partial^2 \rho'}{\partial x_i^2} = & \frac{\partial^2 T_{ij}}{\partial x_i \partial x_j} \\ & + \frac{\partial}{\partial x_i}\left(\left[\sigma_{ij} - p'\delta_{ij}\right]\delta\left(f\right)\frac{\partial f}{\partial x_j}\right) \\ & + \frac{\partial}{\partial t}\left(\rho_0 v_{s,i}\delta\left(f\right)\frac{\partial f}{\partial x_i}\right),\end{aligned}$$

where ρ, v_i are respectively the density and velocity components of the flow, ρ_0 is the mean density, $v_{s,i}$ is the velocity field of a point on the surfaces, T_{ij} is the Lighthill's tensor ($T_{ij} = \rho v_i v_j + (p' - a_0^2 \rho')\delta_{ij} - \sigma_{ij}$), δ stands for the Dirac delta function, σ_{ij} is the shear stress tensor, p' the fluctuating static pressure and $f(\boldsymbol{x}, t)$ is an equation defining the kinematics of the surfaces. ρ' and T_{ij} are understood in the sense of generalised functions: they are zero inside the mathematical surfaces and equal, respectively, to the density fluctuations and Lighthill's tensor of the flow outside. The equation is exact, as a reformulation of the general equations of fluid dynamics. The left side specifies the propagation of an acoustic wave in a uniform medium with sound speed a_0 using density as the dependent variable. The right side is

frequently referred to as a source term, which contains all the effects that generate acoustic waves.

The density fluctuations in the real fluid, in the presence of flow and rigid bodies, are exactly the same as those that would exist in an equivalent acoustic medium perfectly at rest and forced by three source distributions:

- the first right-side term is a volume distribution in the outer region of the surfaces, due to the flow (quadrupole);
- the second right-side term is a surface distribution due to the interaction of the flow with the moving bodies called loading noise (dipole);
- the third-right side term is a surface distribution due to the kinematics of the bodies called thickness noise (monopole).

The FWH equation is applied on the instantaneous LES wall surfaces of the single airfoil to compute the far-field noise. In that case, the volume source term and the thickness noise are neglected, and only the loading noise is accounted for the propagation. Results are presented in Section 3.9.

3 Numerical simulation of a single fixed airfoil

This chapter is focused on the numerical simulation of the tip flow of a single fixed airfoil. Based on a comparison with experiments, the purpose is to assess the ability of numerical approaches to recover the aerodynamics and acoustics of the tip flow. Following a review of the experimental and numerical database of the configuration, the numerical set-up is presented. Then, several flow aspects are investigated with an extensive study of the tip leakage vortex.

Contents

3.1 Single airfoil configuration

Measurements were performed in the large anechoic chamber of the *Laboratoire de Mécanique des Fluides et d'Acoustique* of ECL[1] [34, 45, 58, 46]. As shown in Figure 3.1a, walls are covered with fiberglass structures to absorb sound and avoid acoustic reflections. Air supplied by a centrifugal fan goes through a series of silencers over several meters and then outputs in the anechoic chamber through a rectangular section of dimensions 560 × 560 mm. A rectangular nozzle in blue in both Figures 3.1a (on the background wall, in the center) and 3.1b is connected to provide the desired output Mach number.

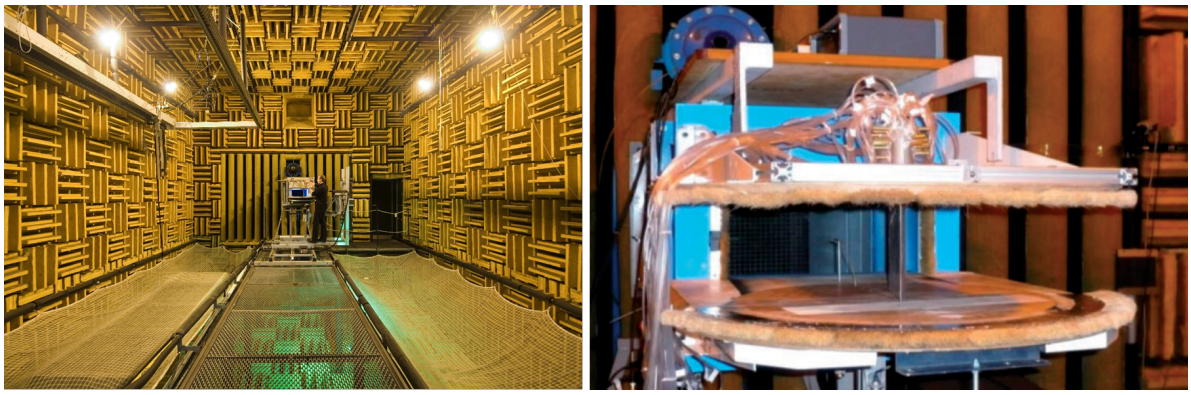

(a) (b)

Figure 3.1: (a) Large anechoic chamber of the *Laboratoire de Mécanique des Fluides et d'Acoustique* viewed from downstream [4]. (b) Picture of the single airfoil configuration showing flexible tubes of wall pressure probes from Jacob *et al.* [46].

Figure 3.1b shows a picture of the single airfoil configuration. It consists in a fixed single airfoil mounted between two flat plates with a gap between the lower plate and the airfoil tip. Sides are open to allow far-field acoustic measurements. Therefore, a rectangular free jet guided by the flat plates exit from the nozzle. The airfoil is placed inside the potential core of the jet to ensure a uniform flow.

Figure 3.2a presents a sketch of the single airfoil configuration. The airfoil is a NACA 5510 of chord c = 200 mm. For a zero angle of attack, the airfoil leading edge is located two chords

[1] *École Centrale de Lyon*

downstream of the nozzle exit. The facility is equipped with an upper turning wooden plate to change the angle of attack. The center of rotation is set at mid-chord. To produce an important TLF to highlight the TCN, important gap heights and angles of attack have to be adopted. The choice of an airfoil with a maximum thickness of 10% of chord allows to avoid flow detachment on the suction side at high angles of attack. The gap height can also be modified by changing the airfoil span. The maximum span is l = 200 mm for the no-gap case.

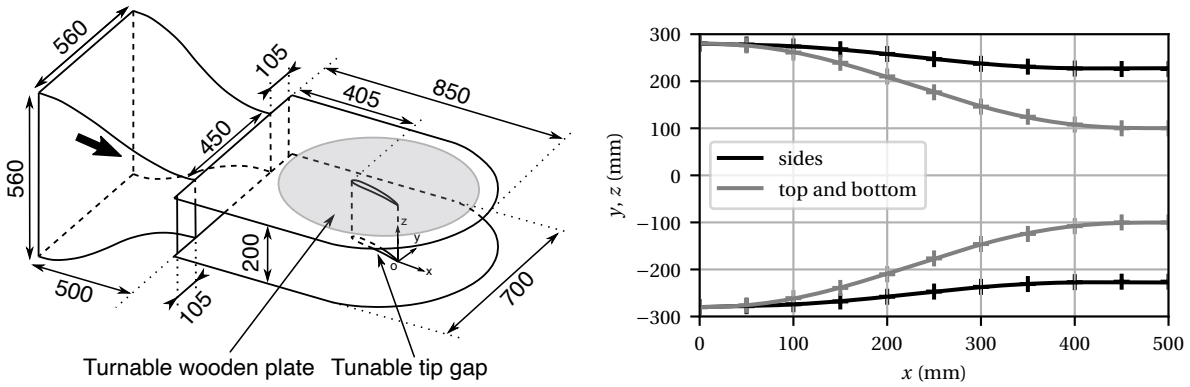

(a) (b)

Figure 3.2: (a) Sketch of the single airfoil configuration with dimensions in millimeters adapted from Jacob *et al.* [46]. (b) Geometry of the nozzle with measurements in plus and extrapolation with hyperbolic tangent function in solid lines.

The geometry of the nozzle is described in Figure 3.2b. Side surfaces are in black solid lines whereas top and bottom ones are in grey solid lines. From the point measurements in plus, a hyperbolic tangent function is used to recover the full curvature of the nozzle. The exit section of the nozzle is rectangular with dimensions 450 × 200 mm. Two shoulders of 105 mm are found at the nozzle exit and could have an impact on the acoustic propagation by modifying the directivity of the waves.

The coordinate system $(O, \boldsymbol{x}, \boldsymbol{y}, \boldsymbol{z})$ used in this study is depicted in Figure 3.2a. The origin, defined at the trailing edge-tip corner, is more appropriate to study the TLV. The $\boldsymbol{x}$ axis is in the streamwise direction. The $\boldsymbol{y}$ axis is in the transverse direction, from pressure side to suction side. The $\boldsymbol{z}$ axis is in the spanwise direction, from the lower to the upper plate.

3.1.1 Experimental campaigns

Two experimental campaigns were carried out on the single airfoil. The first one was performed by Grilliat and Jacob [34, 45] in the frame of project PROBAND in 2009 in which an extensive database was produced. Hot Wire Anemometry (HWA) was performed to characterise the incoming flow between the nozzle exit and the airfoil leading edge. Laser Dopper Velocimetry (LDV) and Particule Image Velocimetry (PIV) were achieved in the TLF and TLV

to measure the flow velocity. In addition, steady and unsteady pressure measurements on the airfoil and casing plate were monitored. Finally, acoustic measurements with an arc of microphones in the far-field were achieved. All the measuring techniques could be used simultaneously to study the causality between the turbulent activity around the airfoil and the noise in the far-field. The authors identified two major flow features that are candidate sources mechanisms: the jet-like TLF and the tip and trailing edges scattering. More details of the mechanisms are given in Section 1.2.1.

The mean flow velocity of the reference case at the exit nozzle was set to $V_0 = 70$ m.s^{-1}, corresponding to a Mach number $\mathrm{Ma}_0 = V_0/a_0 = 0.20$ and a Reynolds number based on the chord $\mathrm{Re}_0 = V_0 c/\nu = 9.3 \times 10^5$. The gap height was $s = 10$ mm and the angle of attack was $\beta = 15.0°$. The influence of the Reynolds number was studied by varying the incoming flow velocity from 20 to 100 m.s^{-1} corresponding to Re_0 from 2.2 to 11.0 $\times 10^5$ and Ma_0 from 0.06 to 0.3. Moreover, the measurements were performed with a range of angles of attack from 0 to 18° to study the impact of the airfoil loading on flow quantities. Finally, the gap height was varied from 0 to 25 mm.

To reduce the background noise of the rig and provide a better signal-to-noise ratio for the acoustic measurements, a second experimental campaign took place. In the first campaign, the facility was equipped with a boundary layer suction device to tune the boundary layer thickness. Indeed, an initial gap between each of the plates and the nozzle lip provided a passive suction device. In the second one, the device was suppressed to have a thinner boundary layer. Therefore, for a nozzle outlet velocity of $V_0 = 70$ m.s^{-1}, the thickness was reduced from 18 mm to 7.5 mm half a chord upstream of the airfoil leading edge. In the second experimental campaign, the boundary layer thickness was then lower than the gap height (10 mm for the reference case) avoiding significant interaction noise between the incoming boundary layer and the airfoil tip. To recover the same distribution of pressure on the airfoil surface, the angle attack was increased up to 16.5°. Moreover, in order to quieten the surrounding jet flow and to reduce low frequency jet oscillations, the nozzle lips and the plate edges were equipped with brushes.

The second campaign was performed by Li and Jacob [58, 46] in the frame of project AXIOOM in 2016. A significant experimental database was produced using time-resolved stereo PIV measurements. Instead of classic PIV in which a laser sheet and a high speed camera are used, stereo PIV requires two high speed cameras. It allows to compute the normal velocity component of the laser sheet. Since stereo PIV is very difficult to tune properly, it was validated against classic PIV and LDV. The rest of the measurements were similar to the first campaign (HWA, wall pressure, LDV, far-field microphone). The results of the first campaign were retrieved by this second test campaign. A low frequency oscillation of the TLV was observed but did not seem to significantly radiate to the far field. Moreover, a hump at medium and high frequencies (0.7 - 7 kHz) was found in the far field (see Figure 3.36).

Table 3.1 sums up the main informations on the experimental campaigns. The simu-

lations presented in this chapter will be validated on the second campaign. This choice is made based on the reduction of the background noise between the two campaigns. Therefore, the operating point of the computations is $V_0 = 70$ m.s^{-1}, $s = 10$ mm and $\beta = 16.5°$.

Authors	Grilliat & Jacob [34, 45]	Li & Jacob [58, 46]
Project	PROBAND	AXIOOM
Year	2009	2016
s	0 … 10 … 25	10
V_0	20 … 70 … 100	70
β	0.0 … 15.0 … 18.0	16.5

Table 3.1: Description of the experimental campaigns on the single airfoil configuration.

3.1.2 Numerical database

Several numerical studies were achieved to reproduce the flow of the single airfoil configuration. The first computation was achieved by Boudet *et al.* [11] using the RANS approach with the solver *Turb'Flow*. This code solves the compressible Navier-Stokes equations using finite volumes, cell-centred approach. The multi-block structured grid was about 5 million points with a mesh resolution at the wall of $\Delta y^+ < 8$ in wall units ($\Delta y^+ < 6$ in the gap). Then, the first grid cell was within the viscous sub-region of the turbulent boundary layer. The turbulence model was the $k-\omega$ of Wilcox with a limiter on the production of k. The inlet boundary condition was located half-chord upstream of the leading edge and the experimental mean and fluctuating axial velocities were imposed. To reduce the computational domain, the surrounding flow was computed as uniform, *i.e.* without the jet. To allow a good agreement with the pressure distribution at midspan, the angle of attack was reduced to 7°. The RANS approach showed a good agreement with the experiment. The wall pressure statistics were modelled using the mean flow and the turbulence parameters from the RANS computation. Therefore, using acoustic models, the airfoil trailing edge noise was predicted and the TCN was partly retrieved when compared to the measurements of the first campaign.

Simultaneously with the second experimental campaign, a ZLES was performed by Boudet *et al.* [10] again with the solver *Turb'Flow*. This method allowed to only use LES in the tip region and in the incoming boundary layer to provide a detailed description of the turbulent dynamics. But, a precise description of the jet shear-layers was not the purpose of the study. Therefore, RANS modelling was used in the rest of the domain in order to reduce the computational cost. The shear-improved Smagorinsky model is used to evaluate the LES subgrid-scale viscosity and the $k-\omega$ model of Wilcox provides the RANS turbulent viscosity. The total grid is composed of 524 structured blocks with 150 million points. The

boundary layer in the gap is resolved with $\Delta y^+ < 1.5$. Since the simulation has been initiated simultaneously with the measurements, the original angle of attack was of 15° with a thin boundary layer. The angle of attack was kept in the simulation but modified to 16.5° in the experiment. The consistency of the experiment and the simulation was checked in terms of incoming boundary layer thickness and airfoil pressure distribution. Within the jet, the development of the incoming boundary layer was simulated by LES over a limited lateral length and repeated periodically in the y-direction up to half a chord upstream the leading edge. The transition to turbulence was induced by a source term that mimics a tripping. Finally, the propagation to the far-field was performed by the FWH acoustic analogy applied on the airfoil surface. The authors managed to retrieve the proper loading on the airfoil with the averaged description of the jet. Moreover, the vortex center and width were quantified. The results confirmed that the tip flow essentially radiates in the central frequency range from 0.7 to 7 kHz (see Figure 3.36).

Recently, Koch *et al.* [51] performed a LES of the single airfoil with the solver *AVBP*, an explicit, unstructured, massively parallel solver [81] which solves the compressible Navier–Stokes equations. For the first time, the convergent nozzle was included in the computational domain. The simulation was compared to the first experimental campaign. The closure of the LES equations was done using the WALE subgrid scale model. The unstructured mesh was composed of tetrahedrons and prisms with a total of 144 million cells. The airfoil and the bottom plate surfaces were meshed with 13 prismatic layers. The wall resolution in wall units was within the range of $\Delta y^+ < 3$ on the airfoil and on the bottom plate close to the tip. The number of points across the tip gap was around 45 (26 prismatic layers and 20 tetrahedra) with a tetrahedral mesh size of 0.4 mm. As achieved by Boudet *et al.* [10], the far-field noise pressure spectra were obtained from the LES with a FWH analogy that radiates the noise pressure fluctuations from the airfoil surface. The authors identified the main noise source from the tip flow. This noise source came from the interaction between the large turbulent structures created inside the tip gap and the suction side tip edge, confirming a previous wavelet analysis [12]. This source was located near the suction side-tip edge around midchord, where large turbulent structures from the TLF exit the gap in two frequency ranges spread around 2 and 6 kHz. Table 3.2 summarises the features of the numerical studies of the single airfoil configuration.

Authors	Boudet *et al.* [11]	Boudet *et al.* [10]	Koch *et al.* [51]
Year	2009	2016	2021
Experiment	1	2	1
Method	RANS	ZLES	LES
Angle of attack	7.0 °	15.0 °	15.0 °
Mesh type	hexahedrons	hexahedrons	tetrahedrons & prisms
Mesh size (10^6)	5	150	144
Wall resolution	wall-resolved	wall-resolved	wall-resolved
Number of elements across the gap	-	-	45
Turbulence modeling	$k-\omega$ Wilcox	$k-\omega$ Wilcox & shear-improved Smagorinsky	WALE
Inlet boundary	half chord upstream LE	half chord upstream LE	nozzle inlet
Surrounding flow	uniform	jet	jet

Table 3.2: Numerical investigations of the single airfoil configuration. LE: Leading Edge.

3.2 Numerical set-up

Different inflow conditions were set to perform the LES of the single airfoil configuration. Boudet *et al.* [10] placed the inlet boundary half-chord upstream of the airfoil leading edge, excluding the nozzle. On the other hand, Koch *et al.* [51] included the nozzle in the computational domain with an inlet boundary at the nozzle inlet. To study the impact of the inflow conditions on the tip flow of the single airfoil, two LES are performed using *AVBP*. The first LES denoted "LES-N&A" computes the flow around the airfoil with the nozzle. In the second LES called "LES-A" , the nozzle is removed. To prescribe the inlet plane of the LES-A, a RANS computation is carried out using the *elsA* software based on a finite volumes, cell-centered approach to solve the compressible Navier-Stokes equations on a multiblocks structured mesh [14]. This simulation is denoted as "RANS" in the following. It is worth noting that the same code *AVBP* has been used for the present work and the study by Koch *et al.* [51], almost simultaneously.

3.2.1 Computational domains

Figure 3.3 presents the computational domains of the three simulations. For the RANS in green, the domain is a rectangle of dimensions $32.5c \times 30c$ composed of three inlet surfaces. The main one is located at the nozzle inlet and the other two are on both sides of the nozzle to set a co-flow with the main jet one. Then, the flow exits at the three other boundaries in the far-field. For the LES-N&A in red, the same inlets are set up but a half disk with a radius of 10c is considered for the outlet. Indeed, the LES boundary condition used at the outlet are more efficient with a flow direction normal to the outlet surface and two corners of outlet boundaries are avoided for the robustness of the computation. Finally, for the LES-A in blue, the same aft part as for the LES-N&A is chosen but the inlet is placed one chord upstream of the airfoil leading edge. Then, only one inlet is found in that case. For the three computational domains, the spanwise extent is the distance between the two plates.

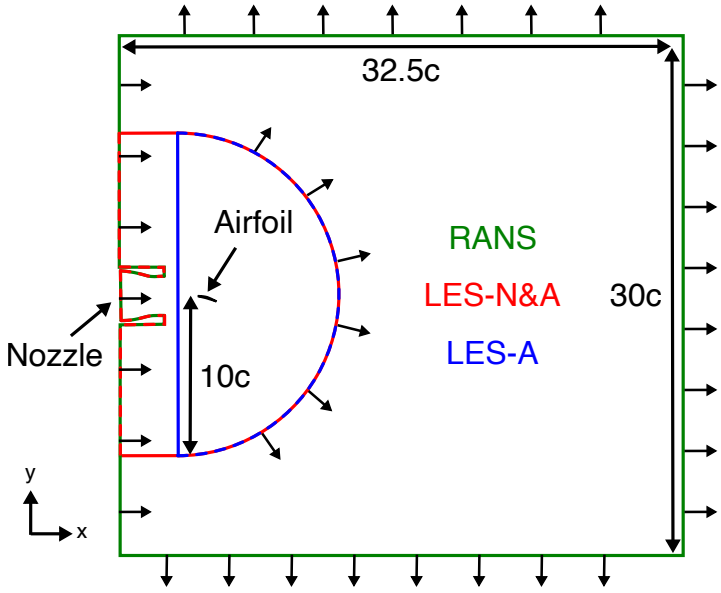

Figure 3.3: Two-dimensional sketch of the computational domains of the RANS in green, LES-N&A in red and LES-A in blue.

3.2.2 Boundary conditions

For all cases, static pressure at the outlet is set at the ambient pressure $P_0 = 97\,700$ Pa. Walls are considered as adiabatic. The quantities imposed on the boundaries for the three cases are summarised in Table 3.3. Inlet boundary conditions specific to each case are presented hereafter.

Cases	Inlet	Outlet
RANS	Nozzle: total pressure and temperature; Co-flow: velocity and static temperature	Static pressure
LES-A	Velocity, static temperature and turbulence	Static pressure
LES-N&A	Nozzle: total pressure and temperature; Co-flow: velocity and static temperature	Static pressure

Table 3.3: Quantities imposed on the boundaries for the RANS, LES-A, LES-N&A.

RANS

Both total pressure and temperature are imposed at the nozzle inlet. Since no loss, work and heat exchange are experienced by the flow through the nozzle, total pressure and temperature are conserved. Moreover, at the nozzle exit, static pressure and temperature are at the ambient conditions (P_0 = 97 700 Pa, T_0 = 290 K). Applying the isentropic relations for a nozzle, the inlet values $P_{tot,in}$ and $T_{tot,in}$ can be computed from the targeted exit Mach number Ma_0 as:

$$P_{tot,in} = P_0 \left(1 + \frac{\gamma - 1}{2} \mathrm{Ma}_0^2\right)^{\gamma/(\gamma-1)}, \tag{3.1}$$

$$T_{tot,in} = T_0 \left(1 + \frac{\gamma - 1}{2} \mathrm{Ma}_0^2\right). \tag{3.2}$$

The flow is imposed normal to the inlet plane. On both side of the nozzle, a co-flow of 1% of the jet velocity V_0 at the ambient temperature T_0 is imposed. A no-slip boundary condition is applied on solid walls.

Turbulent quantities at the inlet $(\rho k)_{in}$ and $(\rho\omega)_{in}$ are also required. The values are computed from the turbulence intensity I and viscosity ratio μ_t/μ using the following relations

$$(\rho k)_{in} = \frac{3}{2} \rho_0 V_0^2 I^2, \tag{3.3}$$

$$(\rho\omega)_{in} = \frac{\rho_0 (\rho k)_{in}}{(\mu_t/\mu)\,\mu_0}. \tag{3.4}$$

Several values of I and μ_t/μ were tested at the nozzle inlet to fit the experimental fluctuating velocity profiles upstream of the airfoil leading edge I = 0.02 and μ_t/μ = 100 were retained.

LES-N&A

Navier-Stokes Characteristic Boundary Conditions (NSCBC) [71] are used at the inlets and outlet to avoid waves reflection in the simulation. The relaxation coefficients are set to 800 at the inlet and 500 at the outlet. It corresponds to a cut-off frequency of 40 Hz for the outlet boundary condition [82]. In practice, f_c separates waves that will be reflected ($f < f_c$) from the ones that will leave the domain ($f > f_c$). The same physical quantities are applied at the inlets as for the RANS. On solid walls, the boundary layer is modelled using a wall law. A linear law is imposed for $y^+ < 11$ and a logarithmic law otherwise [80]. See more details about wall treatment in Section 2.4.

LES-A

Unlike the two previous cases, the inlet for the LES-A is a unique surface on which velocity field and static pressure are imposed. These quantities are extracted from the RANS case. A fully non-reflecting inlet boundary condition is used to inject three-dimensional turbulence while still being non-reflecting for outgoing acoustic waves [22]. The injected synthetic turbulence which is required to trigger the mixing layers is based on Kraichan's method [53]. The turbulence spectrum has a Passot-Pouquet expression [70]. Velocity fluctuations of the injected turbulent field are the ones from the RANS simulation and its most energetic turbulent length scale L_e is set to 6.3 mm. The latter is computed using a property of the Passot-Pouquet spectrum ($L_e = \sqrt{2\pi} L_t$) and the experimental integral length scale L_t (2.5 mm) [46]. A wall law is also applied on solid walls [80]. A linear law is imposed for $y^+ < 11$ and a logarithmic law otherwise [80]. See more details about wall treatment in Section 2.4.

3.2.3 Numerical parameters

RANS

The Roe flux scheme [76] with a second order minmod flux limiter is used. The two-equations turbulence model $k-\omega$ Wilcox [93] defined in Section 2.2.1 is chosen with the Zheng limiter [96]. The Zheng limiter bounds the lowest value of the specific turbulent dissipation rate ω to improve the robustness of the computation. A first order extrapolation is used to treat ω in the near wall region

$$\omega_w = \frac{C\nu}{\beta y_1^2}, \tag{3.5}$$

where y_1 is the distance to the wall of the first cell and C a constant. β is a constant of the $k-\omega$ Wilcox model. A proper convergence of the simulation has only been obtained with this wall damping function.

LES-N&A and LES-A

The Two-Step Taylor Galerkin C (TTGC) numerical scheme [19] is used for the convective fluxes. The spatio-temporal integration is third order accurate in time and space. The 2Δ diffusion operator from Colin [18] is used to compute the viscous fluxes. The unresolved turbulent contributions are modelled with the σ-model developed by Nicoud *et al.* [67] (see Section 2.2.2 for more details). The Colin artificial viscosity model [19] is applied. The 2^{nd} order coefficient is set to 0.1 and the 4^{th} order coefficient to 0.02.

3.2.4 Meshes

RANS

The RANS case is performed on a multiblocks structured mesh. The meshing software *ANSYS ICEM CFD* was used to generate the mesh. A hexahedral mesh is created by first making a blocking which consists in breaking down a geometry into large brick-shapes. The blocking structures the direction of grid lines by the arrangement of the blocks. Then, each block is easily meshed with a pure Cartesian mesh. Block entities are defined by faces and edges which are projected onto the geometry.

Figure 3.4 presents several views of the blocking used for the RANS mesh. The edges projected on curves from the geometry are in green. The edges projected on surfaces are in black and the internal edges are in cyan. The blocking is designed to fit the geometry and also to follow the flow topology. In Figure 3.4a, black lines are inclined to follow the jet deviation and the airfoil wake. A close-up around the airfoil and the nozzle is shown in Figure 3.4b. Two symmetric blocks are used to refine each mixing layer. Moreover, an O-grid block is set up around the airfoil (Figure 3.4c). In the gap, in Figure 3.4d, an internal O-grid block is also used. The main difficulty of this configuration is to combine the blocking for the jet, the airfoil and the gap. The final blocking is composed of 622 blocks.

Figure 3.5 shows cuts of the structured mesh. The mesh is refined at the walls of the nozzle as shown in Figure 3.5a. A geometric law with an expansion ratio of 1.2 is used. The latter is the ratio of the edge length between two successive cells. The mesh size at the wall is 5 μm and the maximum edge size in the nozzle is 10 mm. The same refinement is applied for the plates and the airfoil. The refinement of the mixing layers is gradually loosen to follow their expansion. A maximum edge size of 10 mm is kept in the jet area until $5c$ downstream of the leading edge. Close-ups at the airfoil leading and trailing edges are presented in Figures 3.5b and 3.5c, respectively. The O-grid topology described in the previous paragraph is observable at the leading edge. Figure 3.5d presents a mesh cut in the gap normal to the chord. 60 elements are used to discretise the gap. The spreading of the wall refinement of the airfoil is observed. It results into a total number of about 28×10^6 cells. Even if the current mesh size is larger than the RANS mesh performed by Boudet *et al.* [11], the increase of the

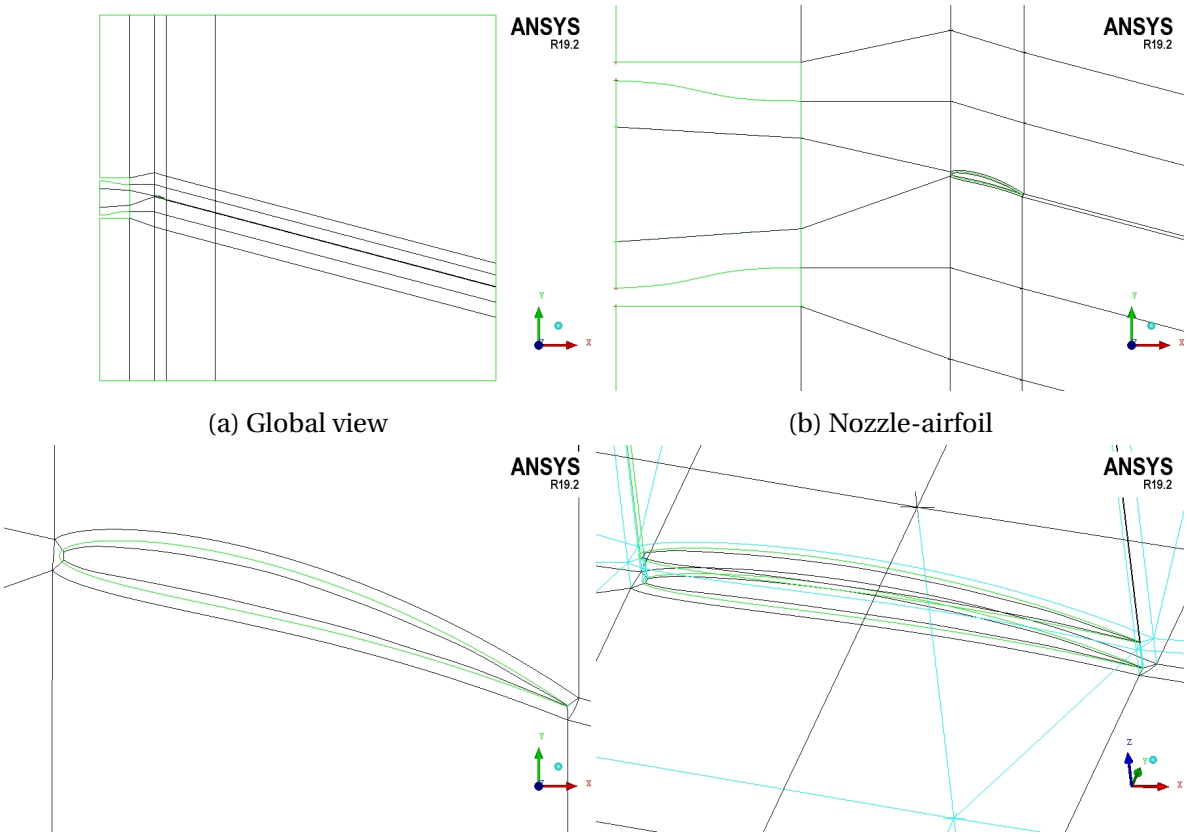

(a) Global view (b) Nozzle-airfoil

(c) Airfoil (d) Gap

Figure 3.4: Views of the blocking for the structured mesh used for the RANS.

computational performance since 2009 allows to keep the same order of return time.

The orthogonality and the aspect ratio are two criteria that measure the mesh quality. The orthogonality is the angle between two contiguous faces of a cell and the aspect ratio is the ratio between the longer and the shorter edges of a cell. In the zones of interest, the orthogonality is higher than 55° and the aspect ratio is lower than 400.

Figure 3.6 presents the wall-normal distance of the first computing point in wall units n^+ on the airfoil and lower plate. n^+ quantifies the mesh resolution at the wall and is equivalent to the classic y^+ in the Cartesian coordinates system. The pressure and suction side surfaces are unwrapped in 2D in Figure 3.6a. The mesh resolution n^+ is below 2 for a major part of the surfaces. This is also valid for the lower plate upstream the airfoil for $x/c < -1$ (not shown here). Larger values until $n^+ = 3$ are identified on the airfoil suction side, close to the leading edge and on the airfoil tip. These values of mesh resolution indicate that the first computing points are located in the viscous sublayer complying with the requirements for wall-resolved RANS simulation.

LES-A

The LES are performed with unstructured tetrahedral meshes. The meshing software *CENTAUR* was used to generate the mesh. Since a direct approach is targeted, *i.e.* computing the

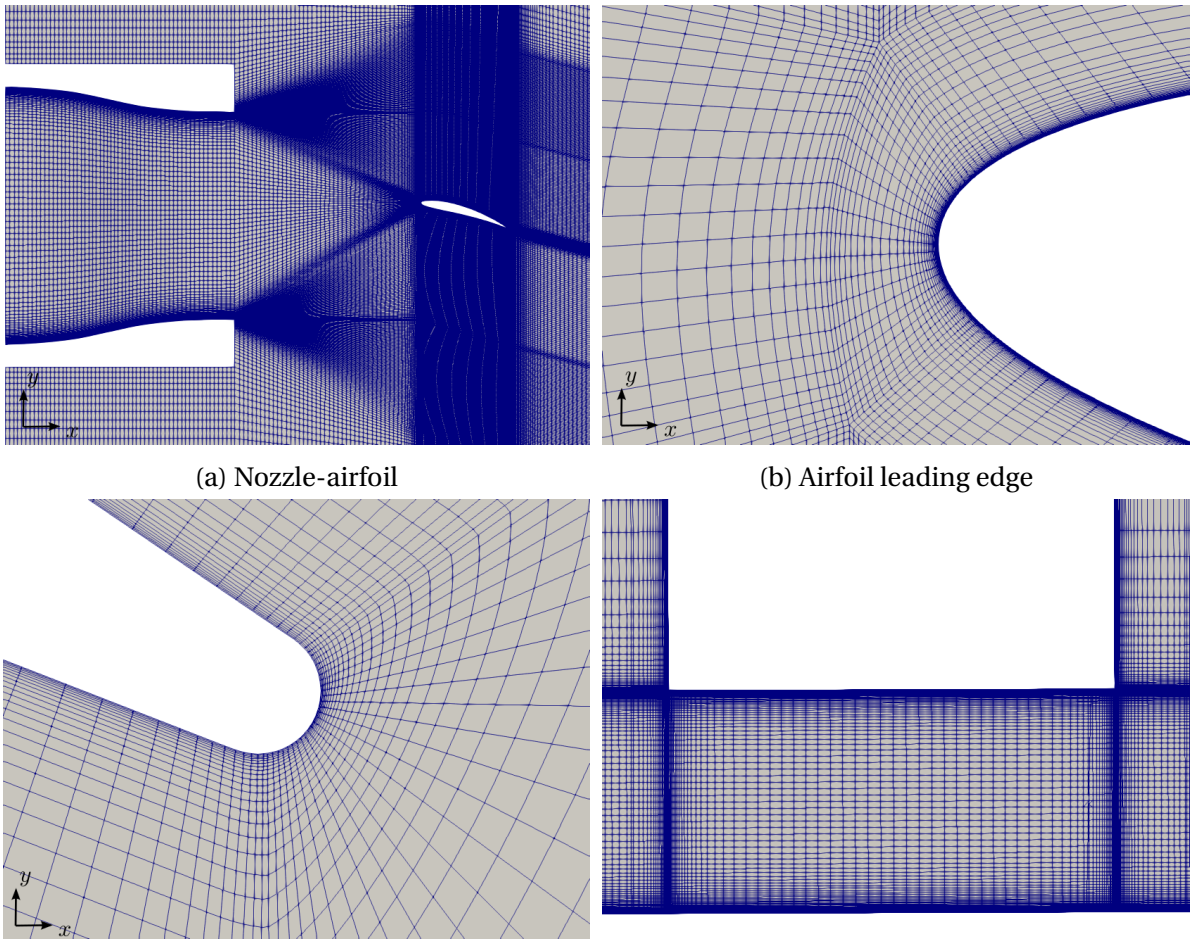

(a) Nozzle-airfoil

(b) Airfoil leading edge

(c) Airfoil trailing edge

(d) Gap

Figure 3.5: Mesh cuts of the structured mesh for the RANS.

sound together with its fluid dynamic source field by solving the compressible flow equations, specific volume mesh sources are set as shown in Figure 3.7. The acoustic propagation zone is a half disk with a radius of 4c in light blue. The maximum edge size inside the zone is 2 mm. Considering that the smallest resolved length scales with the TTGC scheme are equal to 6 times the cell size and that the convection velocity is 70 m.s^{-1}, it leads to a mesh cut-off frequency of 22.8 kHz. The volume mesh source in light green imposes a linear increase of the edge size from 2 to 50 mm to dissipate acoustic waves and avoid production of spurious vorticity. The outer radius of the green volume is 6c. For larger radius around this volume, the edge size is kept constant to 50 mm. On the airfoil and the lower plate surfaces, the edge size is set to 0.5 mm. Cylindrical volume mesh sources are used to refine the leading (LE) and trailing (TE) edges of the airfoil (0.4 mm for the LE and 0.2 mm for the TE). In Figure 3.7, volume mesh sources in red linearly increase the edge size from 0.5 mm on the airfoil surface to 2 mm in the acoustic propagation volume. A red volume source is also dedicated to the refinement of the wake. In the spanwise direction, the volume mesh sources extend until the midspan of the airfoil ($z/c = 0.45$). The mesh is progressively loosen for the airfoil upper part. Finally, the total number of points is 229 $\times$ 10^6 with approximately 70 $\times$ 10^6 dedicated

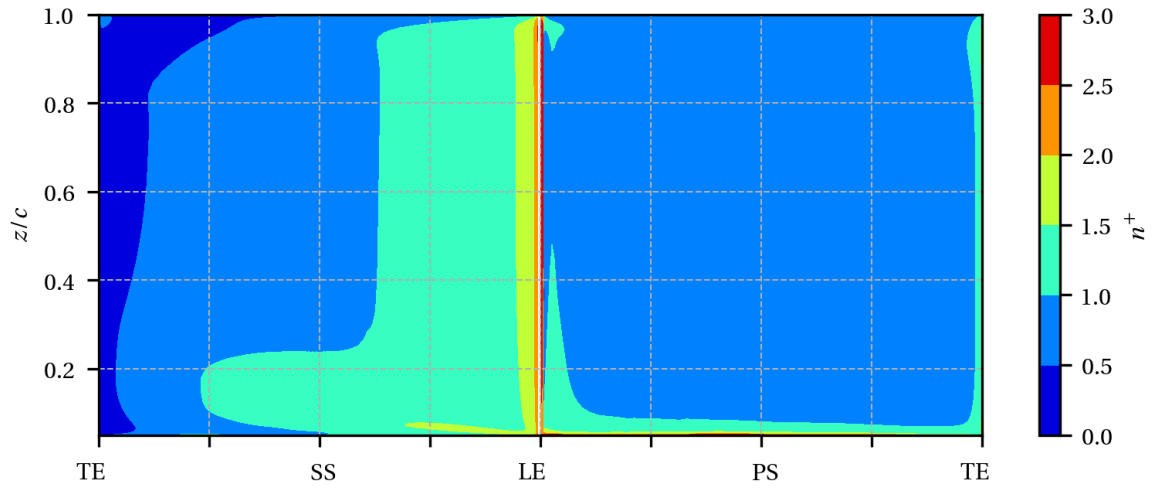

(a) Pressure and suction sides

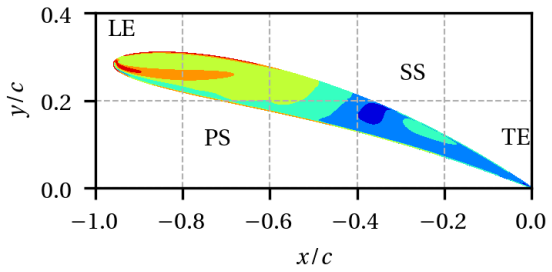

(b) Tip

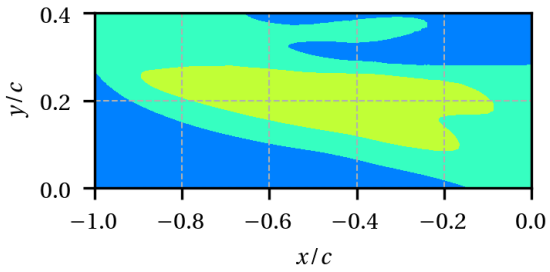

(c) Plate

Figure 3.6: Wall resolution n^+ on the airfoil and lower plate for the RANS. PS: Pressure Side, SS: Suction Side, LE: Leading Edge and TE: Trailing Edge.

to the computation of the acoustic propagation. The current mesh size is then in the same order as the meshes used by Boudet *et al.* [10] (150×10^6) and Koch *et al.* [51] (144×10^6) for which direct acoustic propagation is not achieved.

Figure 3.8 shows several mesh cuts of the unstructured mesh for the LES-A. The smooth evolution of the edge size around the airfoil imposed by the red volume sources is evidenced in Figure 3.8a. The trailing edge curvature is discretised with 4 cells (Figure 3.8c). In the gap (Figure 3.8d), the edge size is constant and equal to 0.5 mm resulting into 20 elements in the gap.

Two criteria are used to measure the quality of the LES-A unstructured mesh: the volume ratio and the equivolume skewness. The volume ratio is the ratio of tetrahedral cell volumes across one face in the mesh. It is equivalent to the expansion ratio used for the RANS structured mesh. The equivolume skewness Q_{skew} is defined as the deviation between the volume of a given tetrahedron V and the volume of an ideal tetrahedron

$$Q_{skew} = \frac{V_{id} - V}{V_{id}}, \tag{3.6}$$

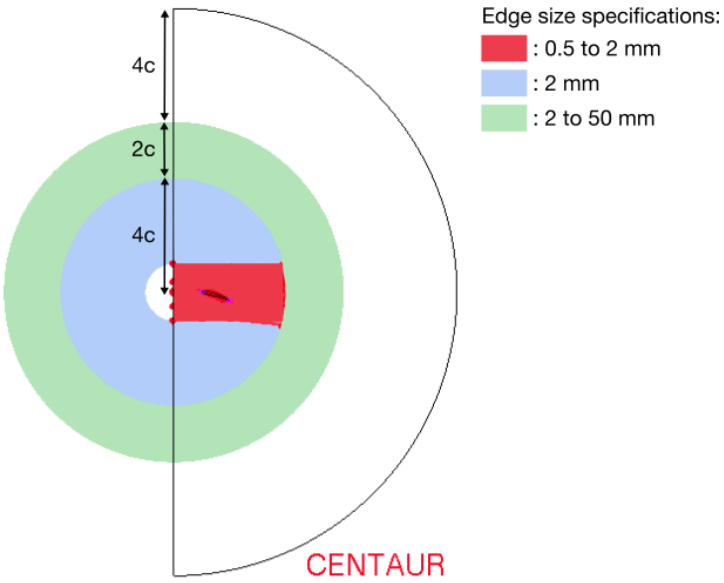

Figure 3.7: Volume mesh sources used to design the LES-A mesh with the meshing software *CENTAUR*.

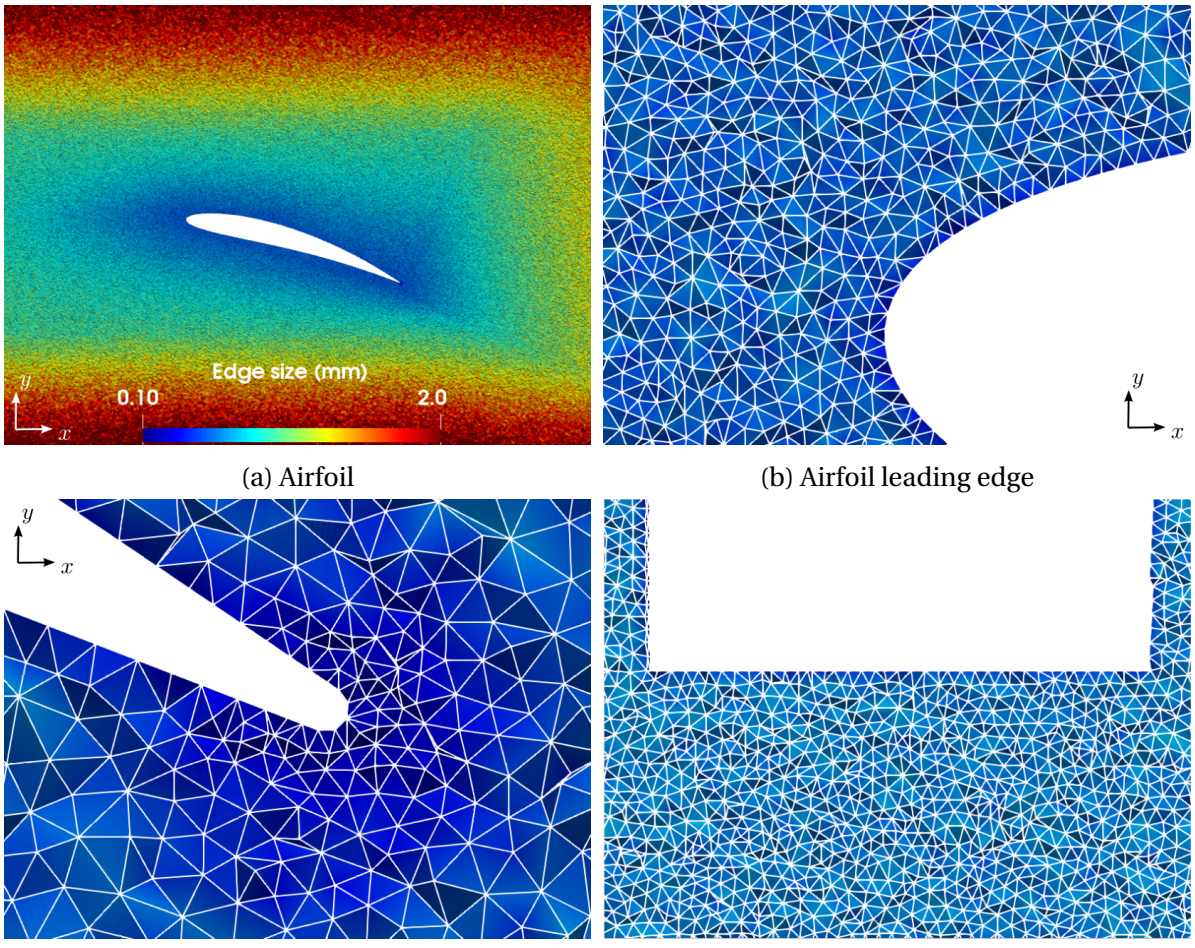

(a) Airfoil

(b) Airfoil leading edge

(c) Airfoil trailing edge

(d) Gap

Figure 3.8: Mesh cuts of the unstructured mesh for the LES-A.

where $V_{id} = \left(8\sqrt{3}/27\right) R^3$, R being the circumsphere radius. The equivolume skewness goes from 0 (ideal tetrahedron) to 1 (zero-volume tetrahedron). The equivolume skewness is lower than 0.998 and the volume ratio is lower than 12 over the whole mesh.

Figure 3.9 presents the mesh sizes s^+, n^+ and r^+ in wall units on the airfoil and lower plate for the LES-A case where (s^+, n^+, r^+) is the local curvilinear coordinate system on the wall. Considering that tetrahedrons on the airfoil surface are ideals, $n^+ = s^+ = r^+$. The pressure and suction side surfaces are again unwrapped in 2D Figure 3.9a. The mesh resolution in the three directions is lower than 150 for the major part of the surfaces. For the incoming flow $x/c < -1$, the resolution is below 50 on the lower plate. The largest values are located in areas where important shear occurs with a maximum value of 200. Values of mesh resolution comply with the requirements for wall-modelled LES [92].

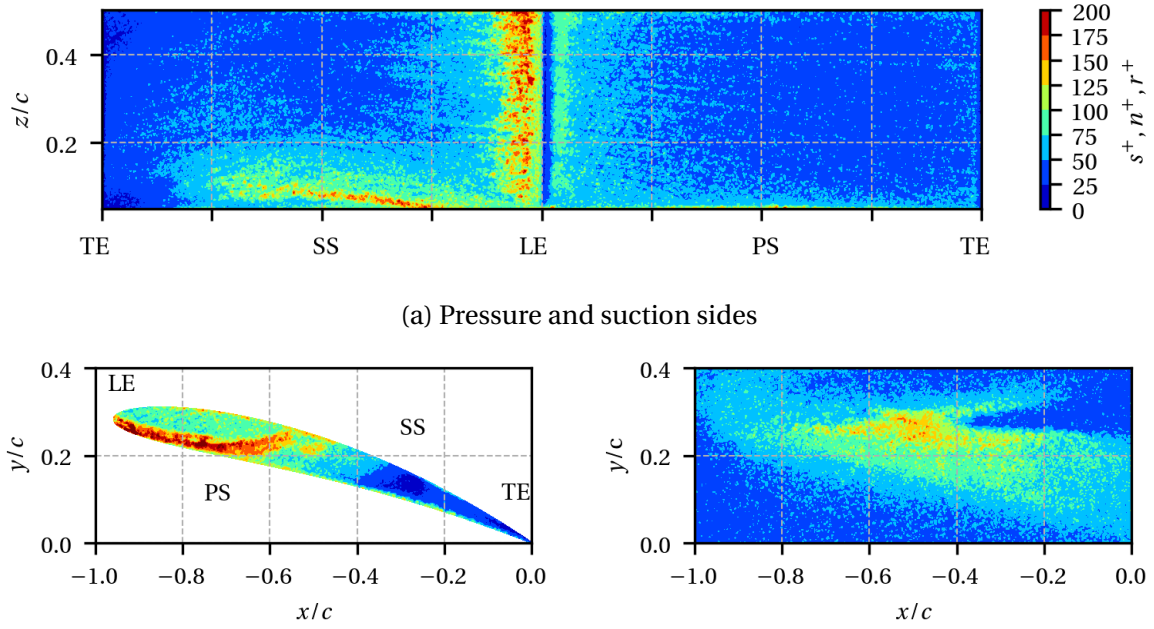

(a) Pressure and suction sides

(b) Tip

(c) Plate

Figure 3.9: Mesh sizes in wall units s^+, n^+, r^+ on the airfoil and lower plate for the LES-N&A and LES-A. PS: Pressure Side, SS: Suction Side, LE: Leading Edge and TE: Trailing Edge.

LES-N&A

The mesh for the LES N&A has been designed based on the LES-A mesh already built.. The modular mesh generation feature of the *CENTAUR* package was used. It allows for an efficient way to generate derivative meshes for a geometry using an already created mesh. This minimizes grid generation and user time. The meshing of the nozzle (and the co-flow) requires 23×10^6 additional tetrahedrons reaching a total number of 252×10^6 elements for the entire mesh. Figure 3.10 presents a plane cut at midspan of the LES-N&A unstructured mesh. The additional part to mesh uses element size information from the previously cre-

ated mesh so that the resulting mesh has smooth transitions across the zone interfaces as shown in Figure 3.10. The aft part of the mesh is the same between the two LES. Therefore, the quality measures and wall resolution are identical to the LES-A mesh.

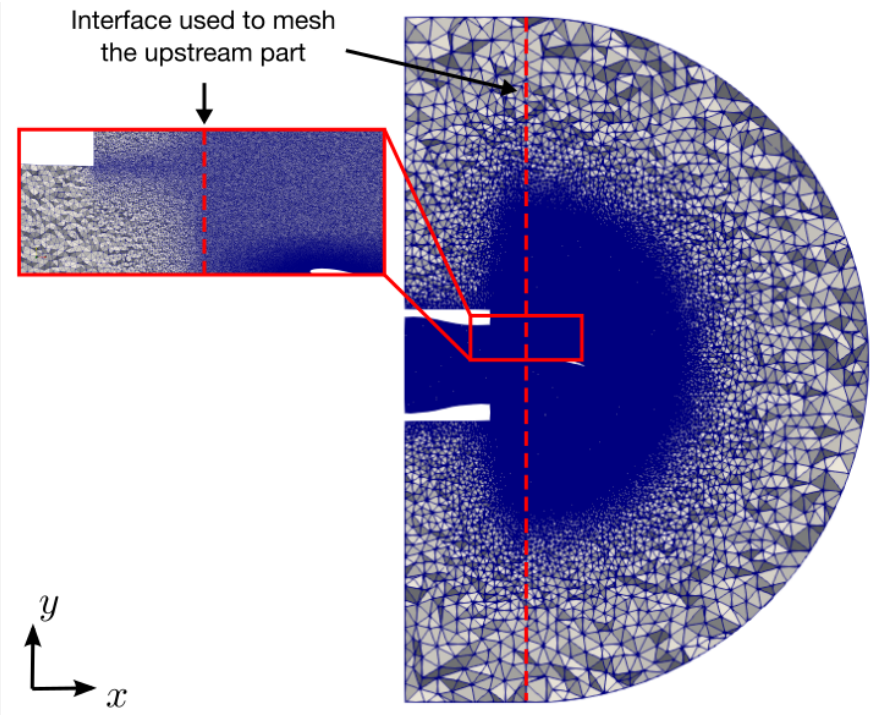

Figure 3.10: Plane cut at midspan (z/c = 0.45) of the LES-N&A unstructured mesh with a close-up on the interface.

Mesh resolution in the gap

Figure 3.11 presents the mesh point distribution across the gap, near the lower plate for the RANS in green and the LES-A in blue. The mesh in the gap is identical between the two LES. The lower plate is at z/c = -0.05. The distribution along z is extracted at x/c = -0.60 and y/c = 0.23. At this location, the mesh resolution on the lower plate is n^+ = 2.0 for the RANS (Figure 3.6) and n^+ = 195 of the LES-A (Figure 3.9). For the RANS, 16 points are below n^+ = 195. Among the 60 elements in the gap for the RANS, 16 elements are then used to compute the plate boundary layer. For the LES-A, this part of the flow is modelled thanks to a wall-law. The same observation is made for the airfoil tip surface. Finally, the same order of mesh resolution in the gap is achieved for the RANS (60 - 2×16 = 28 elements) and the LES-A (20 elements).

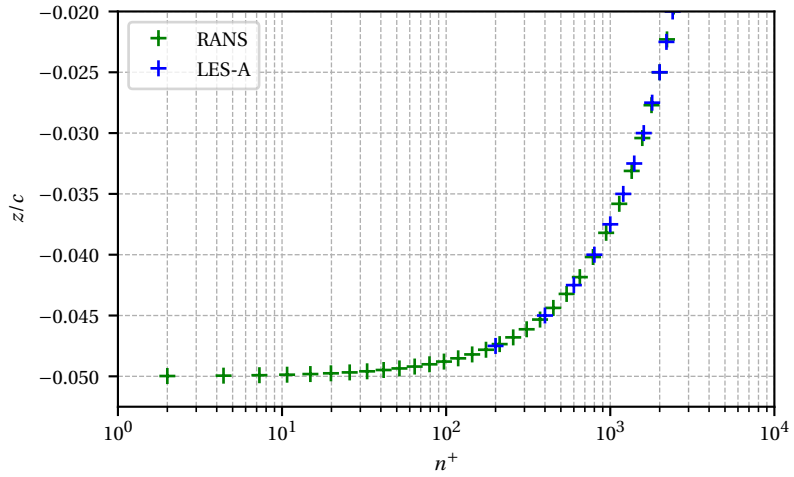

Figure 3.11: Mesh point distribution across the gap, near the lower plate at x/c = -0.60 and y/c = 0.23 for the RANS and LES-A.

3.2.5 Convergence and computational cost

RANS

Several quantities are monitored in time to check the convergence of the steady simulation. Figure 3.12a shows the residuals of the continuum, momentum, energy and turbulent equations for the RANS. All residuals have decreased by more than three orders of magnitude and reached a plateau after around 20 000 iterations. Figure 3.12b presents the sum of the massflow rates at the inlets and outlets of the computational domain. The sum stabilizes after 10 000 iterations and the discrepancy between inlet and outlet massflow rates is lower than 0.1%. Finally, the ratio between the RANS and experimental massflow rates at the nozzle exit is monitored in time as shown in Figure 3.12c. The RANS massflow rate reaches the experimental targeted value and remains constant after 5 000 iterations. The convergence of the RANS simulation is then confirmed. A total of 288 processors during 9 hours were used on CERFACS' internal Kraken cluster.

LES-A and LES-N&A

For unsteady simulations, a characteristic time is introduced to study numerical convergence. In the previous numerical studies of the single airfoil configuration, the characteristic velocity is defined as the velocity at the exit nozzle V_0 and the characteristic length as the airfoil chord c. The characteristic time named as convective time is $\tau_{conv} = c/V_0$. It corresponds to the time for a turbulent structure to flow along the airfoil convected by the mean flow. For the considered operating point, τ_{conv} = 2.86 ms. The simulation time is now expressed in terms of convective time.

As for the RANS, the sum of the massflow rates at the inlets and outlet and the massflow rate at the nozzle exit are monitored and plotted in Figure 3.13. The convergence is shown

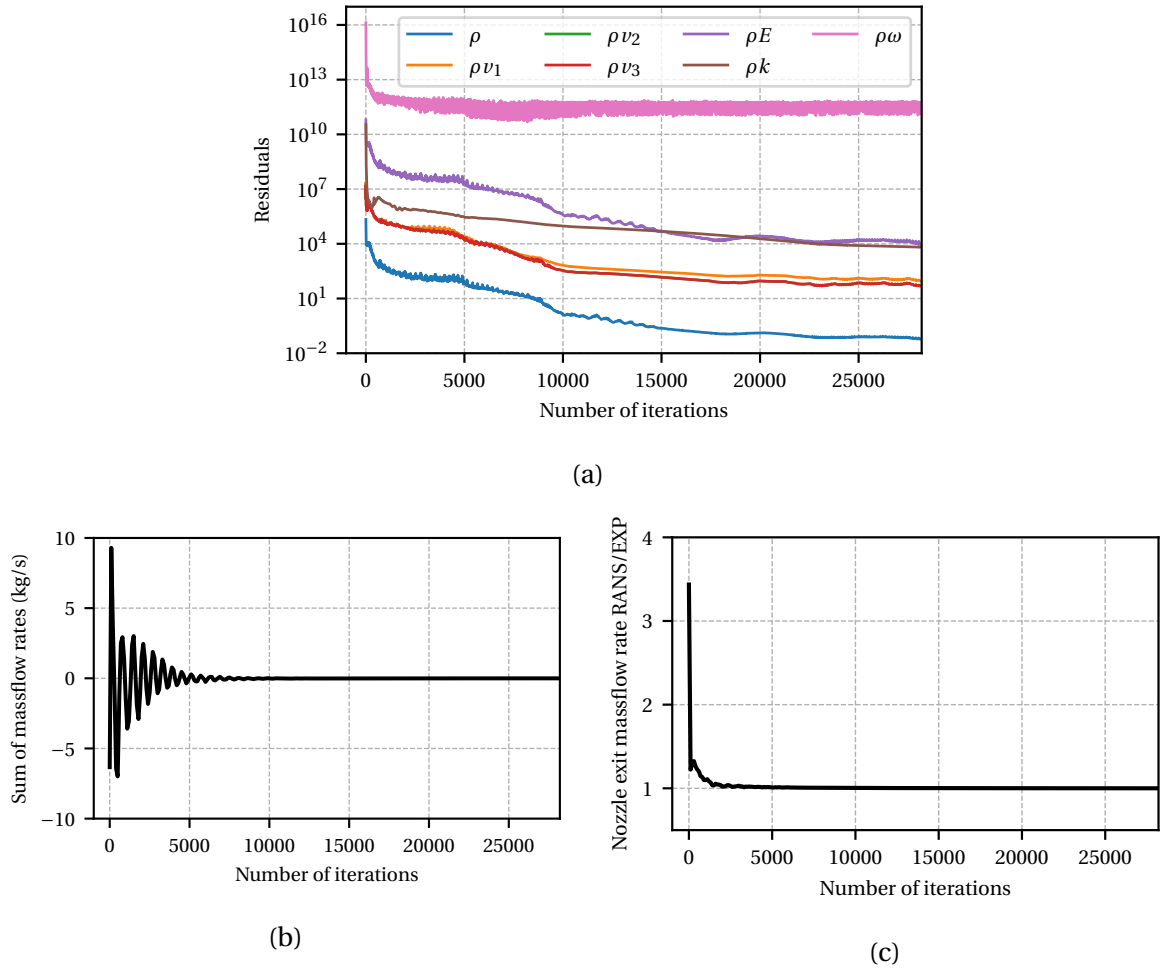

(a)

(b)

(c)

Figure 3.12: Convergence monitoring for the RANS: (a) Residuals of the continuum, momentum, energy and turbulent equations. The y-axis is in logarithm scale. (b) Sum of the massflow rates at the inlets and outlets of the computational domain. (c) Ratio between the RANS and experimental massflow rates at the nozzle exit.

here for the LES-N&A only but a similar behaviour is observed for the LES-A. $35\tau_{conv}$ are required to reach the targeted massflow rate at the nozzle exit. This large value is explained by the development of the jet. Indeed, regarding the size of the computational domain, a particle injected at the inlet requires $12.5\tau_{conv}$ to reach the outlet of the domain. The transient period corresponds actually to 2.8 characteristic times based on the domain length. After $35\tau_{conv}$, the mean massflow rate at the nozzle exit remains constant and the statistics for the LES-N&A are acquired until $49\tau_{conv}$. It results into a period of $14\tau_{conv}$ to compute the flow statistics.

In addition to the integrated quantities, local quantities are monitored. Indeed, the convergence time could be higher in some local part of the flow compared to the time required to converge the integrated quantities. Figure 3.14 presents the convergence in time of the mean static pressure P_{sta} and mean streamwise velocity V_x at several locations in the flow. The mean value is progressively updated in time, *i.e.* a time average is computed with the

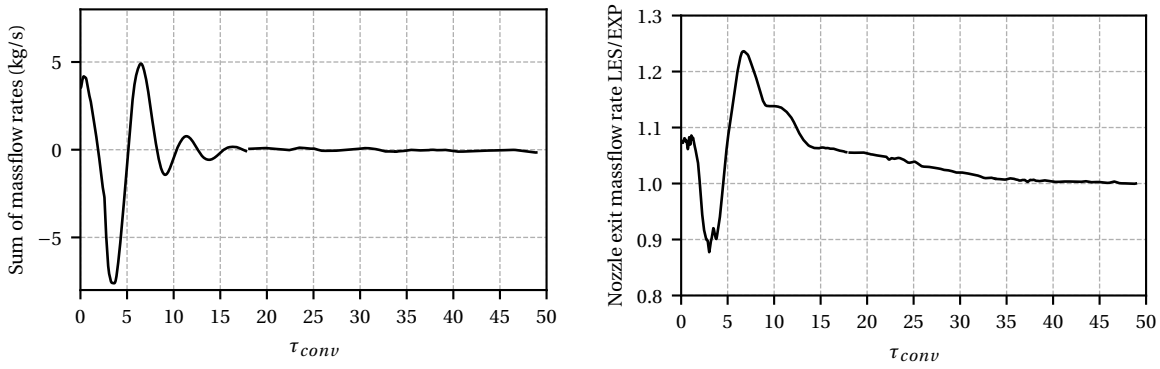

(a) (b)

Figure 3.13: (a) Sum of the massflow rates at the inlets and outlet of the computational domain for the LES-N&A. (b) Ratio between the LES and experimental massflow rates at the nozzle exit.

new instantaneous value and the former ones. The latter is normalised by the last value which corresponds to the mean value over the whole period. Three locations of interest are monitored: the incoming flow, the TLF and the TLV. Time signals are plotted over the considered period for statistics computation (35 to $49\tau_{conv}$) and rendered dimensionless by the mean value of the raw signal. All the probe signals stay around their mean value. The variations of mean static pressure and streamwise velocity are below 0.5 and 2%, respectively. Then, the global and local convergence of the flow is shown.

The time step is fixed at $3.5 \times 10^{-5}\, t_{\text{conv}}$ corresponding to a CFL number of 0.82. A total of 400 000 iterations on 4096 processors during 96 hours were required to acquire the statistics over $14\, t_{conv}$. It corresponds to a frequency range from 25 Hz to 50 kHz. Time and frequency resolutions are summed up in Table 3.4. The calculations were performed on the Joliot–Curie supercomputer in CEA's Very Large Computing Centre (TGCC).

Case	LES-A, LES-N&A, LES-N&A-ADP
Time step	$3.5 \times 10^{-5}\, t_{\text{conv}} = 1.0 \times 10^{-7}$ s
Averaging time	$3.5 \times 10^{-3}\, t_{\text{conv}} = 1.0 \times 10^{-5}$ s
Total time	$14\, t_{conv} = 40$ ms
Minimal frequency	25 Hz
Maximal frequency	50 kHz

Table 3.4: Time and frequency resolutions for the LES-A, LES-N&A, LES-N&A-ADP cases.

In the following, Welch's method is used to compute a Power Spectral Density (PSD) using 10 Hanning windows with an overlap of 50%. Probe data are sampled at $3.5 \times 10^{-3}\, t_{\text{conv}}$ leading to a LES cut-off frequency of 50 kHz. Instantaneous quantities on the airfoil surfaces are less sampled in time than probe data. Dumping time interval is $8.75 \times 10^{-3}\, t_{\text{conv}}$ leading

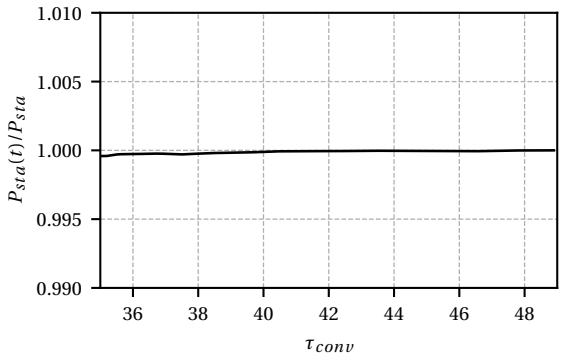

(a) Incoming flow (x/c = -3.0, y/c = 0.14, z/c = 0.45)

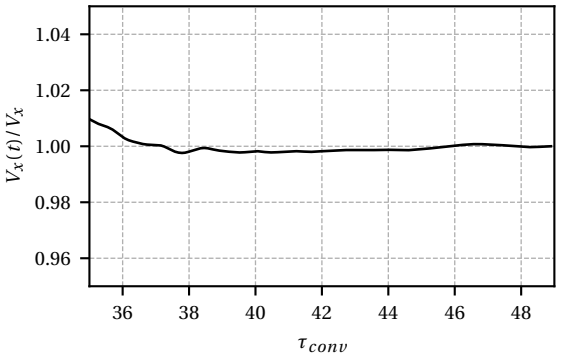

(b) Incoming flow (x/c = -3.0, y/c = 0.14, z/c = 0.45)

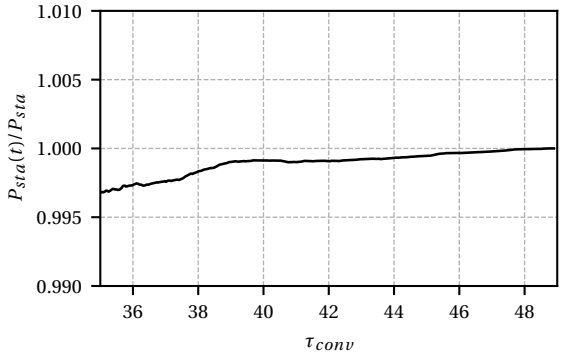

(c) TLF (x/c = -0.21, y/c = 0.097, z/c = 0.025)

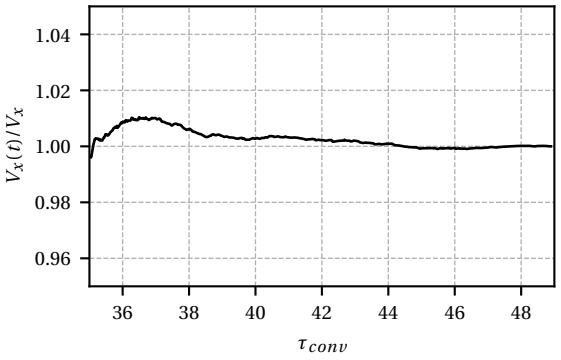

(d) TLF (x/c = -0.21, y/c = 0.097, z/c = 0.025)

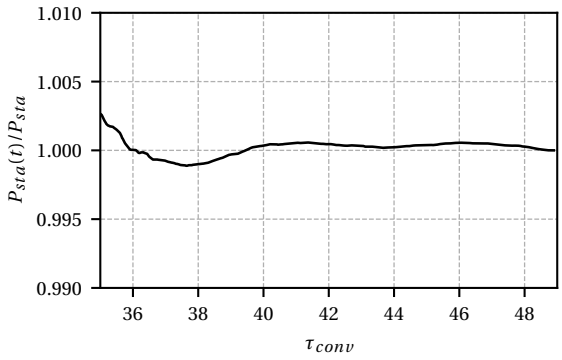

(e) TLV (x/c = 0.010, y/c = 0.15, z/c = 0.050)

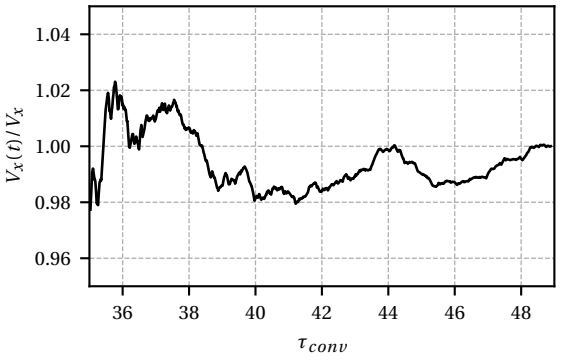

(f) TLV (x/c = 0.010 y/c = 0.15, z/c = 0.050)

Figure 3.14: Convergence in time of the mean static pressure and mean streamwise velocity on local probes.

to a cut-off frequency of 20 kHz. With a total simulation time of $14\,t_{\text{conv}}$ and the parameters set for the Welch's method, the frequency resolution is 70 Hz.

3.3 Instantaneous flow

In order to have a global view of the flow field in the area of interest, Figure 3.15 shows instantaneous iso-surfaces of Q criterion (Q = 3.0 x 10^2 $(V_0/c)^2$) coloured by the velocity magnitude

in the tip flow region for the LES-N&A. It should be underlined that as the instantaneous flow looks very similar in the LES-A, it is not shown here. The airfoil is seen from the suction side. Three vortices are identified. The tip separation vortex in the gap is generated by the separation of the TLF from the airfoil tip. The TLV developing from the airfoil leading edge is the major one. Next to it, an induced vortex is generated by the important circulation of the TLV. The last two vortices are contra-rotating to each other. The vortical structure of the tip flow identified in the literature and described in Section 1.1 is retrieved.

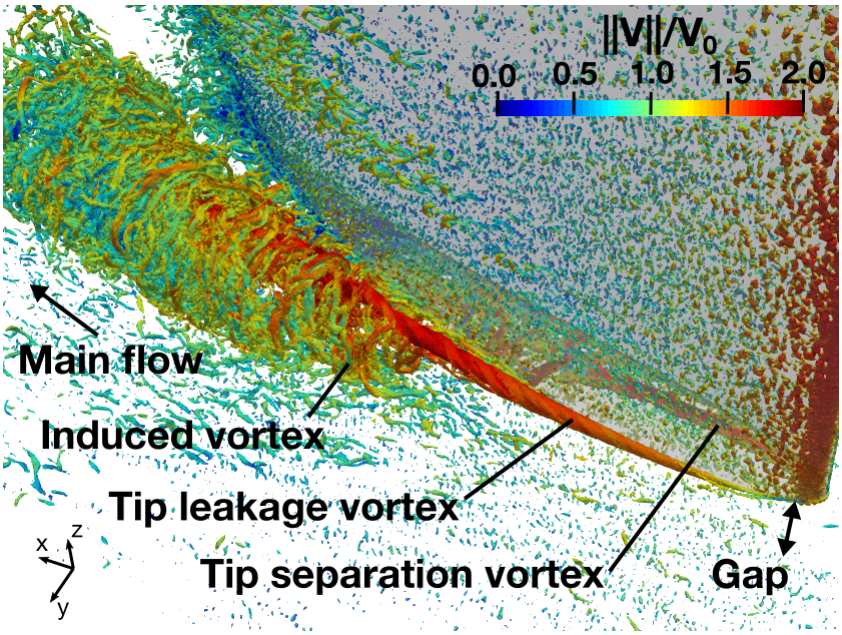

Figure 3.15: LES instantaneous iso-surfaces of Q criterion (Q = 3.0 x 10^2 $(V_0/c)^2$) coloured by the velocity magnitude in the tip flow region for the LES-N&A.

3.4 Mean flow field of the airfoil-free jet facility

To present the flow field of the airfoil-free jet facility, a plane cut of the mean velocity magnitude is presented in Figure 3.16. The velocity magnitude is normalised by the reference mean velocity V_0. The RANS case is shown in Figure 3.16a. Two mixing layers developed from the nozzle exit section are observed. When reaching the airfoil leading edge (x/c = -1), the rectangular jet is deflected by the circulation generated by the airfoil. Lobes of velocity around the airfoil interact with the mixing layers at x/c = -0.5, $y/c = \pm 1$. Moreover, a deficit of velocity magnitude is observed at y/c = 0.25, from x/c = 0. It corresponds to the print of the TLV. The airfoil wake is also identified next to the TLV. All these observations show the interaction between the airfoil and the free jet as discussed by Moreau *et al.* [64].

The flow field topologies are globally the same for the three cases in Figure 3.16. Some deviations are even observed for the mixing layers and the TLV. Whereas the RANS and LES-N&A mixing layers qualitatively exhibit similar thickening, the ones for the LES-A in Figure

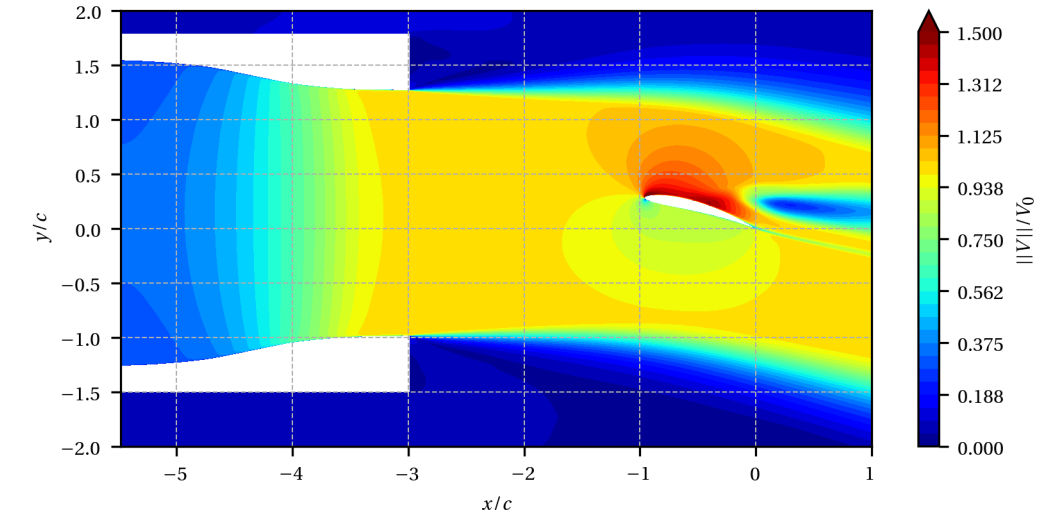

(a) RANS

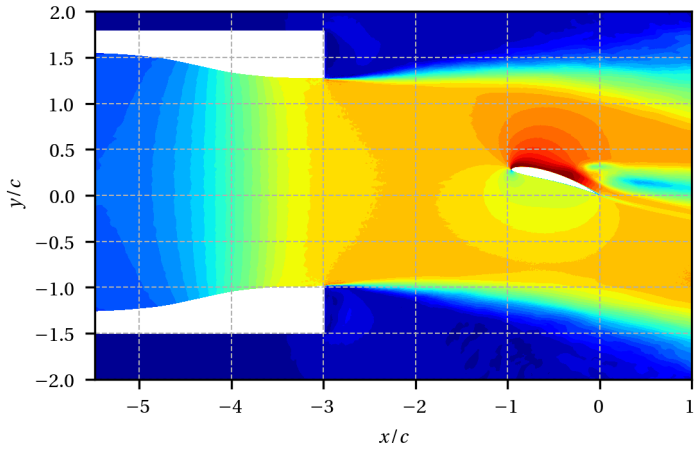

(b) LES-N&A

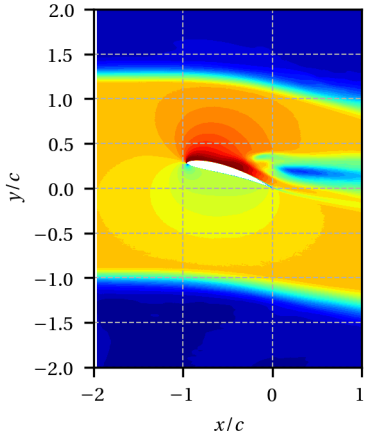

(c) LES-A

Figure 3.16: Mean velocity magnitude fields at $z/c = 0.1$.

3.16c are thinner. Including the nozzle in the computational domain has an impact on the development of the jet. Moreover, for the RANS case (Figure 3.16a), the TLV print is composed of one single area of velocity deficit ($0 < y/c < 0.5$, $x/c > 0$). Instead, for the two LES, it is rather two zones that can be distinguished with a small additional one at $x/c = 0$, $y/c = 0.3$. Besides, a deviation in the amplitude of velocity deficit is even observed between Figures 3.16b and 3.16c. The numerical approach and the inclusion of the nozzle have an impact on the TLV. A quantitative comparison of the TLVs between the cases and measurements will be achieved in Section 3.7.

3.5 Incoming flow

The aim of this section is to characterise the flow upstream of the gap. Velocity profiles obtained numerically are compared to the experimental ones measured with a hot-wire probe

set at $(x - x_{LE})/c$ = -1.5, -1.0, -0.75, -0.5 where x_{LE} is the streamwise position of the airfoil leading edge. The probe locations are aligned with the center of the nozzle exit ($y/c = 0.14$). The incoming flow is characterised in terms of mean velocity, lower plate boundary layer and turbulence intensity.

3.5.1 Mean velocity

The mean streamwise velocity is presented in Figure 3.17. The velocity is normalised by the reference mean velocity V_0. A plateau is roughly observed for the first two values at $(x - x_{LE})/c$ = -1.5 and -1.0. Then, the mean velocity decreases for the two last probes. The latter located at $(x - x_{LE})/c$ = -0.75 and -0.5 in Figure 3.17 correspond to positions x/c = -1.79 and -1.46 in Figure 3.16, where a lobe of lower velocity is found. The decrease of velocity for the two last probes is then caused by the potential effect of the airfoil. This effect has been checked to be globally reproduced in the simulations. In Figures 3.16a and 3.16b, the potential effect extends towards the convergent nozzle until x/c = -1.7. Consequently, the inlet boundary located at x/c = -2.0 for the LES-A could not have been placed further downstream.

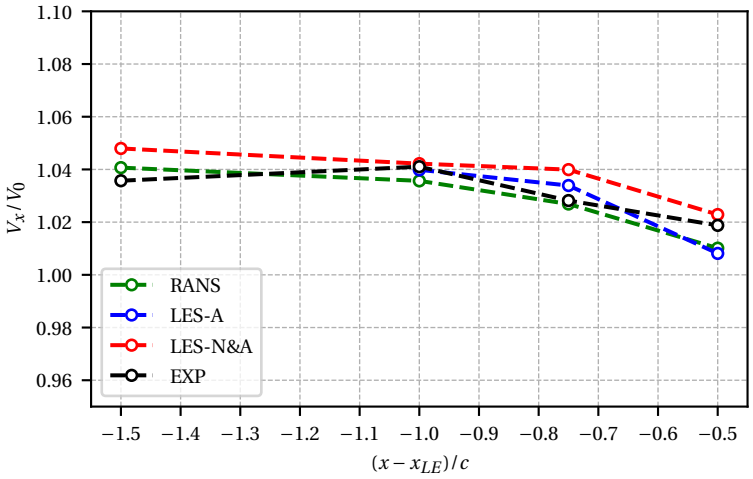

Figure 3.17: Mean streamwise velocity V_x of the incoming flow at $y/c = 0.14$.

To characterise the flow coming into the gap, the spanwise evolution of the mean streamwise velocity a half-chord upstream of the airfoil leading edge is shown in Figure 3.18. z_{LE} is the spanwise coordinate of the airfoil leading edge projected on the lower plate. Results from the ZLES of Boudet *et al.* [10] (orange) and the LES of Koch *et al.* [51] (magenta) described in Section 3.1.2 are added. Discrepancies between the velocity profiles are observed at the wall. The RANS, LES-A and Boudet *et al.* [10] exhibit equivalent profiles with a boundary layer on the lower plate thicker than the experiment. The velocity profiles of the RANS and LES-A collapse because the mean velocity from the RANS is imposed at $(x - x_{LE})/c$ = - 1.0 in the LES-A. On the contrary, the LES-N&A and Koch *et al.* [51] predict a boundary layer thinner than the experiment. Koch *et al.* [51] performed a wall-resolved LES whereas the LES-A uses

a wall-law. Therefore, discrepancies of velocity profiles at the wall are not attributed to the wall-law. A unique value of total pressure is imposed at the inlet of the nozzle for the RANS and LES-N&A meaning no boundary layer on the walls at the nozzle inlet. However, boundary layers exist in the experiment. Inflow conditions in the simulations may be improved by setting total pressure in two dimensions on the inlet surface or by including the wind tunnel upstream of the nozzle inlet in the computational domain.

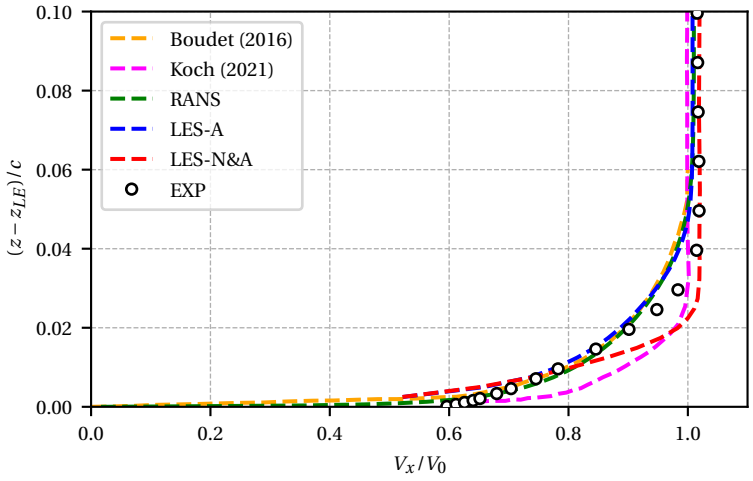

Figure 3.18: Profiles of mean streamwise velocity V_x at $(x-x_{LE})/c$ = - 0.5 and $y/c = 0.14$.

3.5.2 Lower plate boundary layer

To quantify the lower plate boundary layer, the streamwise evolution of its thickness is shown in Figure 3.19. The following definition is used to compute the boundary layer thickness δ: $V_x((z-z_{LE})=\delta) = 0.99\max(V_x)$. The gap height is represented by a dashed grey line at δ/c = $s/c = 0.05$.

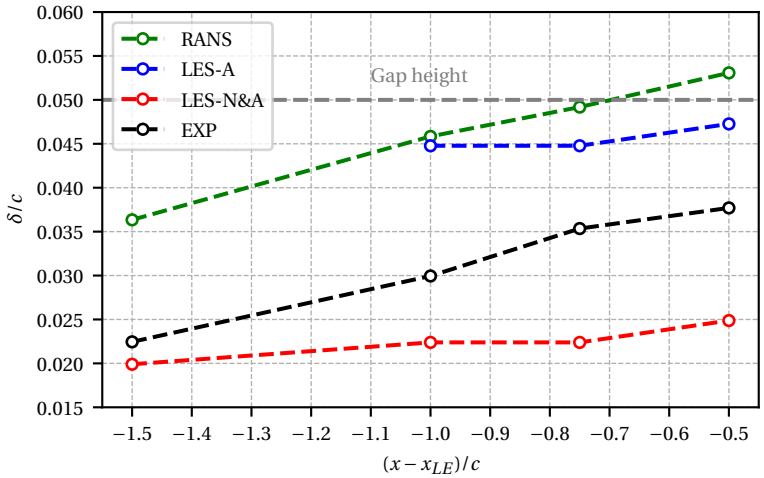

Figure 3.19: Lower plate boundary layer thickness δ of the incoming flow.

The boundary layers for the RANS and LES-A are thicker than in the experiment for all positions. At $(x - x_{LE})/c$ = -0.5, the thicknesses are in the order of the gap height. The boundary layer could then interact with the airfoil leading edge, which is not the case in the experiment. As shown in Figure 3.19 for $(x - x_{LE})/c$ = -0.5, the LES-N&A exhibits a thinner boundary than in the experiment for all positions. Besides, the thickening rate of the boundary layer defined by the gradient $\partial\delta/\partial x$ is equivalent between the RANS and the experiment. The overestimation of the thickness rate on the lower plate for the RANS is then caused by an overestimation in the nozzle. The thickening rates for the two LES are lower than the experiment. The turbulence intensity is now studied to explain the different development of the lower plate boundary layer.

3.5.3 Turbulence intensity

The turbulence intensity of the incoming flow is quantified with the fluctuating velocity component v_x^{rms}. The latter is defined as $\left(v_x^{rms}\right)^2 = \langle v_x - V_x \rangle^2$, where v_x is the instantaneous streamwise velocity and $\langle\,.\,\rangle$ the time average. For the RANS approach, the fluctuating velocity is computed from the turbulent transported variable k, $v_x^{rms} = (2/3k)^{0.5}$. For the LES approach, the time-averaged Reynolds stress tensor of the resolved part of the velocity is computed.

Figure 3.20 presents the profiles of streamwise velocity fluctuations a half-chord upstream of the airfoil leading edge. v_x^{rms}/V_0 is the streamwise turbulence intensity. In the experiment, a turbulence intensity of 1.6% was measured in the outer flow region ($(z - z_{LE})/c$ > 0.06) increasing up to 8.0% in the boundary layer.

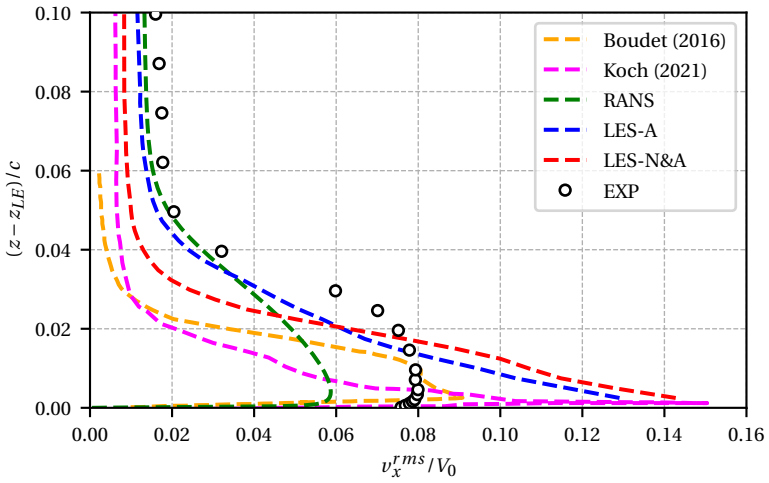

Figure 3.20: Profiles of streamwise velocity fluctuations v_x^{rms} at $(x - x_{LE})/c$ = - 0.5 and y/c = 0.14.

The RANS reproduces the shape of the experimental profile with an underestimation of the turbulence intensity in the boundary layer. The LES-A, LES-N&A and Koch *et al.* [51]

exhibit globally the same shape with a sharp peak at the wall. These differences with the experiment are explained by the history of the boundary layer. Indeed, the boundary layer comes from a wind tunnel in the experiment whereas it is not the case in the LES. Injecting synthetic homogeneous isotropic turbulence in the LES-A only improves the turbulence intensity in the outer flow region when compared to the LES-N&A.

Boudet *et al.* [10] obtained the better agreement with the experimental profile of streamwise velocity fluctuations in their LES. A peak is also observed in the boundary layer but with a lower intensity (9%). This result was obtained by inducing the transition of the boundary layer to the turbulent state using a source term that mimics a surface tripping. In the outer flow, the ZLES from Boudet *et al.* [10] strongly underestimated the turbulence intensity with a relative deviation of 87% from the experiment.

3.6 Airfoil loading

The static pressure distribution on the airfoil surface characterising the airfoil loading is now analysed. The pressure coefficient C_p is introduced

$$C_p = \frac{P_{sta} - P_0}{0.5\rho_0 V_0^2}. \tag{3.7}$$

Figures 3.21 and 3.22 present respectively the mean pressure coefficients on the airfoil at midspan ($z/c = 0.45$) and at tip ($z/c = 0.005$). The lower part of the curves is the pressure side and the upper part the suction side of the airfoil. c_x is the axial chord length.

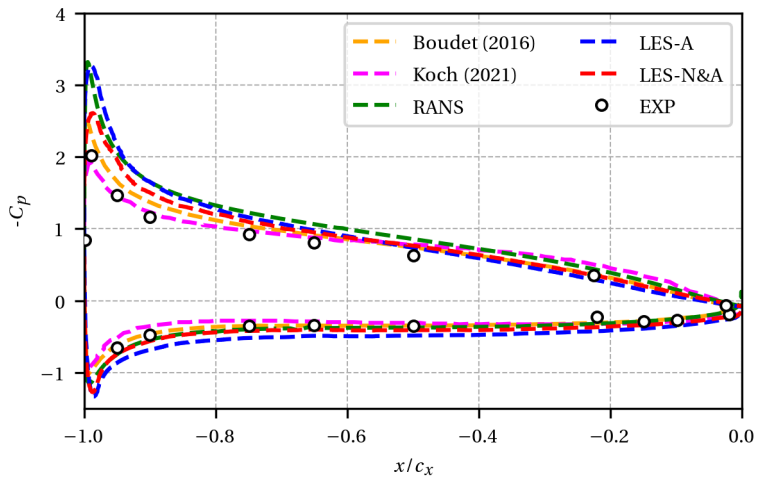

Figure 3.21: Mean pressure coefficients C_p on the airfoil at midspan $z/c = 0.45$.

At midspan (Figure 3.21), the RANS, LES-A and LES-N&A match the experimental pressure coefficients as well as the simulations from Boudet *et al.* [10] and Koch *et al.* [51] for the majority of the airfoil surface promoting that the numerical simulations retrieve the operating point experimentally tested. The LES-A and LES-N&A are performed with a wall-law

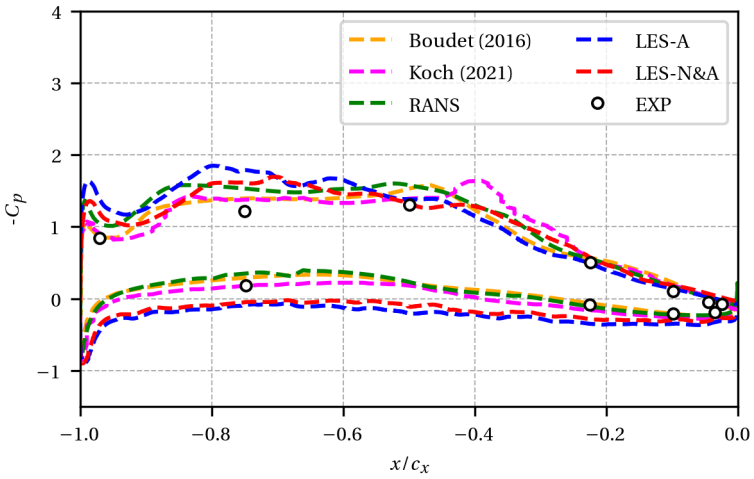

Figure 3.22: Mean pressure coefficients C_p on the airfoil at tip $z/c = 0.005$.

whereas the simulations from Boudet *et al.* [10] and Koch *et al.* [51] are wall-resolved. These results also indicate the good behaviour of the wall-law around the airfoil at midspan.

Besides, slight deviations observed on the suction side, close to the leading edge for x/c_x < -0.8 may be explained by the angle of attack. Indeed, the RANS, LES-A and LES-N&A are performed at 16.5° whereas Boudet *et al.* [10] and Koch *et al.* [51] are at 15.0° as indicated in Table 3.2. It was shown by Grilliat in his thesis [34] that the angle of attack has an influence on the pressure coefficients especially at the leading edge. Moreover, the jet development which is not characterised in the experiment and the simulations could modify the flow around the airfoil, thus the static pressure on the airfoil.

At tip (Figure 3.22), the measured airfoil loading is globally reduced compared to the one at midspan. The TLF from the pressure side to the suction side partially balances the pressure difference at tip. As a reminder, the airfoil tip loading is one of the main parameters which control the TLF (Section 1.1). Again, the RANS, LES-A and LES-N&A are able to properly predict the pressure distribution at tip. The capacity of the wall-law at tip is shown.

3.7 Tip leakage vortex

The capacity of the simulations to reproduce the aerodynamics of the TLV is studied in this section. The streamwise V_x, cross-stream V_y and spanwise V_z mean velocity components of the TLV at the airfoil trailing edge are shown in Figures 3.23, 3.24 and 3.25, respectively. The numerical results are compared with 3D PIV performed by Jacob *et al.* [46]. The TLV is roughly aligned with the $\boldsymbol{x}$ axis, the plane is then almost perpendicular to the trajectory of the TLV. The flow is viewed from down- to upstream. The velocity components are normalised by the reference mean velocity V_0. The airfoil trailing edge is plotted in black solid line at $y/c = 0$. The white rectangle ($0.0 < y/c < 0.1$) in Figures 3.24a and 3.25a defines the airfoil projected surface as seen from the camera but it has no physical meaning since the signal in

this region is disrupted by light reflections [46].

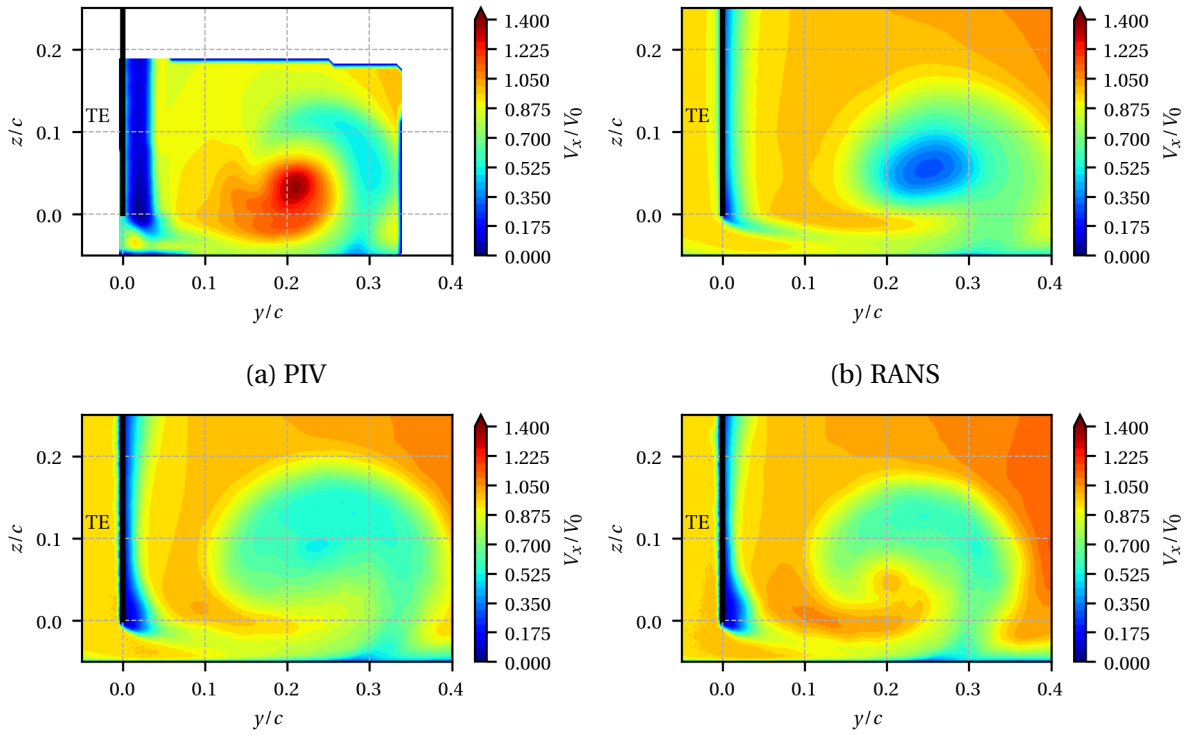

(a) PIV

(b) RANS

(c) LES-A

(d) LES-N&A

Figure 3.23: Streamwise mean velocity component V_x of the TLV at the airfoil trailing edge ($x/c = 0.01$).

When looking at the mean axial velocity component V_x of the TLV from the PIV data (Figure 3.23a), two distinct regions are identified. First, a strong acceleration region with a maximum of $1.4V_0$ is measured at $y/c = 0.22$ and $z/c = 0.04$. This position corresponds to the center of the TLV. Secondly, a low velocity region surrounding the zone of acceleration extends from the plate until $z/c = 0.15$. It is generated by the detachment of the plate boundary layer by the TLF.

The RANS case in Figure 3.23b exhibits a different topology with only one low velocity region. The spatial extension of this region in the RANS velocity field corresponds roughly to the sum of the two regions on the PIV field (Figure 3.23a). The minimum of V_x on the RANS result is equal to $0.3V_0$. This may be explained by the accuracy of the convection scheme and the RANS model. Indeed, a second order scheme is used for the RANS whereas strong velocity gradients are found in the TLV. Moreover, the k-ω Wilcox model is much more suited to wall-bounded flow than to free shear flow.

The LES-A in Figure 3.23c also predicts one low velocity region but with a minimum of V_x of $0.5V_0$. A flow topology with two regions is only captured by the LES-N&A in Figure 3.23d. Nevertheless, the magnitude of the acceleration is lower than the measured one. Adding the convergent nozzle allows to improve the prediction of the convection of the TLV. The streamwise velocity component at the center of the TLV is even underestimated by 21% compared

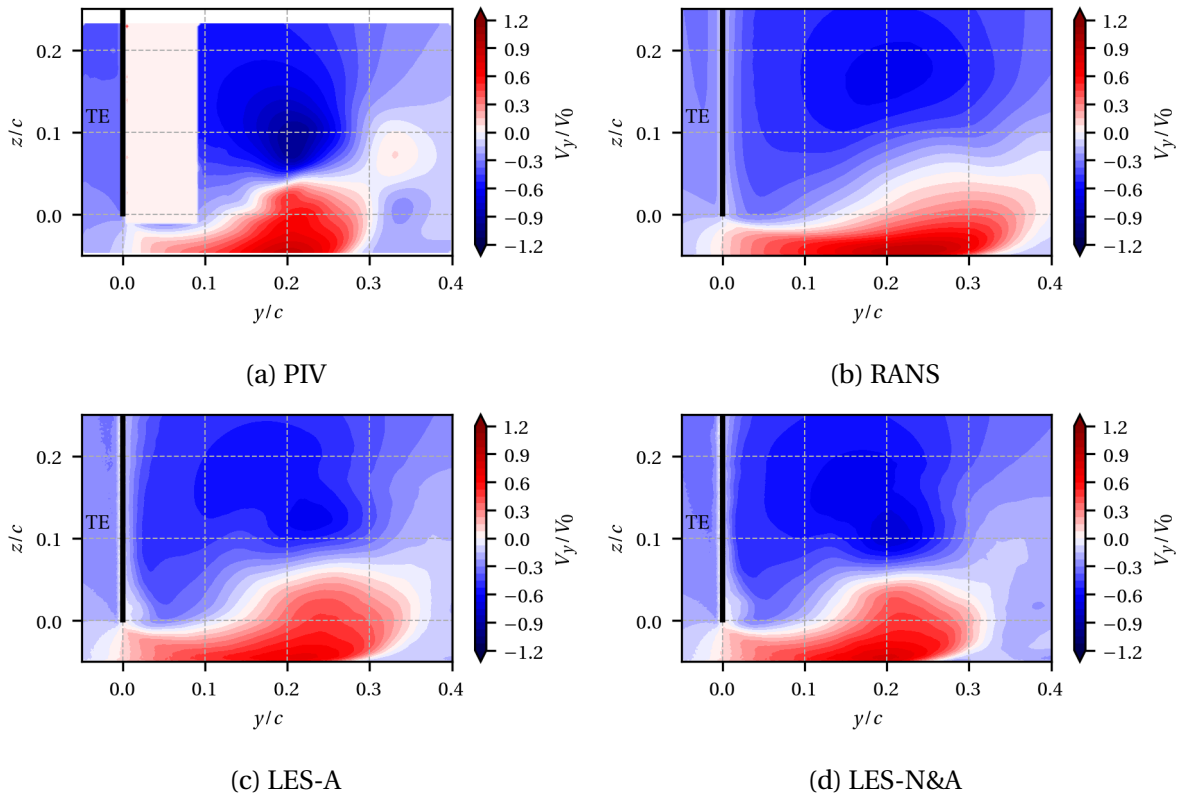

(a) PIV

(b) RANS

(c) LES-A

(d) LES-N&A

Figure 3.24: Cross-stream mean velocity component V_y of the TLV at the airfoil trailing edge ($x/c = 0.01$).

with experiment. This underprediction is attributed to the mesh resolution and will be discussed in Section 3.7.2.

Looking at the PIV measurements in Figures 3.24a and 3.25a, a region of positive V_y is observed for $z/c < 0.05$ whereas a region of negative V_y is shown for $z/c > 0.05$. For the spanwise mean component V_z, two regions are also identified: positive V_z for $y/c > 0.2$ and negative V_z for $y/c < 0.2$. This clearly shows the roll up of the TLV. The same kind of flow topology can be noticed around $y/c = 0.35$ but with a smaller spatial extension and opposite sign compared to the TLV. This flow topology indicates an induced vortex as observed on iso-surfaces of Q criterion in Figure 3.15. In addition, for the cross-stream component V_y, the extension of the region in red in the gap ($z/c < 0$) brings out the TLF that feeds the TLV.

The RANS simulation, in Figures 3.24b and 3.25b, correctly reproduces the topology at the airfoil trailing edge but diffusion is noted. Indeed, a lower velocity magnitude is observed and the TLV is much more spatially spread out compared to the PIV measurements. This is even more pronounced for the spanwise component V_z.

The LES-A, in Figures 3.24c and 3.25c, correctly reproduces the topology of the TLF region with less diffusion than the RANS. The LES-N&A in Figures 3.24d and 3.25d also reproduces the topology of the TLV with the same level of diffusion but an improvement on the position of the vortex is observed. Indeed, on the PIV data (Figure 3.25a), the y position of the TLV which is identified by the sudden change of sign on V_z, is $y/c = 0.2$. Whereas the LES-A

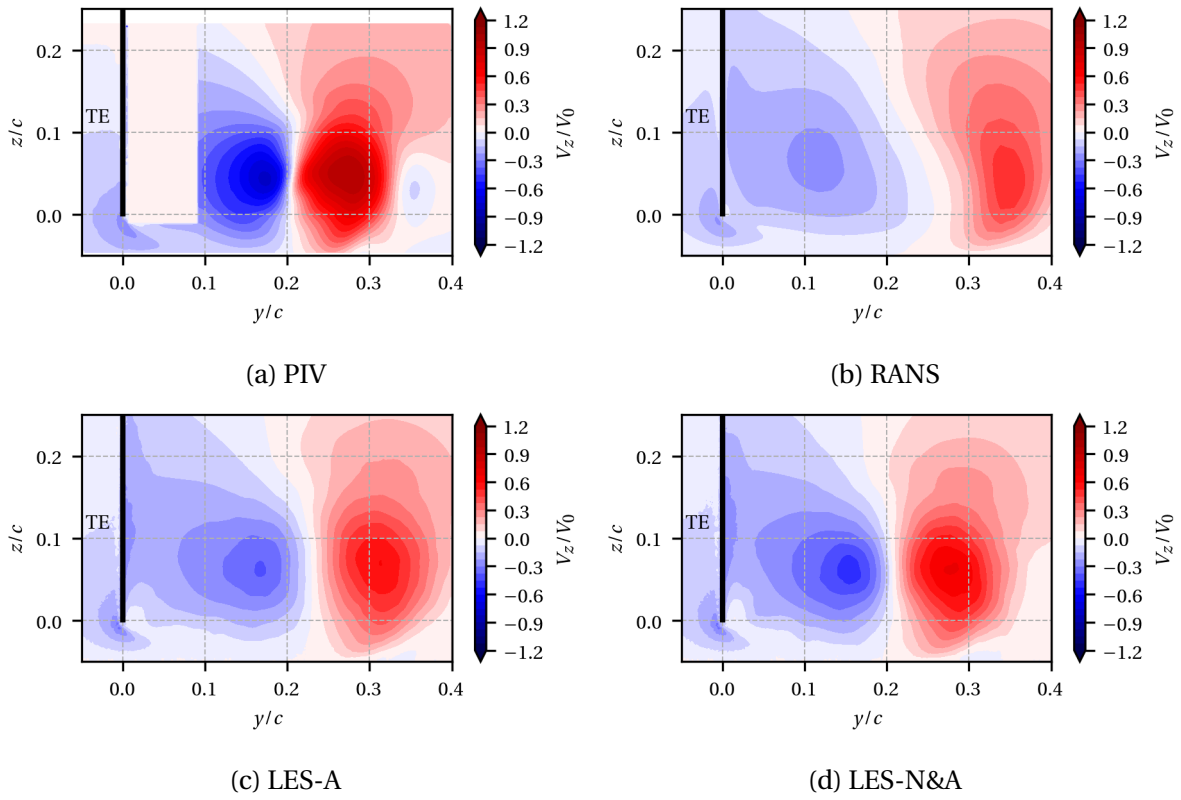

(a) PIV

(b) RANS

(c) LES-A

(d) LES-N&A

Figure 3.25: Streamwise mean velocity component V_z of the TLV at the airfoil trailing edge (x/c = 0.01).

predicts the vortex at y/c = 0.23, adding the nozzle allows to obtain the correct cross-stream position of the vortex. A slight improvement is also observed on the spanwise position between Figures 3.24c and 3.24d.

3.7.1 Mean trajectory

Using the vortex identification functions presented in Section 2.5, TLV centres are identified on yz planes at different spatial positions in the streamwise direction (x/c = -0.5, -0.4, -0.3, -0.2, -0.1, 0.01, 0.1, 0.2, 0.3). Following this process, the mean trajectory of the TLV in space can be obtained. Figure 3.26 displays the trajectory projected on planes xy (Figure 3.26a) and xz (Figure 3.26b) for the RANS, LES-A, LES-N&A and measurements. The experimental data are limited to the three PIV planes at x/c = -0.2, -0.1, 0.01. The airfoil is in grey shapes. The results from Boudet *et al.* [10] and Koch *et al.* [51], only available on plane xy, are also added. Boudet *et al.* [10] also obtained the trajectory using the vortex identification function Γ_1. Koch *et al.* [51] extracted the vortex centres as the point of maximum axial vorticity explaining the continuous line in Figure 3.26a.

All the simulations exhibit the same global trajectory of the TLV. The rough alignment of the vortex with the $\boldsymbol{x}$ axis stated in Section 3.7 is confirmed. During the TLV evolution, its center is moving away from both the blade suction surface and the endwall approximately

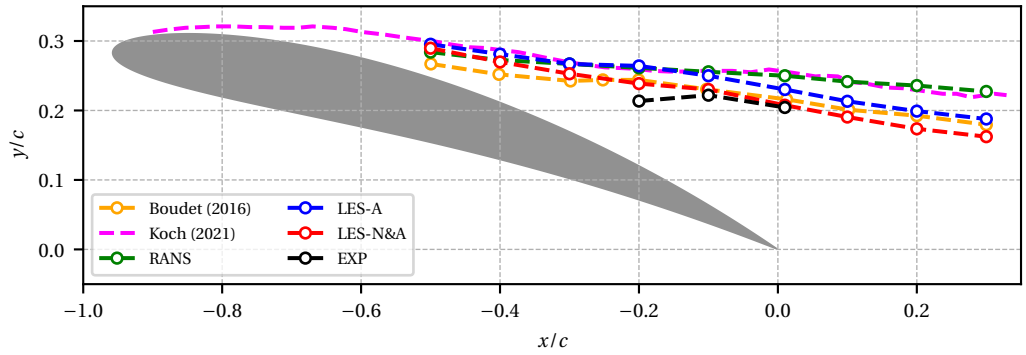

(a) Plane xy

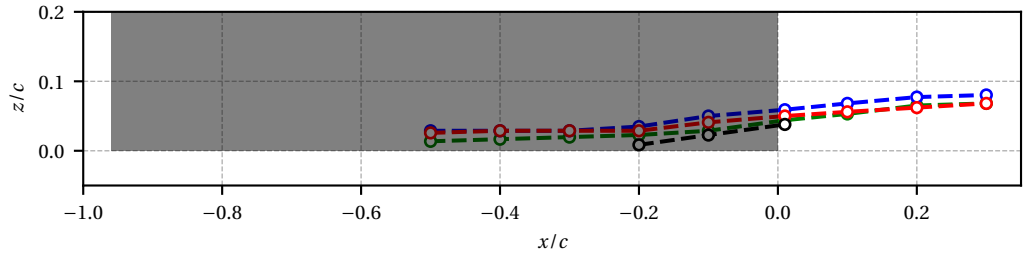

(b) Plane xz

Figure 3.26: Projected mean trajectory of the TLV.

linearly with the distance travelled by the TLV. It confirms the observations from Kang and Hirsch [49] detailed in Section 1.1.2. In Figure 3.26b, the vortex stays close to the airfoil tip with all the centres are located below $z/c = 0.1$. In other words, the influence of the TLV is limited to approximately 10% of the airfoil span.

Nevertheless, some discrepancies are observed between the simulations on Figure 3.26a. The better agreement with the experiment is obtained by the LES-N&A and Boudet *et al.* [10]. The deviations may be explained by the jet development. For instance, for the LES-N&A, the mixing layers are thicker than the ones for the LES-A (Figure 3.16). It results into a contraction of the flow around the airfoil, reducing the distance between the TLV and the airfoil suction side. For the prediction of the TLV trajectory, a particular attention has to be paid to the flow convecting the vortex. In the case of the airfoil-free jet facility, it is mainly influenced by the prediction of the jet. The inclusion of the nozzle in the computational domain exhibits the best results. Moreover, in Figure 3.26b, the TLV is further away from the lower plate for the LES-A than the LES-N&A. It explains the difference in the velocity deficit on Figure 3.16.

Finally, as explained by Storer *et al.* [89], the tip vortices have an influence on the pressure distribution on the airfoil surface. The modification of the trajectory of the TLV observed in Figure 3.26a explains the difference on the pressure coefficient on the suction side at tip for -0.5 < x/c_x < -0.2 in Figure 3.27. For the LES-N&A, the TLV is closer to the airfoil, then the pressure coefficient is lower compared to the LES-A.

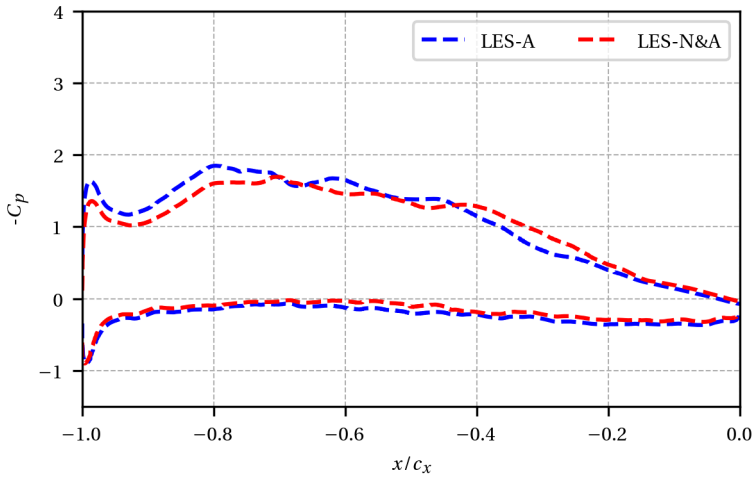

Figure 3.27: Mean pressure coefficients C_p on the airfoil at tip $z/c = 0.005$ for the LES-A and the LES-N&A.

3.7.2 Mean convection

The convection of the TLV is characterised with the streamwise velocity component V_x. In Figure 3.23, the simulations were not able to recover the acceleration measured by the PIV. To improve the prediction of the LES, a mesh adaptation based on the dissipation of the mean flow kinetic energy presented in Section 2.3 is performed.

The mesh adaptation procedure described in Section 2.3 is applied. The metric is only computed from the time-average kinetic energy dissipation rate. Using the *pyhip* tool [36], 38×10^6 tetrahedrons are added to the initial mesh (LES-N&A) and the minimal edge size is divided by a factor of 1.12. The magnification factor is set to $\alpha = 100$ and the minimum of the metric field to $\epsilon = 0.7$. The spatial extension of the adaptation is limited to $z/c < 0.5$ spanwise and to $x/c < 1.25$ streamwise. A particular attention has been paid to refine the mesh on large areas with smooth transition to not constrain the flow physics.

The adapted mesh at $z/c = 0.01$ is shown in Figure 3.28a. The mesh has been refined in the zones of interest, *i.e.* the TLV, the wake and around the airfoil surface. For the same simulated time, the computational cost is increased by 25%. The edge size of the mesh before and after adaptation at the airfoil trailing edge is presented in Figures 3.28b and 3.28c, respectively. This new case is labelled as LES-N&A-ADP.

Figure 3.23 compares the mean axial velocity V_x between the PIV, LES-N&A and LES-N&A-ADP of the TLV at the airfoil trailing edge. With the proper mesh refinement, the LES-N&A-ADP is able to better recover the topology measured by the PIV. Indeed, the two velocity regions and even the position of the maximum of V_x are captured with less than 15% of error compared to the PIV.

In order to have a closer look to the flow in this region, 1D velocity profiles are plotted at $z/c = 0.05$ in Figure 3.30. Using the mesh adaptation, the predicted velocity profile is clearly improved. Indeed, whereas the deficit of velocity caused by the airfoil wake around

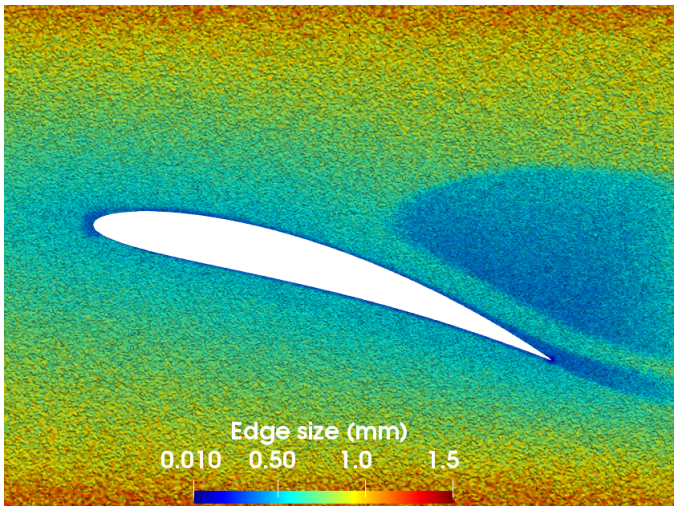

(a) Adapted mesh at $z/c = 0.1$.

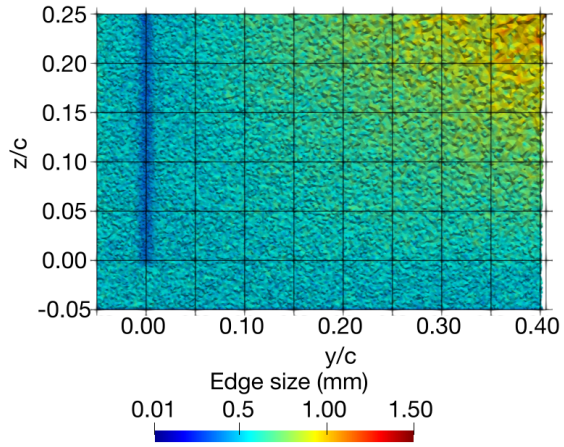

(b) Initial mesh at $x/c = 0.01$.

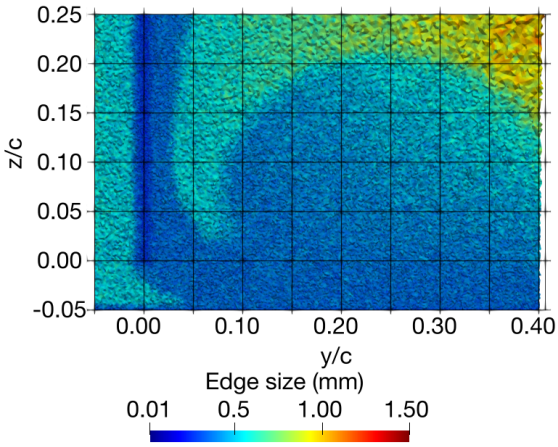

(c) Adapted mesh at $x/c = 0.01$.

Figure 3.28: Mesh cuts before and after adaptation.

$y/c = 0$ is retrieved by both simulations with the correct amplitude, some discrepancies are observed in the TLV area from $y/c = 0.17$ to 0.35. Indeed, the LES-N&A-ADP in brown is able to recover the amplitude of the maximum V_x at $y/c = 0.2$. Mesh adaptation allows to recover the complex structure of the TLV and especially the acceleration of the streamwise velocity component.

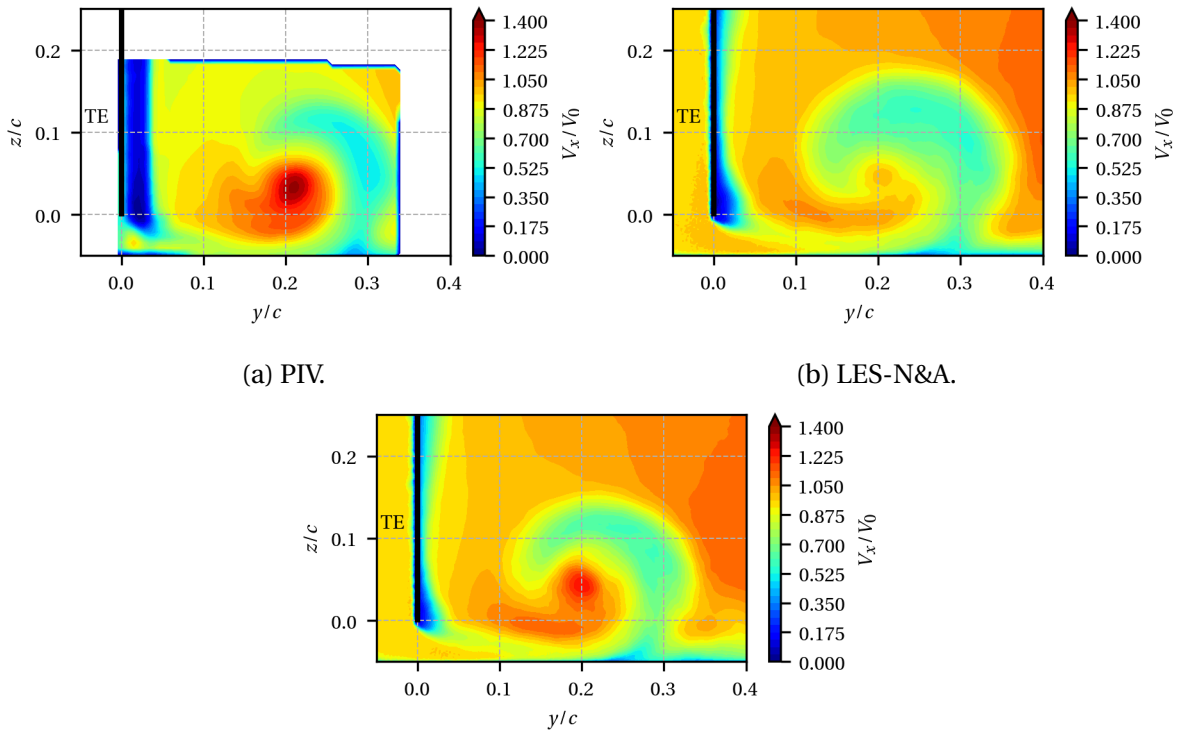

(a) PIV.

(b) LES-N&A.

(c) LES-N&A-ADP.

Figure 3.29: Streamwise mean velocity component V_x of the TLV at the airfoil trailing edge ($x/c = 0.01$).

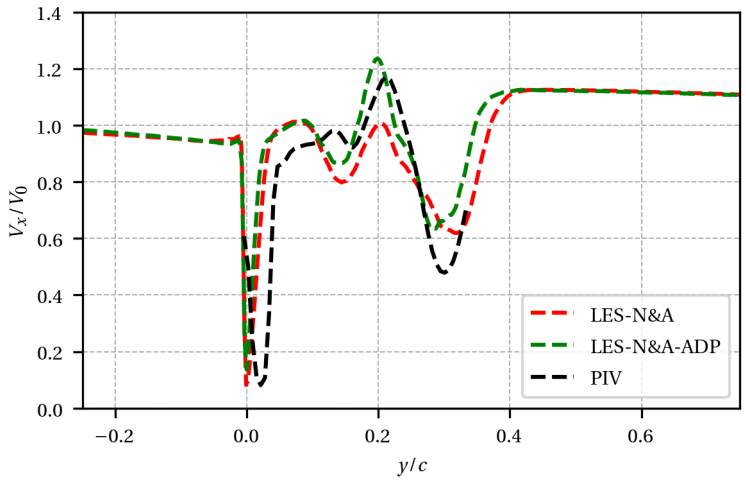

Figure 3.30: Profiles of mean streamwise velocity V_x at $x/c = 0.01$ and $z/c = 0.05$.

3.7.3 Turbulent activity

The velocity fluctuations of the TLV at the airfoil trailing edge are analysed in order to quantify its turbulent activity. The same plane as for the mean velocity components is considered. Figure 3.31 presents the turbulent kinetic energy from the experiment and the simulations. It is normalised by a reference kinetic energy defined as $k_0 = 0.5V_0^2$.

From the PIV measurements in Figure 3.31a, the maximum of normalised turbulent ki-

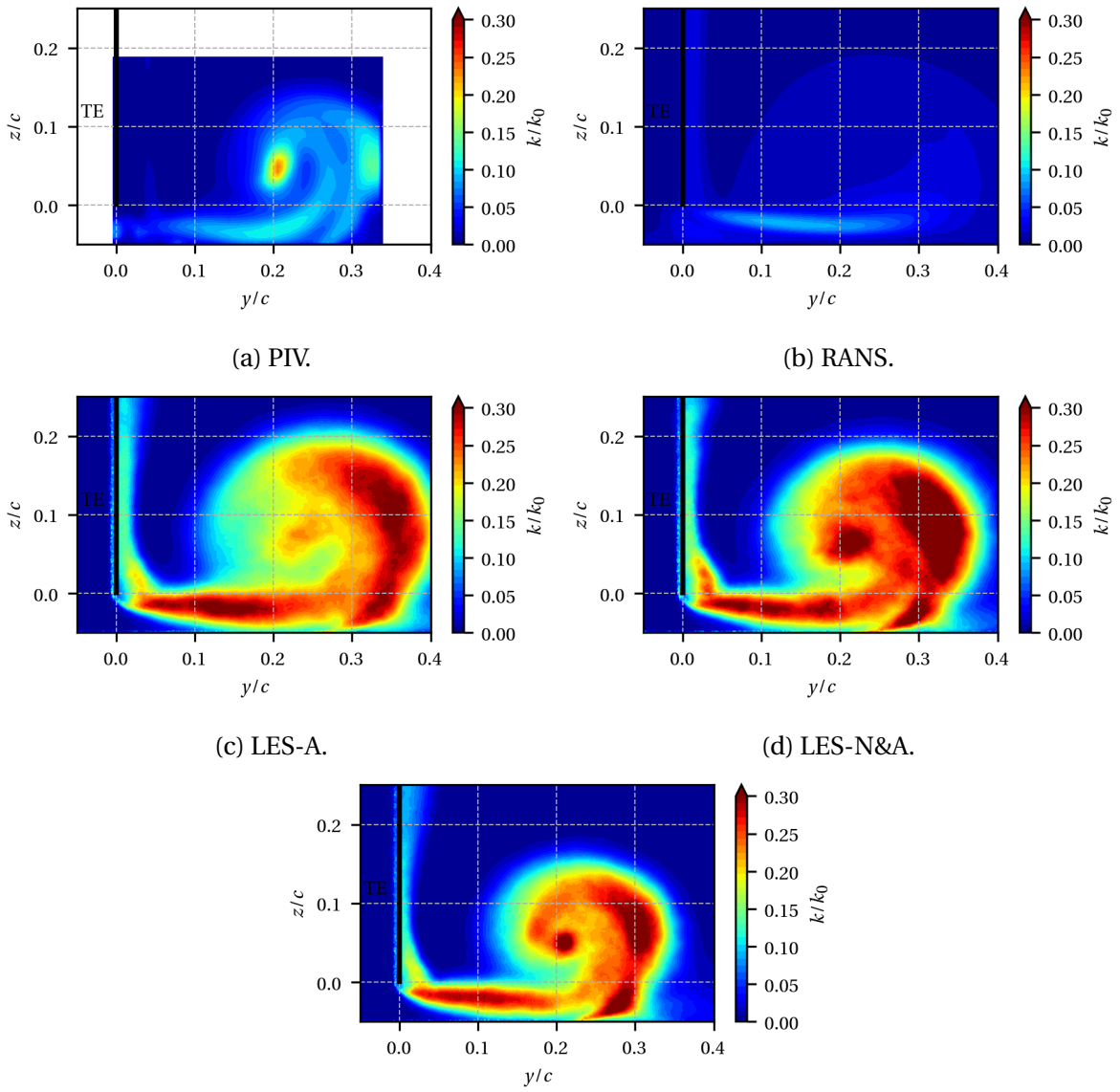

(a) PIV.

(b) RANS.

(c) LES-A.

(d) LES-N&A.

(e) LES-N&A-ADP.

Figure 3.31: Turbulent kinetic energy k of the TLV at the airfoil trailing edge ($x/c = 0.01$).

netic energy is reached at the TLV center with a value of $0.24k_0$. The important rotation of the flow at this location induces large velocity fluctuations. Then, two curved regions with k levels between 0.10 and 0.15 are identified. The first one starting from the lower plate around $y/c = 0.3$ corresponds to the edge of the TLV. The shear layer at the interface between the vortex and the main flow leads to a significant turbulent kinetic energy production. The second curved region with high levels of turbulent kinetic energy is placed at $z/c < 0$. It extends towards the gap along the lower plate. This trace corresponds to the interface between the two regions observed in Figure 3.23a. The strong gradients of V_x in the spanwise direction generates velocity fluctuations.

The RANS only predicts the second curved region generated by the shear stress of the TLF. Levels of k are underestimated with a maximum value around $0.10k_0$. For the LES-A

(Figure 3.31c), the topology of k previously described is correctly modelled. However, the amplitude is highly overestimated. It is even larger for the LES-N&A in Figure 3.31d. The difference between the LES-A and LES-N&A is explained by the modification of the TLV trajectory quantified in Figure 3.26. The position of the two dimensional field relative to the TLV has changed between the two LES. In a reference frame relative to the vortex, the flowfield is a slightly further upstream in the LES-N&A case. Turbulence is dissipated between the two positions relative to the vortex. Adding the convergent nozzle has an impact on the mean trajectory of the TLV but not on its turbulent activity.

The mesh adaptation in the TLV achieved for the LES-N&A-ADP in Figure 3.31e improves the LES prediction. Indeed, the magnitude of turbulent kinetic energy is lower than the LES-N&A. Even if the magnitude of k is still higher than the PIV field, the topology is close to the experiment. The overestimation may be attributed to the large resolved turbulent structures that carry too much energy. The modelling of the small structures in the LES approach explained in Figure 2.1 may be misrepresented having an impact on the energy transfer from large to small structures. A mesh refinement or other subgrid-scale model may improve the prediction of the turbulent kinetic energy in the TLV.

The turbulence isotropy of the TLV is now analysed by looking at the fluctuating velocity components for the PIV and the LES cases. Figure 3.32 presents the spanwise fluctuating velocity component v_z^{rms} of the TLV at the airfoil trailing edge. Areas with important magnitude are retrieved by the LES but overestimated in value. The same conclusion can be made for the streamwise and cross-stream fluctuating velocity components available in Appendix B. The turbulence isotropy of the TLV is predicted by the LES. The overestimation of the turbulence kinetic energy k is the result of a slight overestimation of each fluctuating velocity component ($k = 0.5[(v_x^{rms})^2 + (v_y^{rms})^2 + (v_z^{rms})^2]$).

The analysis will now focus on the spectral content of the velocity component v_z. Two positions on the PIV plane at the airfoil leading edge are considered. The LDV measurement closest to the vortex center ($y/c = 0.2$, $z/c = 0.05$) is plotted in Figure 3.33a together with the prediction from the LES cases. A second probe located in the TLF ($y/c = 0.15$, $z/c = -0.025$) is shown in Figure 3.33b. A peak at $St_0 = 0.14$ characteristic of the jet unsteadiness [34] is noted in Figure 3.33a. The peak is not observed in Figure 3.33b. The jet oscillation has an impact on the velocity fluctuations of the TLV but not on the ones of the TLF.

Only low frequencies until 4 096 Hz (St = 12) are accessible from the experiment, while the simulations essentially predict higher frequencies. However, a good match is obtained in the intermediate Strouhal number range from 3 to 12 kHz. The levels and the spectrum slope are correctly modelled by the numerical methods. For Strouhal numbers below 3, the numerical spectra are damped and diverge from the experiment. The same shape of velocity spectra was observed by Boudet *et al.* [10] for probes located in the TLV.

The almost superimposition of the spectra shows that the inclusion of the nozzle in the computational domain, the mesh adaptation and the use of a wall-law does not have an

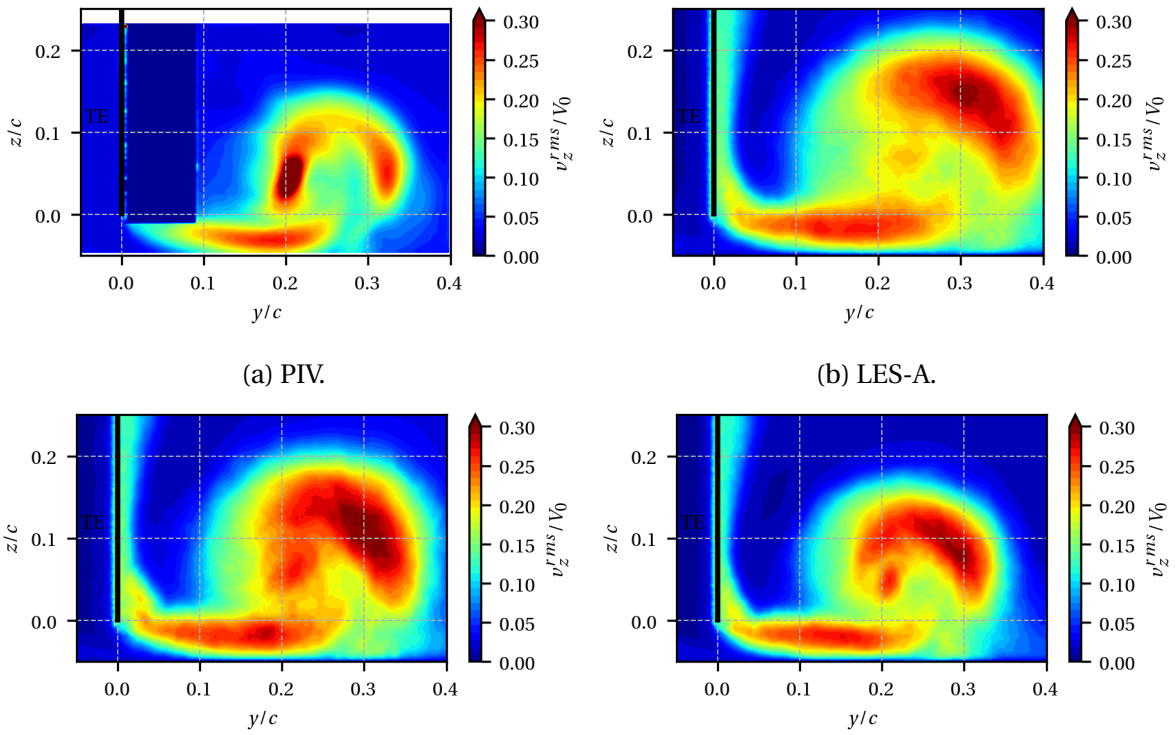

(a) PIV.

(b) LES-A.

(c) LES-N&A.

(d) LES-N&A-ADP.

Figure 3.32: Spanwise fluctuating velocity component v_z^{rms} of the TLV at the airfoil trailing edge ($x/c = 0.01$).

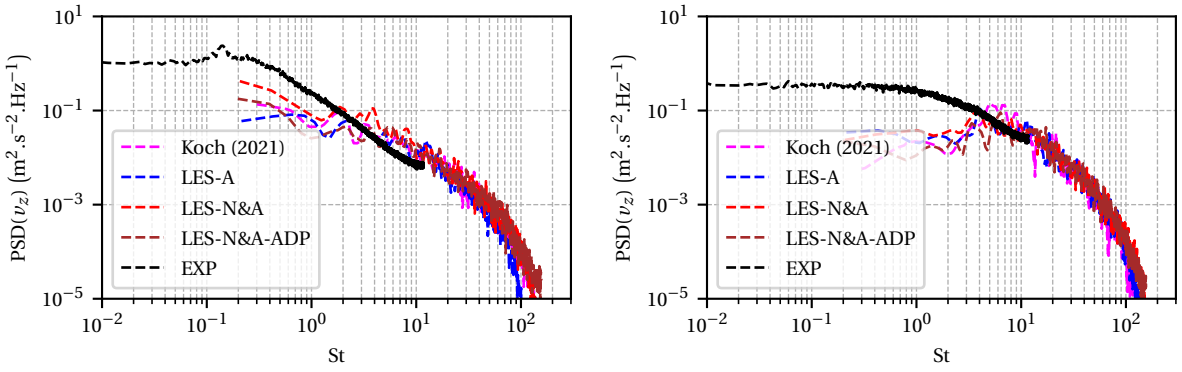

(a) TLV center ($y/c = 0.2$, $z/c = 0.05$)

(b) TLF ($y/c = 0.15$, $z/c = -0.025$)

Figure 3.33: PSD of spanwise velocity component v_z.

impact on the velocity spectra of the tip flow. The same conclusions are made for the spectra of the streamwise component v_x^{rms}.

3.8 Tip wall pressure fluctuations

Scattering of turbulent surface pressure fluctuations into sound is one of the dominant mechanisms behind some important aeroacoustic noise sources, such as trailing edge

noise and rough-wall boundary layer noise [32]. Therefore, Figure 3.34 presents the PSD of wall pressure fluctuations on the airfoil and plate surfaces. Four positions at 77.5% of chord are considered. Probe 21 and 46 are respectively located on the suction side (Figure 3.34a) and pressure side (Figure 3.34d), 1.5 mm away from the tip. In the gap, two probes are located on the camber line: probe B on the airfoil tip (Figure 3.34b) and probe 56 on the lower plate (Figure 3.34c). The Strouhal number St_0 is defined as $St_0 = f.c/V_0$. The LES-A, LES-N&A and LES-N&A-ADP are compared to the measurements extracted from Jacob *et al.* [45]. The experimental cut-off frequency is 22 kHz (St = 62.9) but data are only available until 10 kHz (St = 28.6). Since wall pressure spectra of the LES from Koch *et al.* [51] are not available at 77.5%, the spectra at 75% are used in Figure 3.34.

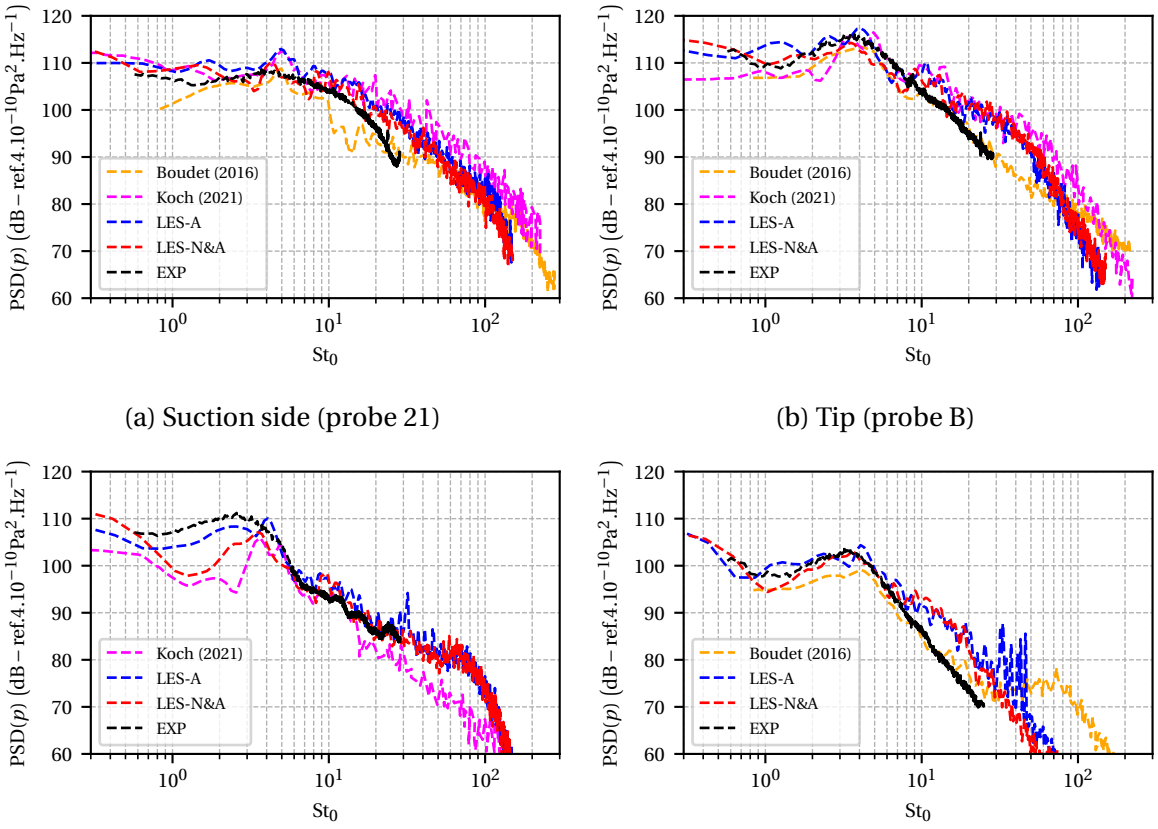

(a) Suction side (probe 21)

(b) Tip (probe B)

(c) Lower plate (probe 56)

(d) Pressure side (probe 46)

Figure 3.34: PSD of wall pressure at 77.5% of chord.

Experimental spectra exhibit a hump around St_0 = 3-4 for the pressure side, tip and lower plate probes. However, in Figure 3.34a, this hump is not found at the suction side probe. Grilliat explains in his thesis [34] that this hump characterises the pressure fluctuations induced by the detachment of the TLF on the airfoil pressure side-tip corner. A broadband hump is observed instead of a tonal peak because of the intermittency of the phenomenon [12]. Moreover, the levels of pressure fluctuations on the suction side are higher than those on the pressure side for all frequencies due to the turbulent activity of the TLV. For the probes

in the gap, the detachment of the TLF from the tip increases the levels on the tip compared to the lower plate.

Spectra from the LES-N&A in red exhibits a good agreement with the experiment in both shape and level. The hump around St_0 = 3-4 in Figure 3.34b is well reproduced by the simulation: both the central frequency and the amplitude are predicted. Deviations are observed in the spectrum slope for Strouhal numbers higher than 10 on the tip (Figure 3.34b) and pressure side (Figure 3.34d) spectra. The same deviation is observed for Koch *et al.* [51] in pink in Figure 3.34b.

The LES-A and LES-N&A globally obtain the same results except on the pressure side spectrum (Figure 3.34d) for which a tonal signature between St_0 = 300 and 500 is noted. To understand this additional noise source between the cases, instantaneous vorticity and dilatation fields are plotted in Figure 3.35.

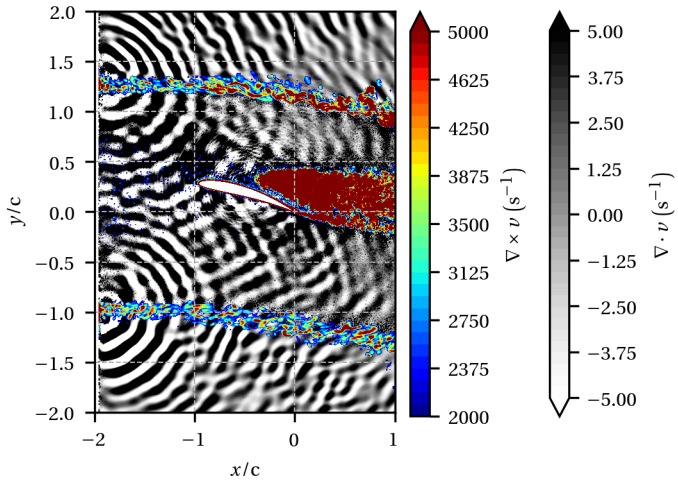

(a) LES-A

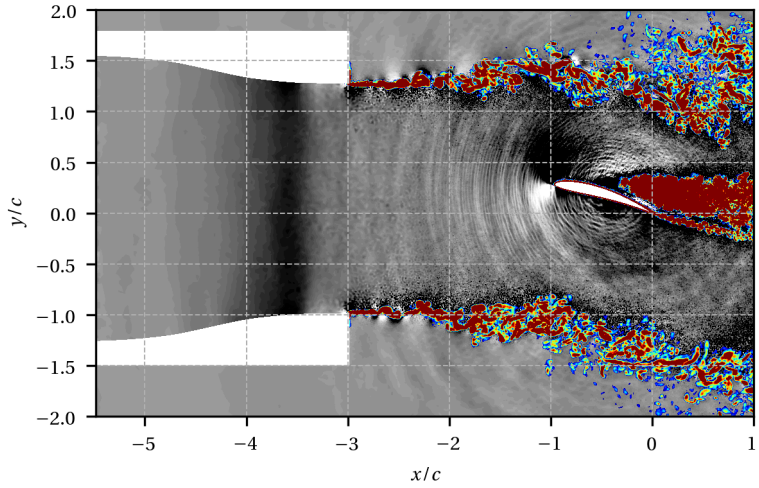

(b) LES-N&A

Figure 3.35: Instantaneous vorticity and dilatation fields at $z/c = 0.1$.

Large differences are observed between the two approaches in Figure 3.35. First, in the

vorticity field, whereas the TLV (x/c > -0.5, 0 < y/c < 0.5) and the airfoil wake are qualitatively similar between the two cases, mixing layers starting from y/c = -1.0 and 1.3 are different. Indeed, considering the full experimental set-up with the nozzle seems to lead to a more natural growth of the jet mixing layers (Figure 3.35b) than for the LES-A case in Figure 3.35a. Then, when considering the acoustic field represented by the dilation field, the LES-A is polluted by a strong numerical spurious noise coming from the inlet. The two sources seem to be located on the jet mixing layers. The tonal noise between St_0 = 300 and 500 in Figure 3.34d is then explained by the synthetic turbulence injection for which the maximum of turbulence intensity on the inlet surface is located in the mixing layers. Adding the nozzle allows to suppress the spurious noise source while keeping the same turbulent activity on tip surfaces.

The LES-N&A in red and LES-N&A-ADP in brown exhibit globally the same shape and levels of wall pressure spectra in Figure 3.34. A slight improvement for the adapted case when compared to the experiment is observed for Strouhal numbers higher than 10 on the airfoil tip (Figure 3.34b). However, the hump around St_0 = 3-4 is less captured than on the initial mesh at 77.5% of chord. The intermittency of the TLF detachment in the gap may explain the discrepancy between the two cases.

The LES from Boudet *et al.* [10] and Koch *et al.* [51] are wall-resolved presented in Figure 3.34. When compared to the wall-modelled LES performed in this thesis, the results are globally the same. The computational cost involved by a wall-resolved mesh is not required for the prediction of the wall pressure fluctuations in the tip flow. The capacity of the wall-law to well capture the near-wall flow physics is demonstrated.

3.9 Far-field noise

Figure 3.36 presents the PSD of acoustic pressure in the far-field. The microphone is set 2 m away from the airfoil suction side, forming an angle of 90° with the airfoil chord. The acoustic propagation in the far-field is ensured using the solid FWH analogy. Only the dipole sources are taken into account to estimate the sound; the quadrupoles associated with the jet-like TLF mentioned in Section 1.2.1 are then ignored. Details about the FWH analogy are given in Section 2.6. The python library *antares* [6] is used following the advanced time formulation of Casalino [16]. Instantaneous surfaces were only dumped for the LES-N&A-ADP.

The microphone recorded the noise emitted by the airfoil in no-gap (grey) and 10-mm-gap (black) configurations. It allows to identify a Strouhal range of the TCN from 2 to 20 (0.7 to 7 kHz). Even if the low-Strouhal number part below 0.6 or 0.9 (200 or 300 Hz) is not accessible in the LES, it is worth mentioning that this part is not reliable because of some issues with the oscillations of the wind-tunnel jet shear layers; the associated background noise cannot be suppressed in this range.

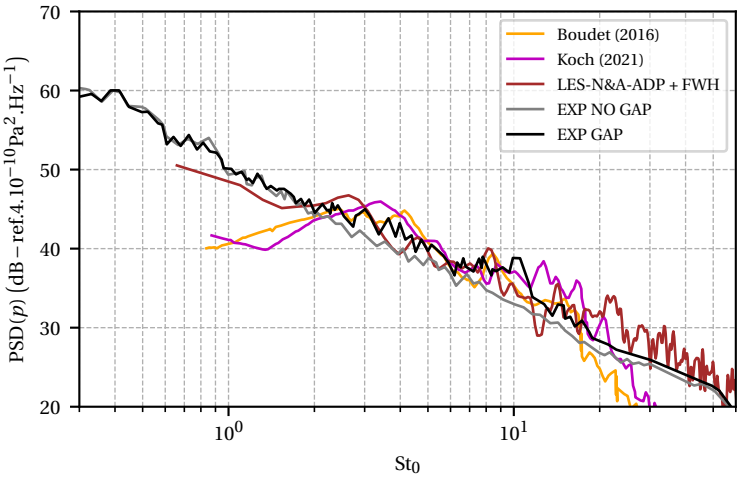

Figure 3.36: PSD of acoustic pressure 2 m away from the airfoil suction side, forming an angle of 90° with the airfoil chord.

The LES-N&A-ADP is able to predict the acoustic spectrum measured in the far-field. The acoustic pressure levels and spectrum slope are recovered on a wide range of Strouhal numbers from 2 to 50. This range is even wider than the LES achieved in the literature from Boudet *et al.* [10] and Koch *et al.* [51] for which discrepancies are observed above St_0= 20. It may be explained by the size of the LES domain. Indeed, Boudet *et al.* [10] performed a ZLES with a LES zone reduced to the tip region and Koch *et al.* [51] achieved a LES on a modified geometry with a reduced span. In both cases, the pressure fluctuations on the airfoil surface are not computed over the full span. This comparison demonstrates also the capacity of the wall-law to model the flow of an airfoil-free jet facility for the purpose of acoustic prediction.

3.10 Partial conclusions

The ability of numerical approaches to recover the aerodynamics and acoustics of the tip flow of a single airfoil has been assessed based on a comparison with experiments. A RANS simulation and three LES were performed and presented in this chapter.

The inflow conditions were first characterised in terms of lower plate boundary layer and turbulence intensity. The RANS boundary layer thickness was in the order of the gap height whereas the experimental one was thinner. The aerodynamics and acoustics of the tip flow could then be impacted. Moreover, the thickening rate of the LES boundary layer was lower than in the experiment and the turbulence intensity profile in the boundary layer was not recovered. These differences with the experiment were explained by the history of the boundary layer. Indeed, the experimental boundary layer came from a wind tunnel whereas it started at the nozzle inlet for the LES. Injecting synthetic homogeneous isotropic turbulence at the LES inlet only improved the turbulence intensity in the outer flow region. Induce the transition to turbulence by a source term, inject anisotropic turbulence or compute the wind

tunnel upstream of the nozzle are solutions to improve the numerical inflow conditions.

The airfoil loading at midspan and tip has been properly recovered by the RANS and LES approaches. The wall-law used for the LES exhibited a good behaviour for the prediction of the pressure distribution, even in the tip region. The jet development, angle of attack and TLV showed to have an influence of the airfoil loading.

The global mean trajectory of the TLV was reproduced in both approaches. Again, the development of the jet mixing layers had an influence on the TLV mean trajectory. However, to recover the complex structure of the vortex, the LES approach resolving the large turbulent structures was required. With the appropriate spatial resolution (achieved through a mesh adaptation technique), the LES approach predicted the streamwise acceleration in the TLV. Moreover, the LES approach was able to accurately compute the topology and spectral content of the TLV turbulence. An overestimation of the turbulence intensity when compared to the experiment was still noted.

The wall pressure fluctuations on the airfoil tip surfaces was predicted by the wall-modelled LES. The turbulence injection did not impact the tip flow aerodynamics but had a non-negligible one on the acoustics. Indeed, a spurious tonal noise located at the inlet boundary was produced polluting the wall pressure spectra. The measured acoustic spectrum in the far-field was recovered using the FWH analogy on solid surfaces.

4 Numerical simulation of a shrouded fan

Numerical simulations of a rig-scaled fan representative of an UHBR turbofan are performed in this chapter.

5 Tip flow analysis

The aim of this chapter is to evaluate the similarity between the tip flows and associated aerodynamic noise sources of the isolated airfoil and fan.

Conclusions

Regarding the potential emergence of tip clearance noise as a primary source of fan noise on the future turbofan architectures, three objectives were set up in the thesis: the understanding of the aerodynamic mechanisms generating tip clearance noise in fan stage at approach regimes, the evaluation of the capacities of numerical methods to reproduce turbomachinery secondary flows and the enhancement of the knowledge for the definition of new improved models of tip clearance noise.

In turbofan engines, a gap exists between the tip of fan blades and the casing wall for operating reason. Due to a pressure difference at the blade tip, a secondary flow going from pressure side to suction side named as the tip leakage flow is generated. At the gap exit, the tip leakage flow interacts with the main flow and rolls up to form the tip leakage vortex in the blade passage. From this tip flow phenomenology, seven aerodynamic mechanisms were identified in the literature and classified into blade self noise, rotor self noise and interaction noise. By comparison of non-dimensional parameters, four mechanisms were retained in fan stage of turbofan engines at approach regimes: the jet-like tip leakage flow, the scattering of vortical structures in the gap by tip edges and the interaction of the tip leakage vortex with the trailing edge of the generating blade or with the adjacent blade.

To study the tip flow and associated noise sources, numerical methods were employed and evaluated by comparison with measurements. LES resolving the large eddies and modelling the small ones, were performed on an isolated airfoil and a rig-scaled fan representative of UHBR turbofan. This numerical method has shown its capacity to recover the tip flow unsteady aerodynamics. The wall-modelled approach exhibited proper results when compared to wall-resolved LES in the isolated airfoil study. The heavy cost of wall-resolved LES was then withdrawn and allowed for the computation of turbomachinery application such as the rig-scaled fan of interest. Moreover, mesh adaptation based on flow quantities has been achieved to refine the tip flow for both the isolated airfoil and fan. This method allowed to design a mesh following the complex three dimensional structure of the tip flow while optimising the mesh size. Nevertheless, a particular attention has to be paid not to

constraint the flow physics. For airfoil-free jet facility, the wind tunnel jet development was shown to have an influence on the flow around the airfoil and especially the convection of the tip leakage vortex. Then, the numerical modelling of the inflow conditions for this kind of facility is of primary importance. Besides, the injection of turbulence produced spurious noise polluting the acoustic spectrum and is then not recommended for aeroacoustics prediction. Finally, vortex identification functions were applied on the numerical results to characterise the tip leakage vortex in terms of trajectory, size and intensity. This method of analysis has shown good results for the identification of large-scale vortex and can be used on other turbomachinery applications.

The LES performed in the thesis were then used to acquire knowledge on the tip flow and associated aerodynamic noise sources. Based on a dimensional analysis providing characteristic dimensionless parameters, the tip flows of the isolated airfoil and fan were compared. Whereas the tip leakage vortex of the isolated airfoil remains a large scale structure for almost the whole chord, the fan vortex rapidly diffused into small vortical structures from 15% of chord. This difference may be explained by a smaller gap height, an earlier detachment from the blade tip, the effect of blade rotation and the flow detachment at the blade leading edge for the fan. Moreover, no additional wall unsteady pressure activity due to the vortical structures coming from the tip leakage vortex were observed at the trailing edge-tip corner for the isolated airfoil and fan. Therefore, the interaction of the tip leakage vortex with the trailing edge of the generating blade or with the adjacent blade was not expected to be a dominant source mechanism in an UHBR turbofan engine. Besides, as explained in the literature, the dominant source mechanism of tip clearance noise for the isolated airfoil is located in the gap, around the mid-chord. This mechanism corresponds to the scattering of the vortical structures by the suction side-tip edge when exiting the gap. Using the Howe's approach, similar mechanism was described at the tip of fan blades.

Perspectives

Regarding the work achieved in the thesis, several improvements and new opportunities in the scope of the tip clearance noise in fan stage of turbofan engines are identified. Perspectives are proposed in terms of numerical simulation, analytical modelling and low-tip clearance noise design.

To predict the acoustic spectrum in the far field of the isolated airfoil case, the FWH analogy has been applied on solid surfaces. Since a direct approach has been set for the LES, *i.e.* compute the sound together with its fluid dynamic source field by solving the compressible flow equations, the FWH analogy on porous surfaces around the jet can be applied (dumped in the current computation). The contribution of dipole and quadrupole sources of the isolated airfoil could then be evaluated separately. Moreover, the first LES of the rig-scaled fan can be further improved. The influence of the gap geometry could be studied by taking into account the chordwise evolution of the gap height. Additional measurements to evaluate the LES prediction of the unsteady aerodynamics of the rig-scaled fan should be also valuable. As for the isolated airfoil, the results from the LES can be used for acoustic prediction purpose and be compared to existing free-field acoustic measurements.

From the modelling point of view, the LES produced a large database on the unsteady aerodynamics of the tip flow that could be helpful to formulate realistic flow hypothesis. Moreover, the dimensional analysis developed in the thesis set up the ground for analytical developments. Correlation laws between dimensionless parameters could then be formulated to determine which aerodynamic noise mechanism of tip clearance noise is dominant for new configurations. Nevertheless, new studies on other configurations are required to extend the database which is currently not sufficient to produce this kind of correlation laws.

As described in the literature, the level of tip clearance noise is mainly influenced by the gap height. The more the gap height is large, the more vortical structures will be produced at the blade tip. Then, the first advice to minimise the contribution of the tip clearance noise to the fan noise would be to have the smallest gap height as possible. If a large gap height could not be avoided for operating reasons, the second advice would be to smooth the tip

edges. Indeed, the dominant mechanism identified in the thesis is the scattering of vortical structures in the gap by the sharp tip edges.

A

Relations of similitude for turbomachinery

Most of the time, measurements are carried out at different ambient conditions. Indeed, experimental campaigns may be performed on different days and locations, thus modifying the external temperature and pressure. Moreover, numerical simulations are often achieved at a single ambient condition. Therefore, data need to be extrapolated at the same ambient condition to be compared to each other. In this Appendix, relations of similitude between two flows of the same turbomachinery at different ambient conditions are developed.

A.1 Flowrate

Considering a section normal to the axis of rotation of the turbomachinery at two flow conditions a and b (at the air intake for instance), one can write

$$\frac{\dot{m}_a}{\dot{m}_b} = \frac{\rho_a S_a v_a}{\rho_b S_b v_b} = \frac{\frac{P_a}{r_a T_a} S_a v_a}{\frac{P_b}{r_b T_b} S_b v_b}$$

$\dot{m}$ is the massflow rate normal to the section S and v is the corresponding flow speed. Since the same turbomachinery is considered for the two conditions: $S_a = S_b$. The same fluid is used and the variation of temperature is small then $r_a = r_b$ and $\gamma_a = \gamma_b$. The cinematic homothety between a and b implies the same compressible effects. Therefore, the Mach number Ma is the same between a and b:

$$\mathrm{Ma}_a = \mathrm{Ma}_b \Rightarrow \frac{v_a}{\sqrt{r_a \gamma_a T_a}} = \frac{v_b}{\sqrt{r_b \gamma_b T_b}} \Rightarrow \frac{v_a}{v_b} = \frac{\sqrt{T_a}}{\sqrt{T_b}}$$

Combining the two previous equations results in:

$$\frac{\dot{m}_a \sqrt{T_a}}{P_a} = \frac{\dot{m}_b \sqrt{T_b}}{P_b} \tag{A.1}$$

Using the definition of total temperature and pressure

$$\frac{\frac{T_{ta}}{T_a}}{\frac{T_{tb}}{T_b}} = \frac{1+\frac{\gamma_a-1}{2}\mathrm{Ma}_a^2}{1+\frac{\gamma_b-1}{2}\mathrm{Ma}_b^2} \Rightarrow \frac{T_a}{T_b} = \frac{T_{ta}}{T_{tb}}$$

and

$$\frac{P_t}{P} = \left(\frac{T_t}{T}\right)^{\frac{\gamma}{\gamma-1}} \Rightarrow \frac{P_a}{P_b} = \frac{P_{ta}}{P_{tb}}$$

Therefore, Equation A.1 becomes

$$\frac{\dot{m}_a\sqrt{T_{ta}}}{P_{ta}} = \frac{\dot{m}_b\sqrt{T_{tb}}}{P_{tb}} \tag{A.2}$$

This ratio is called the reduced massflow rate.

A.2 Rotation speed

Let's now consider the speed of rotation of a rotor at two different conditions a and b, one can write:

$$\frac{N_a}{N_b} = \frac{\frac{2\pi}{60}\frac{u_a}{r_a}}{\frac{2\pi}{60}\frac{u_b}{r_b}} = \frac{u_a}{u_b}$$

u is defined as the linear speed of rotation at a certain radius r. The cinematic homothety implies that the Mach number Ma is invariant:

$$\mathrm{Ma}_a = \mathrm{Ma}_b \Rightarrow \frac{u_a}{u_b} = \frac{\sqrt{T_a}}{\sqrt{T_b}} \Rightarrow \frac{N_a}{\sqrt{T_a}} = \frac{N_b}{\sqrt{T_b}}$$

Again, the definition of total temperature can be used resulting in

$$\frac{N_a}{\sqrt{T_{ta}}} = \frac{N_b}{\sqrt{T_{tb}}} \tag{A.3}$$

This ratio is called the reduced speed of rotation.

B

Fluctuating velocity components for the airfoil

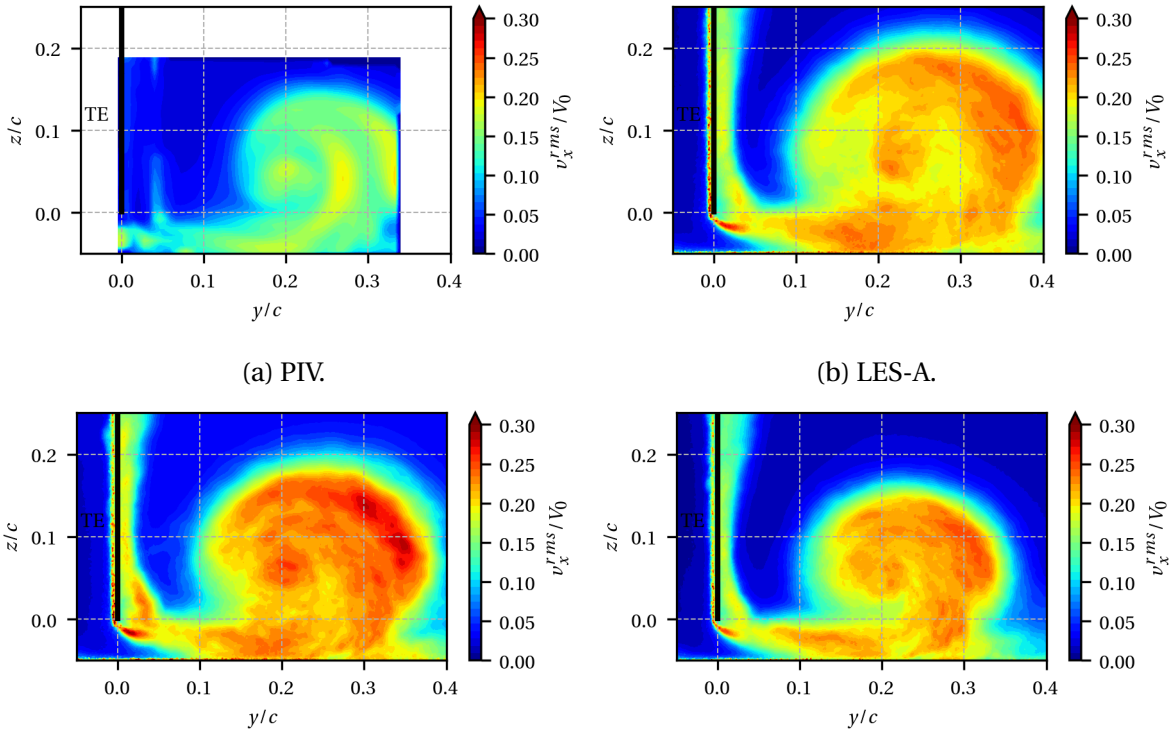

(a) PIV.

(b) LES-A.

(c) LES-N&A.

(d) LES-N&A-ADP.

Figure B.1: Streamwise fluctuating velocity component v_x^{rms} of the TLV at the airfoil trailing edge ($x/c = 0.01$).

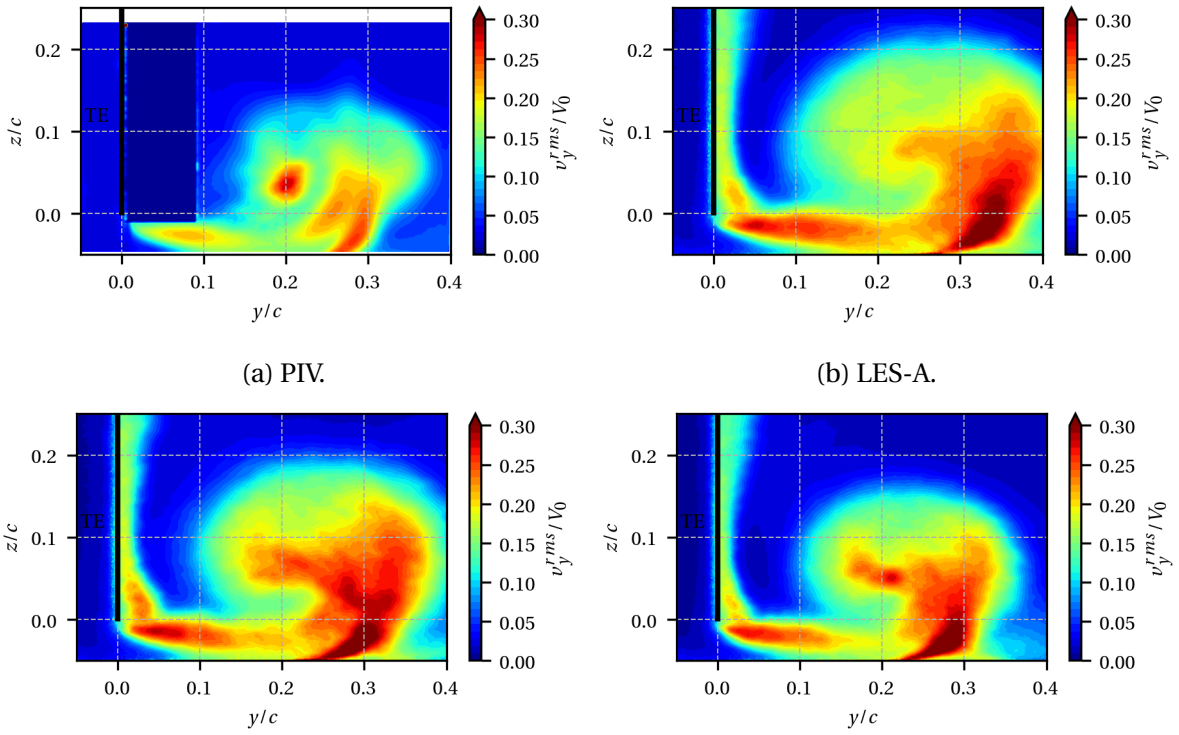

(a) PIV.

(b) LES-A.

(c) LES-N&A.

(d) LES-N&A-ADP.

Figure B.2: Cross-stream fluctuating velocity component v_y^{rms} of the TLV at the airfoil trailing edge ($x/c = 0.01$).

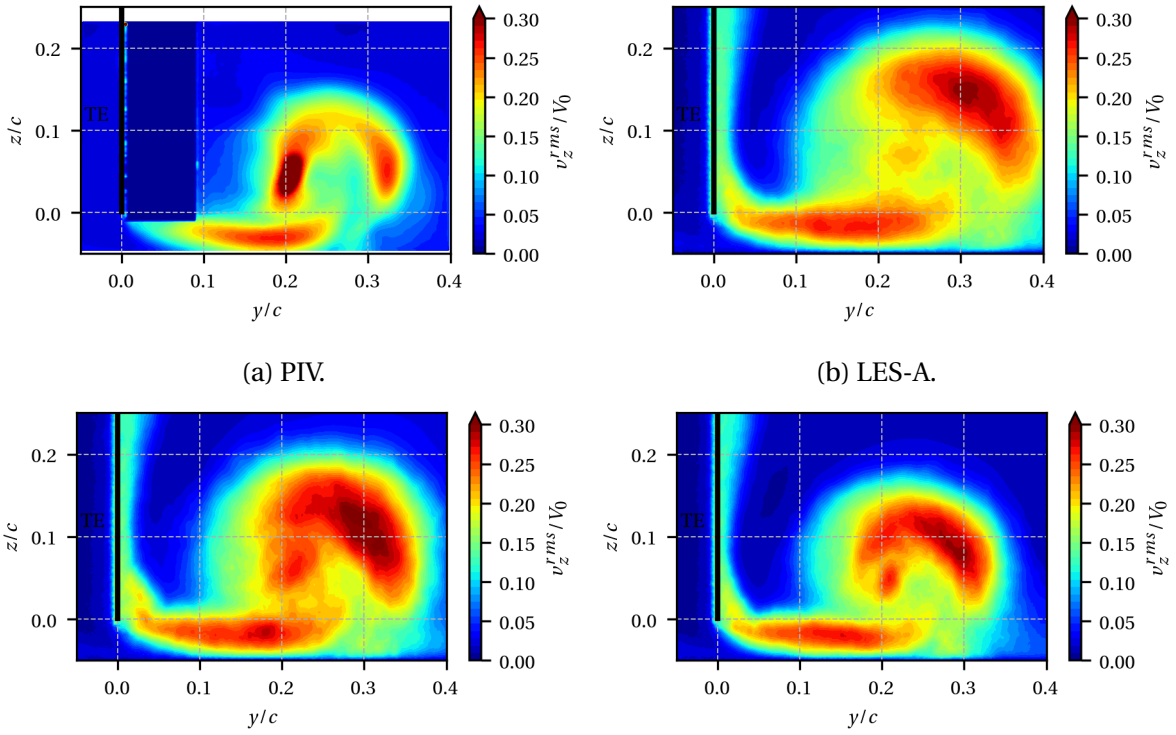

(a) PIV.

(b) LES-A.

(c) LES-N&A.

(d) LES-N&A-ADP.

Figure B.3: Spanwise fluctuating velocity component v_z^{rms} of the TLV at the airfoil trailing edge ($x/c = 0.01$).

Bibliography

[1] CFM56 Engine. https://www.cfmaeroengines.com/engines/cfm56/. Accessed: 2021-12-21.

[2] ENOVAL European project. https://cordis.europa.eu/project/id/604999/reporting. Accessed: 2021-12-23.

[3] LEAP Engine. https://www.cfmaeroengines.com/engines/leap/. Accessed: 2021-12-21.

[4] Souffleries anéchoïques du LMFA. http://lmfa.ec-lyon.fr/spip.php?article289. Accessed: 2019-11-18.

[5] R. Amiet. Noise due to turbulent flow past a trailing edge. *Journal of sound and vibration*, 47(3):387–393, 1976.

[6] Antares Development Team. Antares Documentation Release 1.17.0. https://cerfacs.fr/antares/, 2021.

[7] B. Baldwin and H. Lomax. Thin-layer approximation and algebraic model for separated turbulentflows. In *16th Aerospace Sciences Meeting*, 1978.

[8] J. P. Bindon. The Measurement and Formation of Tip Clearance Loss. *Journal of Turbomachinery*, 111(3):257–263, 1989.

[9] J. Boudet, A. Cahuzac, P. Kausche, and M. C. Jacob. Zonal Large-Eddy Simulation of a Fan Tip-Clearance Flow, With Evidence of Vortex Wandering. *Journal of Turbomachinery*, 137(6):061001, 2015.

[10] J. Boudet, J. Caro, B. Li, E. Jondeau, and M. C. Jacob. Zonal Large-Eddy simulation of a tip leakage flow. *International Journal of Aeroacoustics*, 15(6-7):646–661, 2016.

[11] J. Boudet, J. Grilliat, J. Caro, and J. M.C. Combined experimental/computational study of the tip clerance flow and acoustics. 2009.

[12] J. Boudet, M. C. Jacob, J. Caro, E. Jondeau, and B. Li. Wavelet analysis of a blade tip-leakage flow. *AIAA Journal*, 56(8):3332–3336, 2018.

[13] W. Cabot and P. Moin. Approximate wall boundary conditions in the large-eddy simulation of high reynolds number flow. *Flow, Turbulence and Combustion*, 63:269–291, 2000.

[14] L. Cambier, S. Heib, and S. Plot. The Onera elsA CFD software: input from research and feedback from industry. *Mechanics & Industry*, 14(3):159–174, 2013.

[15] R. Camussi, J. Grilliat, G. Caputi-Gennaro, and M. C. Jacob. Experimental study of a tip leakage flow: wavelet analysis of pressure fluctuations. *Journal of Fluid Mechanics*, 660:87–113, 2010.

[16] D. Casalino. An advanced time approach for acoustic analogy predictions. *Journal of Sound and Vibration*, 261(4):583–612, 2003.

[17] G. T. Chen, E. M. Greitzer, C. S. Tan, and F. E. Marble. Similarity Analysis of Compressor Tip Clearance Flow Structure. *Journal of Turbomachinery*, 113(2):260–269, 1991.

[18] O. Colin. A finite element operator for diffusion terms in AVBP. Technical report, Institut Français du Pétrole, 2003.

[19] O. Colin and M. Rudgyard. Development of high-order Taylor–Galerkin schemes for LES. *Journal of Computational Physics*, 162(2):338–371, 2000.

[20] C. Dapogny, C. Dobrzynski, and P. Frey. Three-dimensional adaptive domain remeshing, implicit domain meshing, and applications to free and moving boundary problems. *Journal of computational physics*, 262:358–378, 2014.

[21] G. Daviller, M. Brebion, P. Xavier, G. Staffelbach, J. M. Müller, and T. Poinsot. A Mesh Adaptation Strategy to Predict Pressure Losses in LES of Swirled Flows. *Flow, Turbul. Combust.*, 99(1), 2017.

[22] G. Daviller, G. Oztarlik, and T. Poinsot. A generalized non-reflecting inlet boundary condition for steady and forced compressible flows with injection of vortical and acoustic waves. *Computers & Fluids*, 190:503–513, 2019.

[23] J. W. Deardorff. A numerical study of three-dimensional turbulent channel flow at large reynolds numbers. *Journal of Fluid Mechanics*, 41(2):453–480, 1970.

[24] J. Dittmar. Interaction of rotor tip flow irregularities with stator vanes as a noise source. In *4th Aeroacoustics Conference*, 1977.

[25] J. H. Dittmar, R. P. Woodward, and M. J. MacKinnon. Fan noise reduction achieved by removing tip flow irregularities behind the rotor-forward arc test configuration. In *Meeting of the Acoustical Soc. of Am.*, 1984.

[26] R. Dunne and M. Howe. Wall-bounded blade-tip vortex interaction noise. *Journal of Sound and Vibration*, 202(5):605–618, 1997.

[27] T. Fukano and C. M. Jang. Tip clearance noise of axial flow fans operating at design and off-design condition. *Journal of Sound and Vibration*, 275(3-5):1027–1050, 2004.

[28] T. Fukano, Y. Takamatsu, and Y. Kodama. The Effects of Tip Clearance Axial and on the Noise Fans of Pressure. *Journal of Sound and Vibration*, 105(2):291–308, 1986.

[29] U. W. Ganz, P. D. Joppa, T. J. Patten, and D. F. Scharpf. Boeing 18-Inch Fan Rig Broadband Noise Test. Technical report, NASA, 1998.

[30] E. Garnier, N. Adams, and P. Sagaut. *Large eddy simulation for compressible flows*. Springer Science & Business Media, 2009.

[31] M. Germano, U. Piomelli, P. Moin, and W. H. Cabot. A dynamic subgrid-scale eddy viscosity model. *Physics of Fluids A: Fluid Dynamics*, 3(7):1760–1765, 1991.

[32] S. Glegg and W. Devenport. *Aeroacoustics of low Mach number flows: fundamentals, analysis, and measurement*. Academic Press, 2017.

[33] L. Graftieaux, M. Michard, and N. Grosjean. Combining PIV, POD and vortex identification algorithms for the study of unsteady turbulent swirling flows. *Measurement Science and technology*, 12(9):1422, 2001.

[34] J. Grilliat. *Contribution à l'étude aéroacoustique des écoulements de jeu*. PhD thesis, École Centrale de Lyon, 2009.

[35] J. Grilliat, M. C. Jacob, E. Jondeau, M. Roger, and R. Camussi. Broaband noise prediction models and measurements of tip leakage flows. In *14th AIAA/CEAS Aeroacoustics Conference (29th AIAA Aeroacoustics Conference)*, 2008.

[36] Hip Development Team. Pyhip 0.3.2. https://pypi.org/project/pyhip/, 2021.

[37] M. Howe. Contributions to the theory of aerodynamic sound, with application to excess jet noise and the theory of the flute. *Journal of Fluid Mechanics*, 71(4):625–673, 1975.

[38] M. S. Howe. The dissipation of sound at an edge. *Journal of Sound and Vibration*, 70:407–411, 1980.

[39] C. E. Hughes. *NASA Collaborative Research on the Ultra High Bypass Engine Cycle and Potential Benefits for Noise, Performance, and Emissions*. National Aeronautics and Space Administration, Glenn Research Center, 2013.

[40] IATA. IATA Forecast Predicts 8.2 billion Air Travelers in 2037. https://www.iata.org/en/pressroom/pr/2018-10-24-02/. Accessed: 2021-12-21.

[41] IATA. IATA Revises 2020 Passenger Traffic Forecast Down for Africa. https://www.iata.org/en/pressroom/pr/2020-10-21-02/. Accessed: 2021-12-21.

[42] IATA. IATA Revises 2020 Passenger Traffic Forecast Down for the Middle East. https://www.iata.org/en/pressroom/pr/2020-10-21-01/. Accessed: 2021-12-21.

[43] M. Inoue and M. Kuroumaru. Structure of Tip Clearance Flow in an Isolated Axial Compressor Rotor. *Journal of Turbomachinery*, 111(3):250–256, 1989.

[44] International Civil Aviation Organization. Environmental Protection: Annex 16 to the Convention on International Civil Aviation. Technical report, International Civil Aviation Organization, 2008.

[45] M. C. Jacob, J. Grilliat, R. Camussi, and G. C. Gennaro. Aeroacoustic Investigation of a Single Airfoil Tip Leakage Flow. *International Journal of Aeroacoustics*, 9(3):253–272, 2010.

[46] M. C. Jacob, E. Jondeau, and B. Li. Time-resolved PIV measurements of a tip leakage flow. *International Journal of Aeroacoustics*, 15(6-7):662–685, 2016.

[47] F. Kameier and W. Neise. Experimental Study of Tip Clearance Losses and Noise in Axial Turbomachines and their Reduction. *Journal of Turbomachinery*, 119(3):460–471, 1997.

[48] F. Kameier and W. Neise. Rotating blade flow instability as a source of noise in axial turbomachines. *Journal of Sound and Vibration*, 203(5):833–853, 1997.

[49] S. Kang and C. Hirsch. Experimental Study on the Three-Dimensional Flow Within a Compressor Cascade With Tip Clearance: Part II—The Tip Leakage Vortex. *Journal of Turbomachinery*, 115(3):444–450, 1993.

[50] S. Kang and C. Hirsch. Experimental Study on the Three-Dimensional Flow Within a Compressor Cascade With Tip Clearance: Part I—Velocity and Pressure Fields. *Journal of Turbomachinery*, 115(3):435–443, 1993.

[51] R. Koch, M. Sanjosé, and S. Moreau. Large-eddy simulation of a single airfoil tip-leakage flow. *AIAA Journal*, 59:2546–2557, 2021.

[52] V. Kolár. Compressibility effect in vortex identification. *AIAA journal*, 47(2):473–475, 2009.

[53] R. H. Kraichnan. Diffusion by a random velocity field. *The physics of fluids*, 13(1):22–31, 1970.

[54] B. Lakshminarayana. *Fluid Dynamics and Heat Transfer of Turbomachinery*. John Wiley & Sons Inc., 1996.

[55] B. Lakshminarayana, M. Zaccaria, and B. Marathe. The Structure of Tip Clearance Flow in Axial Flow Compressors. *Journal of Turbomachinery*, 117(3):336–347, 1995.

[56] A. Leonard. Energy cascade in large-eddy simulations of turbulent fluid flows. 18:237–248, 1975.

[57] E. Lévêque, F. Toschi, L. Shao, and J.-P. Bertoglio. Shear-improved smagorinsky model for large-eddy simulation of wall-bounded turbulent flows. *Journal of Fluid Mechanics*, 570:491–502, 2007.

[58] B. Li. *Aerodynamic and acoustic analysis of the tip-leakage flow past a single ailfoil*. PhD thesis, École Centrale de Lyon, 2016.

[59] M. J. Lighthill. On sound generated aerodynamically i. general theory. *Proceedings of the Royal Society of London. Series A. Mathematical and Physical Sciences*, 211(1107):564–587, 1952.

[60] R. E. Longhouse. Control of tip-vortex noise of axial flow fans by rotating shrouds. *Journal of Sound and Vibration*, 58(2):201–214, 1978.

[61] J. März, C. Hah, and W. Neise. An Experimental and Numerical Investigation into the Mechanisms of Rotating Instability. *Journal of Turbomachinery*, 124(3):367–374, 2002.

[62] J. Moore and J. S. Tilton. Tip leakage flow in a linear turbine cascade. *Journal of Turbomachinery*, 110:18–26, 1988.

[63] S. Moreau. Turbomachinery noise predictions: present and future. 1(1):92–116, 2019.

[64] S. Moreau, M. Henner, G. Iaccarino, M. Wang, and M. Roger. Analysis of flow conditions in freejet experiments for studying airfoil self-noise. *AIAA journal*, 41(10):1895–1905, 2003.

[65] F. Nicoud and F. Ducros. Subgrid-scale stress modelling based on the square of the velocity gradient tensor. *Flow, turbulence and Combustion*, 62(3):183–200, 1999.

[66] F. Nicoud, H. B. Toda, O. Cabrit, S. Bose, and J. Lee. Using singular values to build a subgrid-scale model for large eddy simulations. *Physics of fluids*, 23(8):085106, 2011.

[67] F. Nicoud, H. B. Toda, O. Cabrit, S. Bose, and J. Lee. Using singular values to build a subgrid-scale model for large eddy simulations. *Physics of Fluids*, 23(8):085106, 2011.

[68] N. Odier, A. Thacker, M. Harnieh, G. Staffelbach, L. Gicquel, F. Duchaine, N. G. Rosa, and J.-D. Müller. A mesh adaptation strategy for complex wall-modeled turbomachinery les. *Computers & Fluids*, 214:104766, 2021.

[69] B. Pardowitz, U. Tapken, L. Neuhaus, and L. Enghardt. Experiments on an Axial Fan Stage: Time-Resolved Analysis of Rotating Instability Modes. *Journal of Engineering for Gas Turbines and Power*, 137(6):062505, 2015.

[70] T. Passot and A. Pouquet. Numerical simulation of compressible homogeneous flows in the turbulent regime. *Journal of Fluid Mechanics*, 181:441–466, 1987.

[71] T. Poinsot and S. Lele. Boundary conditions for direct simulations of compressible viscous flows. *Journal of Computational Physics*, 101(1):104–129, 1992.

[72] S. B. Pope. *Turbulent flows*. Cambridge University Press, 2000.

[73] A. Powell. Theory of vortex sound. *The journal of the acoustical society of America*, 36(1):177–195, 1964.

[74] L. Prandtl. Eine Beziehung zwischen Wärmeaustausch unf Strömungswiderstand der Flüssigkeit. *Zeitung Physik*, 11:1072–1078, 1910.

[75] D. A. Rains. Tip clearance flows in axial flow compressors and pumps. Technical report, California Institute of Technology, Hydrodynamics and Mechanical Engineering Laboratories, 1954.

[76] P. L. Roe. Approximate Riemann solvers, parameter vectors, and difference schemes. *Journal of computational physics*, 43(2):357–372, 1981.

[77] M. Roger and S. Moreau. Back-scattering correction and further extensions of amiet's trailing-edge noise model. part 1: theory. *Journal of Sound and Vibration*, 286(3):477–506, 2005.

[78] Y. Rozenberg, M. Roger, A. Guédel, and S. Moreau. Rotating blade self noise: experimental validation of analytical models. In *13th AIAA/CEAS Aeroacoustics Conference (28th AIAA Aeroacoustics Conference)*, 2007.

[79] P. Sagaut, S. Deck, and M. Terracol. *Multiscale and Multiresolution Approaches in Turbulence*. Cambridge University Press, 2006.

[80] P. Schmitt, T. Poinsot, and K. Schuermans, B .and Geigle. Large-eddy simulation and experimental study of heat transfer, nitric oxide emissions and combustion instability

in a swirled turbulent high-pressure burner. *Journal of Fluid Mechanics*, 570:17–46, 2007.

[81] T. Schønfeld and M. Rudgyard. Steady and unsteady flow simulations using the hybrid flow solver AVBP. *AIAA journal*, 37(11):1378–1385, 1999.

[82] L. Selle, F. Nicoud, and T. Poinsot. Actual impedance of nonreflecting boundary conditions: Implications for computation of resonators. *AIAA journal*, 42(5):958–964, 2004.

[83] S. Sjolander and K. Amrud. Effects of tip clearance on blade loading in a planar cascade of turbine blades. *Journal of Turbomachinery*, 109:237–244, 1987.

[84] J. Smagorinsky. General circulation experiments with the primitive equations: I. the basic experiment. *Monthly weather review*, 91(3):99–164, 1963.

[85] A. J. Smits and J.-P. Dussauge. *Turbulent shear layers in supersonic flow*. Springer Science & Business Media, 2006.

[86] P. Spalart and S. Allmaras. A one-equation turbulence model for aerodynamic flows. In *30th aerospace sciences meeting and exhibit*, page 439, 1992.

[87] P. R. Spalart. Detached-eddy simulation. *Annual review of fluid mechanics*, 41:181–202, 2009.

[88] D. Spalding. A single formula for the "law of the wall". *Journal of Applied Mechanics*, pages 455–458, 1961.

[89] J. A. Storer and N. A. Cumpsty. Tip Leakage in Axial Compressors. *Journal of Turbomachinery*, 113(2):252–259, 1991.

[90] G. I. Taylor. Conditions at the Surface of a Hot Body Exposed to the Wind. *Rep. Memo. of the British Advisory Committee for Aeronautics*, 272:423–429, 1916.

[91] P. Tucker. Computation of unsteady turbomachinery flows: Part 2—LES and hybrids. *Progress in Aerospace Sciences*, 47(7):546–569, 2011.

[92] C. Wagner, T. Hüttl, and P. Sagaut. *Large-eddy simulation for acoustics*, volume 20. Cambridge University Press, 2007.

[93] D. C. Wilcox. Reassessment of the scale-determining equation for advanced turbulence models. *AIAA journal*, 26(11):1299–1310, 1988.

[94] J. F. Williams and D. L. Hawkings. Sound generation by turbulence and surfaces in arbitrary motion. *Philosophical Transactions for the Royal Society of London. Series A, Mathematical and Physical Sciences*, pages 321–342, 1969.

[95] D. You, M. Wang, P. Moin, and R. Mittal. Vortex dynamics and low-pressure fluctuations in the tip-clearance flow. *Journal of Fluids Engineering*, 129(8):1002–1014, 2007.

[96] X. Zheng and F. Liu. Staggered upwind method for solving Navier-Stokes and k-omega turbulence model equations. *AIAA journal*, 33(6):991–998, 1995.

[97] T. Zhu, D. Lallier-Daniels, M. Sanjosé, S. Moreau, and T. Carolus. Rotating coherent flow structures as a source for narrowband tip clearance noise from axial fans. *Journal of Sound and Vibration*, 417(6):198–215, 2018.

[98] W. Zierke, K. Farrell, and W. Straka. Measurements of the tip clearance flow for a high-reynolds-number axial-flow rotor. *Journal of Turbomachinery*, 117(4):522–532, 1995.

[99] École Centrale de Lyon. Bruit des transports aériens et terrestres, 2020. Copyright Safran Aircraft Engines.

dernière page de la thèse

AUTORISATION DE SOUTENANCE

Vu les dispositions de l'arrêté du 25 mai 2016,

Vu la demande du directeur de thèse

Monsieur L. ROGER

et les rapports de

M. T. CAROLUS
Professeur - University of Siegen - Institute for Fluid and Thermodynamics - Paul Bonatz Strasse 9-11 - D-57068 Siegen - Allemagne

et de

Mme M. SANJOSE
Professeure - Ecole de Technologie Supérieure de l'Université du Québec - 1100 Rue Notre-Dame Ouest - Montréal (QC) H3C 1K3 - Canada

Monsieur LAMIDEL David

est autorisé à soutenir une thèse pour l'obtention du grade de **DOCTEUR**

Ecole doctorale Mécanique, Energétique, Génie civil, Acoustique

Fait à Ecully, le 25 mars 2022

Pour le directeur de l'Ecole centrale de Lyon
Le directeur des Formations

Service Scolarité
ECULLY

Grégory VIAL